

**The Use of Geospatial Science to Map the Distribution of
Ecklonia radiata (Golden Kelp) at Aldinga Reef, South
Australia**

By

Basma Abdul Muhsin

Thesis

Submitted to Flinders University

for the degree of

Master of Geospatial Information Science
College of Science and Engineering

26th November 2021

TABLE OF CONTENTS

TABLE OF CONTENTS	I
ABSTRACT	IV
DECLARATION.....	V
ACKNOWLEDGEMENTS.....	VI
LIST OF FIGURES	VII
LIST OF TABLES.....	IX
1 INTRODUCTION	1
1.1 Rationale	1
1.1.1 Research Objectives.....	3
1.2 Study Area: Aldinga Reef.....	4
1.3 An Outline of the Thesis.....	8
2 LITERATURE REVIEW	10
2.1 Remote Sensing of <i>Ecklonia radiata</i>	10
2.1.1 Remote Sensing and Types of Resolution	10
2.1.2 Benthic Habitat Mapping using optical remote sensing	11
2.1.3 Light attenuation in water	11
2.1.4 Water Column Correction	12
2.1.5 Atmospheric effects	13
2.1.6 Atmospheric Correction or Radiometric Correction	14
2.1.7 Confounding Effect of Sun-glint	15
2.1.8 Sun-glint removal.....	15
2.1.9 UAV Image Capture Over Shallow Water	16
2.1.10 Environmental Conditions for Image Collection Over Shallow Water	17
2.2 Image Classification.....	17
2.2.1 Image pre-processing	17
2.2.2 Key Image Classification Approaches.....	18
2.2.3 Machine Learning and SVM.....	20
2.3 Golden kelp <i>Ecklonia radiata</i> in southern Australia	21
2.3.1 Classification and reproduction	22
2.3.2 Distribution and factors that contribute to distribution of <i>Ecklonia</i> species.....	24
2.3.3 Reflectance properties, spectral signature and remote sensing of <i>Ecklonia radiata</i> ..	26
2.3.4 Future environmental threats on <i>Ecklonia radiata</i>	28
3 METHODS.....	29
3.1 Planning for Field Data Collection	29
3.2 Preliminary Survey.....	30
3.2.1 Identifying sensor and flying altitude of UAV	30
3.2.2 Identifying appropriate environmental conditions for UAV detection of <i>Ecklonia radiata</i>	

3.3	Collection of UAV images	32
3.3.1	Image Collection to Estimate Cover of <i>E. radiata</i>	33
3.3.2	Image Collection to Validate Classification Model	35
3.4	Pre-processing of UAV Images	38
3.4.1	Georeferencing and Mosaicking	39
3.5	Image Classification	41
3.6	Data Validation	44
3.6.1	Validation in subtidal zone	44
3.6.2	Validation in rockpools	45
3.7	Accuracy Assessment	46
4	RESULTS	47
4.1	Preliminary Survey	47
4.1.1	Ability of Different Types of Sensors and Bandwidths to Detect <i>E. radiata</i>	47
4.1.2	UAV Flying Altitude to Detect <i>E. radiata</i>	47
4.1.3	Environmental Conditions for UAV Image Collection	48
4.2	Image Classification Outputs for Validation sites	50
4.2.1	Classification of images over zone S	50
4.2.2	Classification of Images over zone I	57
4.3	Image Classification Outputs for Individual Images Over Study Area	62
4.4	Validation and Accuracy Assessment	66
4.4.1	Validation and accuracy assessment in Zone S	67
4.4.2	Validation and accuracy assessment in Zone I	68
5	DISCUSSION	71
5.1	Optimum observational requirements and conditions for mapping <i>E. radiata</i> using UAV imagery at Aldinga Reef	71
5.1.1	Sensors and multispectral bands	71
5.1.2	Operational Conditions and UAV flying requirements	71
5.2	Extent to which UAV RGB imagery can be used to detect <i>E. radiata</i>	74
5.2.1	Deep Subtidal Zone (Zone S)	74
5.2.2	Deep Subtidal Zone (Zone I)	75
5.2.3	Individual Images Over the whole study area	75
5.3	Percentage Cover and Distribution of <i>E. radiata</i> in Aldinga Reef	76
5.3.1	Distribution of <i>E. radiata</i> at Zone S	76
5.3.2	Percent Cover of <i>E. radiata</i> in the Study Area	77
6	CONCLUSION AND RECOMMENDATION	78
6.1	Conclusion	78
6.1.1	Optimal observational conditions for mapping <i>E. radiata</i> using UAV imagery over Aldinga Reef	78
6.1.2	<i>Ecklonia radiata</i> detection in intertidal and subtidal zones using UAV RGB imagery	79
6.2	Recommendations	79
7	REFERENCE LIST	82

8	APPENDICES	94
8.1	Permits and certificates.....	94
8.1.1	Marine Parks Permit to Undertake Scientific Research.....	94
8.1.2	RPA Operator Accreditation Certificate.....	98
8.2	Screenshots of GSP Missions.....	99
8.2.1	Screenshots of GSP 3D Mission Flight Plans to capture overlapping images over the Dive Validation Areas in Zone.....	99
8.2.2	Screenshots of Way Point Mission Flight Plans to capture individual images over Zone I and Zone S.....	102
8.3	Map Outputs	107
8.3.1	Ecklonia radiata cover in Validation Sites (Zone S) in Aldinga Reef.....	107
8.3.2	Ecklonia radiata cover in Validation Sites (Zone I) in Aldinga Reef	110
8.3.3	Ecklonia radiata cover in Individual Images in (Zone I) in Aldinga Reef	112
8.3.4	Ecklonia radiata cover in Individual Images in (Zone S) in Aldinga Reef	112

ABSTRACT

Ecklonia radiata is the dominant macroalgae, the defining feature of the Great Southern Reef (GSR) and the only laminarian kelp in most of its distribution. Hence its services are environmentally, ecologically and socioeconomically important. Despite *E. radiata*'s resilience to some temperature increase, it is reported that climate change related shifts can affect the early development of the species and had led to its loss. Therefore, there is a need to explore easy-to-use and rapid methods to monitor *E. radiata*. This research explores the use of Unmanned Aerial Vehicle (UAV) images to estimate the percentage of *E. radiata* in Aldinga Reef, South Australia, using a simple empirical classification model and explores optimal observational conditions to detect *E. radiata* from UAV images. The optimum observational conditions were explored by flying UAV at varying conditions. Images were captured over shallow intertidal (Zone I) and deeper subtidal (Zone S) environments at a UAV flying altitude of 20 m. Supervised Support Vector Machine (SVM) was used in ArcGIS Pro to classify them. SVM classification results were compared with *in-situ* validation and an accuracy assessment was carried out. The results show that it is recommended to collect UAV images at low tide and bright sunlight without cloud cover. This is because water attenuation with depth (i.e high tide) and lower light intensity (cloud cover) reduces the red spectral reflectance of *E. radiata* making it spectrally similar to other aquatic vegetation. UAV oblique images can capture *E. radiata* when UAV heading is aligned to sun azimuth with the sensor facing away from the sun and when UAV tilt is aligned to sun elevation above horizon angles. In intertidal zones, UAV nadir and oblique images can capture *E. radiata* at higher sun altitude angles (41°) and with higher windspeeds (30km/hr) than recommended. In subtidal zones, images can be captured with higher sun altitudes and windspeeds than recommended to a certain degree of success, when overlapping UAV images are captured. The SVM classification model proposed can be used to classify and estimate *E. radiata* cover accurately in intertidal and shallow subtidal areas. However, in deeper subtidal zones the accuracy of this method was low. This method can be improved with the use of high spatial resolution bathymetry data to carry out water column correction. The use of sensors with higher radiometric resolution and exposure control can help better correct for illumination change in oblique images.

DECLARATION

I certify that this thesis does not incorporate without acknowledgment any material previously submitted for a degree or diploma in any university; and that to the best of my knowledge and belief it does not contain any material previously published or written by another person except where due reference is made in the text.

Signed 

Date 26 November 2021

ACKNOWLEDGEMENTS

I would like to express my gratitude and appreciation for the following people who made this research possible.

- To my supervisors Associate Professor David Bruce and Dr Ryan Baring for their continuous support, encouragement, guidance, and belief in me that helped me push through during difficult times and enjoy this journey of learning. Thank you, David, especially for introducing me the amazing world of rocky reefs and to the spectacular Golden Kelp.
- To Dr Robert Keane for his guidance and support especially in UAV training and field work components.
- To my program coordinator Dr Tessa Lane, and my tutor Dr Claire Moore for their encouragement, support, and belief in me.
- To my scientific dive team members Joshua Dennis, Matt Lloyd, Adrienne Gooden and Oliver Petersen for a long day of dive data collection in the freezing cold winter water, and for all the preparation and planning to make it a success. I am extremely grateful for your hard work.
- To my fieldwork support team for their time, energy, and commitment. I would like to thank Joram Downes and Michael Hillman for their technical support in fieldwork and UAV flying. I would like to thank Joram for sharing his local knowledge of the beautiful Aldinga Reef. I would also like to thank Yun Guang Jasper Wong, Chanveasna Ly and Md Mashiur Rahman Talukder for their, support in fieldwork. Thank you for your assistance, company, and for the friendships we forged through this research.
- To Asrath and Naseem for babysitting when I needed the most. Your encouragement and support cannot be thanked enough.
- To my family for their support, patience, encouragement when times were hard. I would like to thank my father for his encouragement and my children for their unconditional love and for being my motivation for learning.
- Thank you my most beloved husband Monchi, for being there for me always.

Thank you all for making this research project a success.

LIST OF FIGURES

Figure 1:1 <i>Ecklonia radiata</i> (Golden Kelp) in rockpools of Aldinga Reef (photo credit to Hussain (2021))	1
Figure 1:2 <i>Ecklonia radiata</i> distribution in the Great Southern Reef (GSR) (adapted image from (Bennett et al. 2016a) using data from (ALA 2021))	2
Figure 1:3 Aldinga Reef Encounter Marine Park Sanctuary Zone (data from NPSA (2016))	4
Figure 1:4 An image of Aldinga Reef at a low tide with its dune system on the foreground and the intertidal zone between the beach system and the sea (photo credit to Hussain, 2021)	5
Figure 1:5 Coastal Monitoring Profile Line 200054 over Aldinga Reef showing profiles from 1976 to 2018. It also shows highest and lowest astronomical tides (HAT and LAT) in AHD. The subtidal zone and intertidal zone are marked on the map along with the Zone I and Zone S used in this research (adapted from a figure developed by Michael Hillman (2021) using data acquired from NatureMaps (2021))	6
Figure 1:6: Storm water drains that end along the coastline adjacent to Aldinga Reef (data from DEW (2019))	7
Figure 2:1: Water absorption curve of the visible spectrum in water (Figure 12 in Pope and Fry (1997)	11
Figure 2:2 A simplified schematic of atmospheric interference and the passage of electromagnetic radiation from the Sun to the satellite sensor (Figure 7.1 in Green et al. (2020))	13
Figure 2:3 Life cycle of <i>Ecklonia radiata</i> (Figure 5 from Wernberg et al. (2019b))	22
Figure 2:4 Morphological stages of <i>E. radiata</i> (Figure 1.1 from Fairhead (2002))	23
Figure 2:5: A summary of factors that influence the distribution of Ecklonia species from literature	26
Figure 2:6 Reflectance spectra of <i>E. radiata</i> , <i>Sargassum</i> spp. and <i>S. doryocarpa</i> (adapted from Harvey (2009))	27
Figure 3:1: An overview of the methods used to collect data and analysis of images and mapping.	29
Figure 3:2 The shallow subtidal and intertidal zone (Zone I) and deeper subtidal zone (Zone S) where individual images were captured to estimate percent cover of <i>E. radiata</i> at Aldinga Reef	34
Figure 3:3: Location of rockpools used for validation at Aldinga Reef in 2020.	36
Figure 3:4: Dive Validation Areas in North, South and West of the study area at Aldinga Reef	38
Figure 3:5: An overview of georeferencing and mosaicking of all input data	39
Figure 3:6: Detailed flowchart of mosaicking and reprojection process to create mosaics for validation and mosaic of individual images that covered the whole study area	41
Figure 3:7: Spectral profile of broad benthic classes found in Aldinga Reef	42
Figure 3:8: Flowchart showing the image classification process using the Image Classification Wizard in ArcGIS Pro	42
Figure 3:9: Showing dive transect lines (in red) in each validation area in South, West and North subtidal areas	45
Figure 4:1: Classified validation transects in the West of the study area showing all classes within the area covered by the 10m buffered transect lines (WT1, WT2, WT3) of 30m in length each.....	51
Figure 4:2: Classified validation transects in the West of the study area highlighting <i>E. radiata</i> within the area covered by the 10m buffered transect lines (WT1, WT2, WT3) of 30m in length each.....	52
Figure 4:3: Classified validation transects in the South of the study area showing all classes within the area covered by the 10m buffered transect lines (ST1, ST2, ST3) of 30m in length each.	53

Figure 4:4: Classified validation transects in the South of the study area highlighting *E. radiata* within the area covered by the 10m buffered transect lines (ST1, ST2, ST3) of 30m in length each. 54

Figure 4:5: Classified validation transects in the North of the study area showing all classes within the area covered by the 10m buffered transect lines (NT1, NT2, NT3) of 30m in length each. 55

Figure 4:6: Classified validation transects in the North of the study area highlighting *E. radiata* within the area covered by the 10m buffered transect lines (NT1, NT2, NT3) of 30m in length each. 56

Figure 4:7: Classified validation transects in the North Shallow (NS) Rockpool..... 58

Figure 4:8: Classified validation transects in the West Shallow (WS) Rockpool 59

Figure 4:9: Classified validation transects in the West Deep (WD) Rockpool 60

Figure 4:10: Classified individual images over the study area 62

Figure 4:11: Reclassified individual images over the study area 62

Figure 4:12: This figure shows classified individual images in the West of the study area at the top, and unclassified RGB mosaic of the same area at the bottom. 64

Figure 4:13: Classified individual image in Northwest of the study area showing good classification of Ecklonia in shallow water and boxes showing good removal of sun glint..... 65

Figure 4:14: Sediment in shallow water misclassified as various classes..... 66

Figure 4:15: Exploring the relationship between accuracy and *E. radiata* detection using SVM changes with depth in rockpools (validation sites in zone I) 70

LIST OF TABLES

Table 3:1: A comparison of Mavic 2 Pro, Mavic 2 Enterprise, and Parrot Sequoia multispectral sensor (DJI 2018b, 2021a, 2021b; Pix4D 2018, 2021)	31
Table 3:2: Environmental factors recorded and observed to analyse the suitable conditions for collecting UAV images	32
Table 3:3: Description of zone created to capture individual images of the study area	33
Table 3:4: Description of rockpools used as validation areas in the shallow subtidal and intertidal zones (Zone I).....	36
Table 3:5 Description of areas for validation in the subtidal zone (Zone S)	37
Table 3:6: Classes of categories included in the schema for mosaiced image samples	43
Table 4:1 Summary of the ability of different sensor and bands to capture <i>E. radiata</i>	47
Table 4:2: A summary of how spectral and spatial detail changes with changes in image altitude.	48
Table 4:3: Summarises the environmental conditions that are favourable for <i>E. radiata</i> detection	50
Table 4:4: Percentage of <i>E. radiata</i> from SVM classifier for individual transects lines of each validation area (north, south, west) in the Deep Subtidal Zone (Zone S) and percentage of <i>E. radiata</i> for each validation area separately.....	56
Table 4:5: Percentage of <i>E. radiata</i> from SVM classifier for individual transects lines of all rockpools in shallow subtidal and intertidal zone (Zone I) and percentage of <i>E. radiata</i> for each rockpool separately.	61
Table 4:6: The percentage and area covered in <i>E. radiata</i> in the study area of Aldinga Reef.....	63
Table 4:7 Percent accuracy of the SVM classifier to detect <i>E. radiata</i> in the deep subtidal zone (Zone S).....	67
Table 4:8: Percent Accuracy of SVM classifier to detect <i>E. radiata</i> in shallow subtidal and intertidal zone (Zone I)	68

1 INTRODUCTION

This research explores the use of UAV (Unmanned Aerial Vehicle) images to estimate the percentage of *Ecklonia radiata* in Aldinga reef using a simple empirical classification model and the optimal environmental conditions to detect *Ecklonia radiata* from UAV images captured over water.

1.1 Rationale

Ecklonia radiata (*E. radiata*) is a subtidal brown macroalgae that can be found globally. It is a common kelp found in the temperate reefs of Australasia and southern Africa (Wernberg et al. 2019b). In Australia, *E. radiata* is commonly known as the Golden Kelp (ALA 2021) possibly due to its unique golden colour as seen in Figure 1:1. It is the most dominant macroalgae in the temperate reefs of Australia (Wernberg et al. 2019b). The presence of *E. radiata* is described as a significant feature of shallow temperate reefs of Australia, and its continuous span across 8000 kilometres of the southern coastline from Western Australia to New South Wales makes it a defining feature of the Great Southern Reef (GSR) (Bennett et al. 2016a) (see Figure 1:2). It is also considered the only laminarian kelp throughout its range that provides habitats, biodiversity and environmental services and hence is ecologically and socioeconomically very important (Wernberg et al. 2019b)

Image removed due to copyright restriction.

Figure 1:1 *Ecklonia radiata* (Golden Kelp) in rockpools of Aldinga Reef (photo credit to Hussain (2021))

Image removed due to copyright restriction.

Figure 1:2 *Ecklonia radiata* distribution in the Great Southern Reef (GSR) (adapted image from (Bennett et al. 2016a) using data from (ALA 2021))

Climate change has been a major threat to kelp forests throughout the world (Mabin et al. 2013). Despite the characteristic resilience of *E. radiata* to some temperature increase (Bennett et al. 2016a), it is reported that climate change related shifts such as the strengthening of the East Australian Current (EAC) and ocean warming, can affect the early development of the species (Mabin et al. 2013). Furthermore, there have been observed incidents of *E. radiata* loss to climate change resulting in turfing algae taking over those areas previously inhabited by *E. radiata* (Wernberg et al. 2019b). Therefore, studying the distribution patterns and understanding the factors that describe the distribution patterns of *E. radiata* is important for better understanding the species for climate change adaptation and mitigation.

South Australian Coastlines make up 50% of the GSR and there have only been a few large-scale surveys and studies (Brook et al. 2020; Cheshire & Westphalen 2000; EPA 1998; Turner, Kildea & Westphalen 2007) on the distribution of macroalgae in South Australia in recent decades. The aim of most of these studies such as Brook et al. (2020); Cheshire and Westphalen (2000); EPA (1998); Turner, Kildea and Westphalen (2007) was to assess the overall health of these rocky reefs and some of the recent studies used the presence of the broader macroalgae cover as an indicator of

reef health. However, there is a key research gap in terms of a focus on mapping kelp and specifically *E. radiata* in the South Australian context. Furthermore, most of the aforementioned studies that assessed reef health, except for EPA (1998), were based on data collection using field methods such as line transects by SCUBA divers which utilized a lot of human effort and time in collecting data. Yet, there are studies like EPA (1998) which has employed some aerial images to collect data. Aside from that early study, there are no other studies that have used mapping of *E. radiata* with optical remote sensing methods in South Australia.

The existing studies reported a lower cover of macroalgae in Adelaide Metropolitan Coastlines linking the decline with impacts from development of the coastline and lack of suitable benthic structure for settlement of spores (Brook et al. 2020; Turner, Kildea & Westphalen 2007). Turner., Kildea and Westphalen (2007) reported an abundance of larger brown macroalgae in Aldinga Reef between 1996 and 1999, and a significant increase in cover, between 30-40% from 1996 to 1999 in the area. However, the report by Brook et al (2020) observed a decline in brown macroalgae between 2017 and 2018. This observation of declines of macroalgae at Aldinga Reef is alarming especially because of its history of conservation since 1971 to date.

The gap in research on *E. radiata* in a South Australian context and from an aerial optical remote sensing perspective, makes this a significant area of interest for research. With the increasing impact of climate change on kelp populations, despite the high resilience of *E. radiata* to environmental change compared to other kelp species, there is an urgent need to map and observe changes more frequently. The potential of the species to adapt and mitigate the impacts of climate change, its ecological and socioeconomic significance, and its role in defining the GSR make it invaluable for future preservation of southern temperate rocky reefs. Aldinga reef has a reported high macroalgae cover, with *E. radiata* forming a large proportion of it, yet with the recent decline in canopy forming macroalgae is concerning considering the reef's conservation status as a Marine Park. Therefore, research with a purpose of using geospatial science to map the distribution of *Ecklonia radiata* (Golden Kelp) at Aldinga Reef, South Australia will be important for establishing easy-to-use, rapid monitoring (e.g using remote sensing) in future, which is the proposed aim of this study.

1.1.1 Research Objectives

The research objectives for the study are as follows.

1. To what extent does previous literature explain the optimum environmental conditions needed for benthic remote sensing using UAV imagery and the environmental conditions that contribute to variation in the distribution of *Ecklonia radiata*.
2. To what extent can *E. radiata* (Golden Kelp) be mapped using multispectral imagery;
3. What are the optimum observational conditions for mapping *Ecklonia radiata* using UAV imagery over Aldinga Reef? and;

4. What is the potential to estimate the percentage cover of *Ecklonia radiata* in Aldinga Reef using UAV multispectral imagery?

1.2 Study Area: Aldinga Reef

Aldinga Reef is a temperate limestone rocky reef at Aldinga in the Gulf of St. Vincent, South Australia (DENR 2010; Wegener 1995). The intertidal zone of Aldinga reef is of Tertiary age (Wegener 1995). Aldinga reef was declared an Aquatic Reserve in 1971 (Wegener 1995). With an area of 505 hectares, it was the largest Aquatic Reserve in South Australia when reported by Wegener in 1995. and it remains a large Marine Park Sanctuary Zone in Fleurieu Peninsula. Aldinga Aquatic Reserve falls under Encounter Marine Park (DENR 2010) due to the reef being an important nursery for a variety of organisms (Wegener 1995). Figure 1:3 shows the spatial extent of Aldinga Aquatic Reserve.

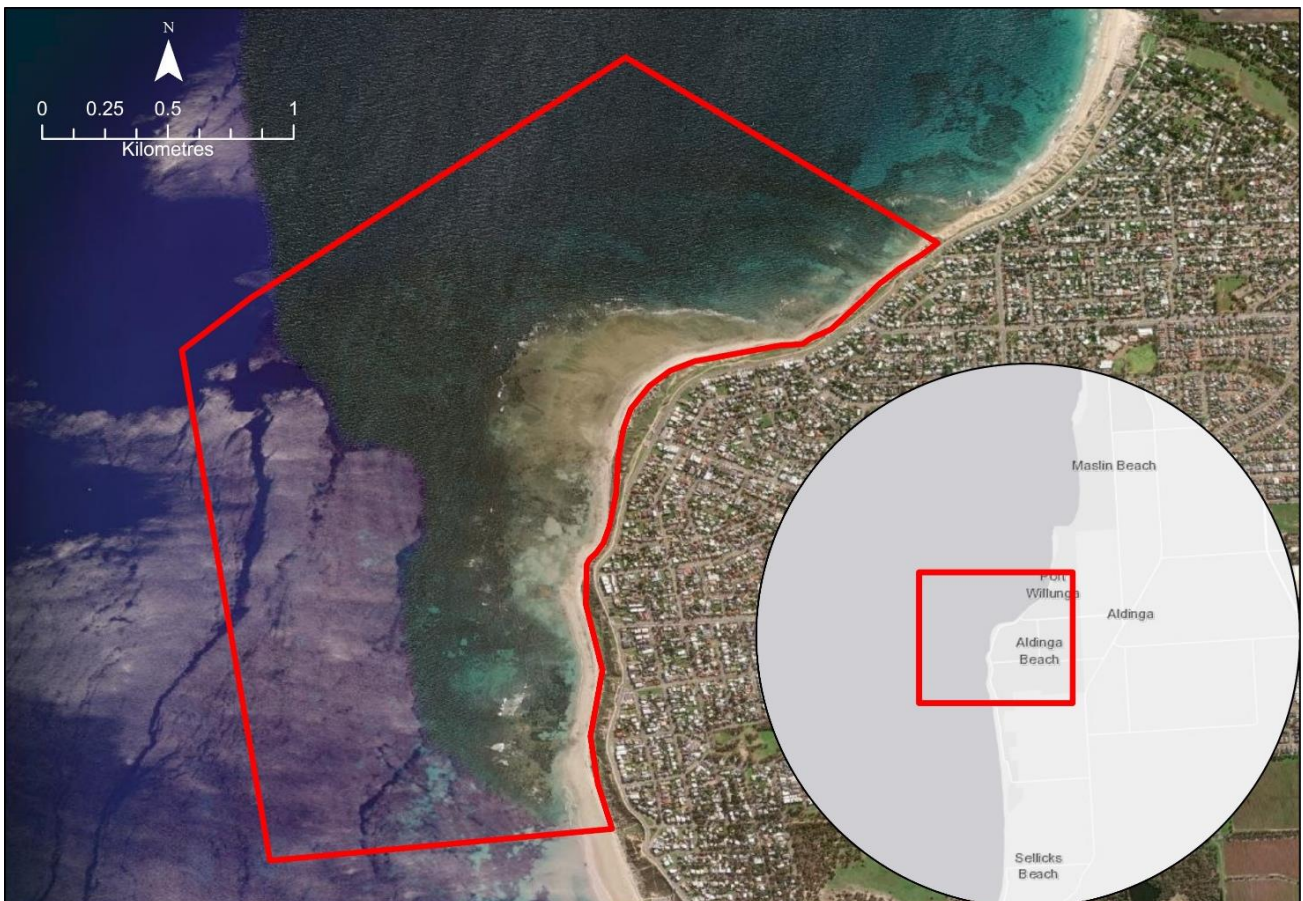


Figure 1:3 Aldinga Reef Encounter Marine Park Sanctuary Zone (data from NPSA (2016))

Aldinga Reef is divided into three distinct sections (Wegener 1995). The first section is the large and shallow intertidal platform which gets exposed during low tide (Wegener 1995) (see Figure 1:4). This area also has sandy rock pools (Wegener 1995) mostly located at the edges of the intertidal zone.

The second section is the subtidal zone extending out from the edge of the intertidal zone to the reef edge commonly known as “the drop off” (Wegener 1995). This reef edge is located around 500 meters out from the low tide range of the intertidal zone (Wegener 1995). The last section is the deep reef further out to sea (Wegener 1995).

Image removed due to copyright restriction.

Figure 1:4 An image of Aldinga Reef at a low tide with its dune system on the foreground and the intertidal zone between the beach system and the sea (photo credit to Hussain, 2021)

The information on the depth variation of Aldinga reef is not very comprehensive. According to Wegener (1995), the depth at which “the drop off” is located is 10 m. Clarke, et al. (2019) gave a general range of depth for Aldinga Reef between 10 m to 18 m and Cheshire and Westphalen (2000) divided the reef into Aldinga shallow (5-6 m depth) and Aldinga deep (12-12.5 m depth) based on where sampling was carried out in their studies. The reef platform is described as gently sloping with occasional outcrops (Cheshire & Westphalen 2000). A NatureMaps profile line that runs across Aldinga Reef (Figure 1:5) shows a depth profile along the line and the variation in depth over time. This profile may have been used to describe the depth variation by Wegener (1995) and Cheshire and Westphalen (2000). However, high spatial resolution bathymetry data that can show detailed depth variation in the reef is not available.

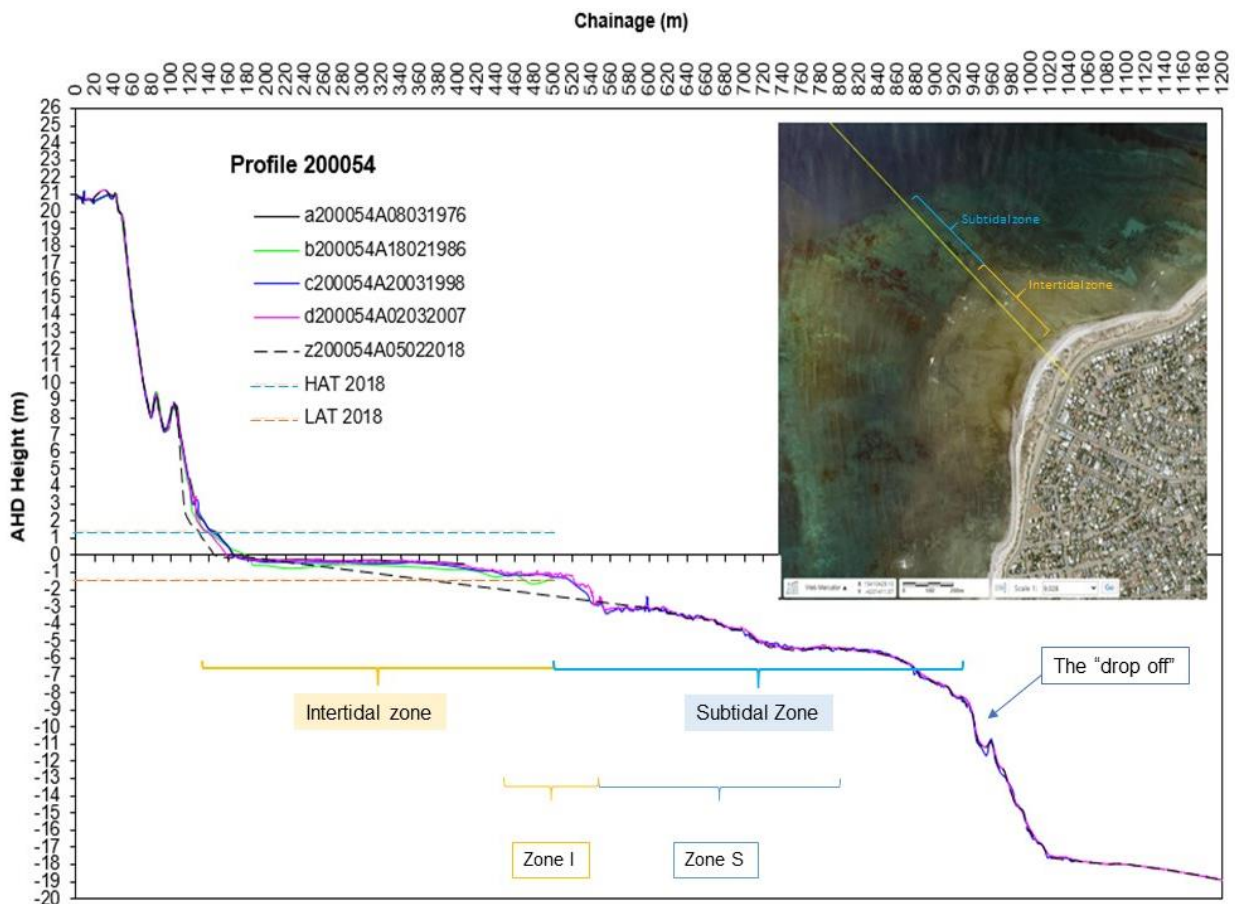


Figure 1:5 Coastal Monitoring Profile Line 200054 over Aldinga Reef showing profiles from 1976 to 2018. It also shows highest and lowest astronomical tides (HAT and LAT) in AHD. The subtidal zone and intertidal zone are marked on the map along with the Zone I and Zone S used in this research (adapted from a figure developed by Michael Hillman (2021) using data acquired from NatureMaps (2021))

The Gulf of St Vincent in which Aldinga reef is located is protected from swells from the Southern Ocean due to the location of Kangaroo Island at the mouth of the gulf (Short 2020). Its orientation blocks the entrance of swells except through the larger 40km Investigator Strait and through the narrower 14km Backstairs Passage (Short 2020). Therefore, the highest energy swells enter the gulf from a south westerly direction (250°) (Short 2020; Western et al 2021a). However, the energy from these swells is dissipated through wave refraction, diffraction, and bottom friction (Western et al 2021a) to generate low energy waves as it reaches Aldinga Reef (Western et al 2021b). In addition to the swells, the south-eastern coastline of the gulf is affected by wind generated waves that change direction seasonally from north-west in winter to south-west in summer (Short 2020). The contribution of sediment from rivers and creeks to the gulf is minimal (Western et al 2021a;b). The sediment drift direction along the eastern coastline is northwards (Short 2020; Western et al 2021a) with sediment deposited at three barrier systems where Sellicks-Aldinga is one of the smaller barriers systems (Short 2020). However, this sediment flow is predicted to decline in the future (Western et

al 2021b). As a result the net littoral drift of sediment is in the northerly direction along the coastline (McDowell, Green & Griffante 2009). Northward moving sediment plumes have been observed by Kinhill Engineers (1978; cited in Wegener 1995). Both Kinhill Engineers (1978) and Wegener (1995) state that the sediment from southern catchments, especially Sellicks Creek Catchment, impacts Aldinga Reef. Wegener (1995) identified stormwater drains as the main source of nutrients in Aldinga Reef waters but concluded that its impact was negligible. Furthermore, erosion of Aldinga soft sediment dunes is an issue highlighted in the Coastal Adaptation Study for the area (Western et al. 2020) Stormwater drains located in Aldinga can be seen in Figure 1:6

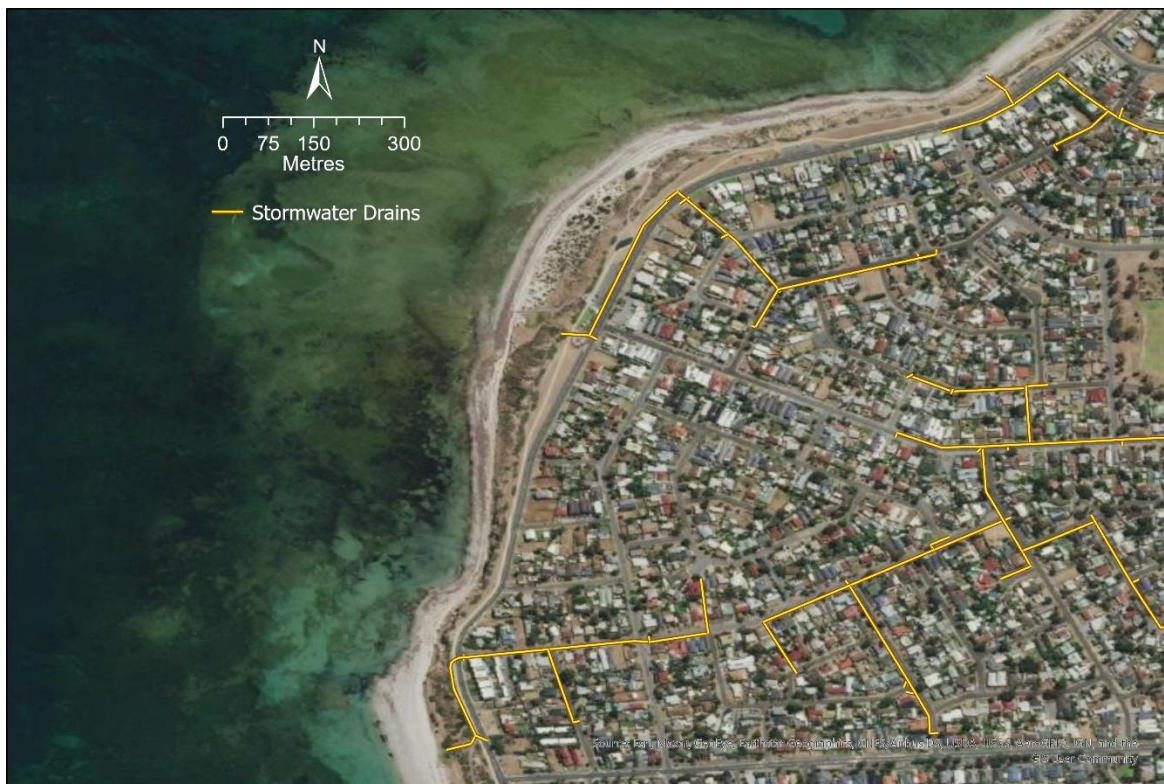


Figure 1:6: Storm water drains that end along the coastline adjacent to Aldinga Reef (data from DEW (2019))

Aldinga Reef is predominantly composed of brown macroalgae from the orders Laminariales and Fucales (Cheshire & Westphalen 2000). The most common brown macroalgae species present includes *Sargassum* spp, *Hormosira banksia* (seagrape) and *Ecklonia radiata* (Wegener 1995). Kinhill Engineers (1978; cited in Wegener 1995) observed that the subtidal zone of Aldinga Reef is dominated by *E. radiata* and Edyvane (2008) describe *E. radiata* as one of the dominant species along with others such as *Cystophora* spp. and *Sargassum* spp.. There are no studies that describe the detailed distribution pattern of *E. radiata* in Aldinga reef.

1.3 An Outline of the Thesis

The thesis will be structured into six chapters

Chapter 1: Introduction

This chapter introduces the research topic, explain the rationale and objectives of the research, introduces the study area, and include a brief outline of the thesis structure.

Chapter 2: Literature Review

This chapter is divided into three sections. The first section discuss literature on remote sensing methods that can be used to detect *Ecklonia radiata*. This section begins with the basic concepts of optical aerial remote sensing for benthic habitat mapping. This is followed by discussing the confounding issue of light attenuation and sun glint and the common methods used to overcome these issues. Finally, it focuses on the use of Unmanned Aerial Vehicles (UAV) for benthic mapping and the best practices and optimal environmental conditions for its successful use in benthic habitat mapping. The second section discuss image classification methods. It begins with an introduction of main classification methods and its uses and focus on machine learning algorithm Support Vector Machine (SVM). The third section is on *E. radiata*. This section deals with its classification, reproduction, factors that contribute to its distribution and its future threats. It also includes literature on the reflectance spectra of *E. radiata*.

Chapter 2: METHODS

Methods section explains the methods and the rationale behind selecting them. This section is divided into seven stages. Stage one is preplanning for fieldwork, followed by stage two; the preliminary survey to test out environmental conditions suitable for mapping *E. radiata* in Aldinga Reef. The third stage is the collection of UAV imagery over validation sites and in Zone I and Zone S of Aldinga Reef to estimate *E. radiata* percent cover. The fourth and fifth stages are pre-processing of imagery followed by image classification using supervised object-oriented Support Vector Machine (SVM) method. The sixth stage is *in-situ* data validation and the seventh is Accuracy Assessment.

Chapter 4 RESULTS

This section reports the results of the research from preliminary data collection, from classification outputs and from *insitu* validation and accuracy assessment. It reports the optimum environmental conditions for the mapping of *E. radiata* using UAV imagery in Aldinga Reef, the differences in the distribution of *E. radiata* observed in validation sites and the percentage cover of *E. radiata* in Zone I and Zone S of Aldinga Reef.

Chapter 5 DISCUSSION

In this chapter the results from the research will be discussed with the use of previous literature. The discussion will be used to establish the optimum environmental conditions required to map *E. radiata*, to explore the extent to which UAV RGB imagery can be used to map *E. radiata*, to link the variation in *E. radiata* distribution in validation site with possible factors that contribute to variation in its distribution, and discuss the accuracy at which *E. radiata* in Zone I and Zone S can be used to estimate the percent cover of *E. radiata* in Aldinga Reef.

Chapter 6 CONCLUSION AND RECOMMENDATION

This chapter summaries key findings in terms of the research objectives. It summaries the discussion of the optimum environmental conditions for *E. radiata* mapping using UAV imagery, the extent to which UAV imagery can be used to map *E. radiata* and the accuracy at which *E. radiata* can be estimated in Zone I and Zone S of Aldinga Reef along with the estimated values.

2 LITERATURE REVIEW

2.1 Remote Sensing of *Ecklonia radiata*

The traditional method of biodiversity monitoring involves sampling a small area of a reef using quadrat or transect samples (Underwood 2000). Although this method is accurate to estimate an overall species cover, it does not provide information on smaller scale variations in the reef structure that may contribute to variation in the distribution of species (Murfitt et al. 2017). Furthermore, replicating the data collected over intertidal zones with variable wave and tide conditions, can be labour intensive, time consuming, and therefore expensive (Murfitt et al. 2017). Optical remote sensing is a proposed rapid method solution to this problem.

2.1.1 Remote Sensing and Types of Resolution

Remote sensing data are collected using passive or active remote sensing methods. Passive remote sensing is when a sensor records electromagnetic radiation emitted from the target to observe and study it (Jensen 2015). On the other hand active remote sensing involves the use of an active sensor which is one that emits energy such as radio waves (in RADAR), light (in LiDAR) or sound (in SONAR) and then the time taken for radiative flux to get scattered back to the sensor is measured (Jensen 2015). This study focuses on the use of passive optical sensors for collecting data.

Spectral resolution is the size of wavelength intervals (also known as bands or channels in the electromagnetic spectrum that the remote sensing instrument is sensitive to (Jensen 2015). The term hyperspectral is used to refer to a sensor that usually has more than 100 bands (Hedley, J et al. 2016). While multispectral sensors are those that record multiple bands and multiple bands, which are typically 4 to 5 bands including the visible and infrared bands (Jensen 2015).

Spatial resolution refers to the measurement of the smallest angular or linear separation between two objects that can be resolved with remote sensing (Jensen 2015). This smallest unit is usually observed in digital imagery as rectangular pixels and the measurement of their dimensions (for example 1m x 1m) on ground is used to describe the spatial resolution of an image (Jensen 2015). Spatial resolution of imagery can be divided based on pixel sizes into very high (<1m), high (1-10m) moderate (10-100m) and low (100-1000m) (Hedley et al. 2016). Higher spatial resolution imagery usually covers smaller areas in space (less than 100km²) in comparison to moderate and low spatial resolution imagery (10,000s km²) (Hedley et al. 2016).

Radiometric resolution describes the sensitivity of a sensor to detect differences in signal strength when recording radiant flux and is quantified in digital image outputs as number of bits (Jensen 2015). Temporal resolution describes the frequency of resampling on a specific location by a sensor (Jensen 2015). This review will focus more heavily on spectral and spatial resolution.

2.1.2 Benthic Habitat Mapping using optical remote sensing

Benthic habitat maps record the spatial location of areas that are associated with certain species, their communities and its assemblages (Harris & Baker 2012). It is useful for applications such as marine environmental management and identifying areas for conservation which is useful information for decision makers (Harris & Baker 2012) Benthic habit mapping using passive optical remote seeing methods use the visible wavelengths of the electromagnetic spectrum (i.e. wavelengths approximately between 400-740nm), because it is the wavelengths within the visible spectrum that penetrates water (Hedley et al. 2016). Therefore, optical remote sensing methods for benthic mapping are restricted to shallow water environments that can be penetrated by visible light (Brown et al. 2011)

2.1.3 Light attenuation in water

Image removed due to copyright restriction.

Figure 2:1: Water absorption curve of the visible spectrum in water (Figure 12 in Pope and Fry (1997))

Light attenuation is the process of the exponential loss of light intensity as it enters water (Green et al. 2000). Loss of light intensity is quantified by a coefficient c , that is measured in unit per meter (Davies-Colley et al. 2014). The cause of this loss of light energy is absorption and scattering of light (Green et al. 2000). Absorption of a wavelength removes it altogether whereas scattering changes the direction and propagation of the light beam increasing its chances of getting absorbed (Gallegos & Moore 2000). Figure 2:1 shows the absorption of visible spectrum in pure water. Absorption is mostly caused by the water column itself, suspended and dissolved material in the water and the underlying substrate and benthos (Green et al. 2000). Scattering is caused by inorganic or organic

particulate matter, and suspended load such as sediment in the water (Green et al. 2000). The rate of energy loss from light attenuation varies for different wavelengths (Green et al. 2000). For example, the red band of the visible spectrum attenuates faster than the shorter waved blue band (Green et al. 2000). As a result of this process, the separability of substrates and benthos based on spectra declines with increasing depth of water and consequently the spectral signature of the same substrate is different in shallower water verses deeper water (Green et al. 2000).

Light attenuation from pure water alone can vary for different wavelengths and with depth (Gallegos and Moore 2000). Gallegos and Moore (2000) states that light attenuation due to water alone was recorded as 0.038m^{-1} by Lorenzen's (1972). Gallegos (1994) shows how light attenuation changes from $0.16\text{-}0.13\text{m}^{-1}$ when water depth is varied from 1 to 3 meters.

Fine mineral sediments, organic matter, and particles, especially in eutrophic water attenuates lights strongly by scattering of light (Davies-Colley et al. 2014). The scattering is stronger with the presence of fine particles and this peaks at around $1.2\mu\text{m}$ in diameter for near spherical mineral sediments, and his value is different in organic matter because of changes in density and reflective index (Davies-Colley et al. 2014). The light scattering peaks at around $5\mu\text{m}$ in organic particles such as phytoplankton cells and detritus (Davies-Colley et al. 2014).

Turbidity of water can increase the sediment load in water and in turn increase the scattering of light (Green et al. 2000). Turbidity in many coastal areas generally increases in a seaward direction with increase in depth of water, however it cannot be generalised as many other factors contribute to variability in turbidity of coastal areas (Green et al. 2000)

Therefore, the spectral radiance captured by a sensor depends on both the reflectance measured and the water depth at which it is located, light attenuation from suspended and dissolved particles and light absorption by various benthic components underneath (Green et al. 2000). As a result, attenuation of light in water is a challenge when using a remote sensor over water to map the substrate and benthos underneath due to the confounding effect of changes in spectral signature with increasing depth (Green et al. 2000).

2.1.4 Water Column Correction

The impact of light attenuation on the reflectance spectra because of increasing water depth, can be removed if depth and water attenuation characteristics of the waterbody can be acquired (Green et al. 2000; Mumby et al. 1998). Usually, depth information is required for each pixel of the image collected and therefore bathymetry data or a good digital elevation model that corresponds to pixel level detail of the image is required (Green et al. 2000; Mumby et al. 1998). However, acquiring accurate field bathymetry data is a challenging process in shallow water coastal environments (Kutser et al. 2020). Acquiring field survey data, such as echosounder data using a sea vessel, is

challenging because of the difficulty to access shallow water with the danger from reef structures and rocks (Kutser et al. 2020). Bathymetry data from satellite and aerial imagery may cover a larger extent in area (Agrafiotis et al. 2019) but they are not very useful to correct light attenuation in water of very high spatial resolution images due to mismatch of bathymetry and image pixels (Green et al. 2000) (i.e. with the large pixel sizes in satellite and aerial image derived bathymetry). UAV derived bathymetry is a time consuming and a costly process (Agrafiotis et al. 2019). Yet it is being considered a more efficient method of bathymetry data collection in shallow waters of less than 10 metres, even though image-based bathymetry is heavily influenced by wave action and water clarity (Agrafiotis et al. 2019)

2.1.5 Atmospheric effects

Image removed due to copyright restriction.

Figure 2:2 A simplified schematic of atmospheric interference and the passage of electromagnetic radiation from the Sun to the satellite sensor (Figure 7.1 in Green et al. (2020))

Scattering and absorption of light is not only an issue in the water column but also initially occurs in the atmospheric column even before reaching the water (Green et al. 2000) (see Figure 2:2). Absorption of light occurs by gas particles such as carbon dioxide, ozone and water vapour molecules and other aerosols (Green et al. 2000). The aerial and satellite remote sensing methods try to use wavelengths with minimum absorption, which are known as transmission windows (Green et al. 2000). This includes visible to near infrared (300-1300nm), middle infrared (1500-1800 nm, 2000-2500 nm and 3500-4100 nm) and thermal infrared (7000–15000 nm) (Green et al. 2000). Scattering of light in the atmosphere occurs as a result of its interaction with atmospheric gasses and water vapour (less than 100µm), most other airborne particles or aerosols (usually greater than 1µm) and rain droplets and ice (greater than 10µm) (Green et al. 2000). Atmospheric absorption and scattering causes haziness in imagery as pixels in the image incorporate the scattered reflectance from the neighbouring pixels or adjacency effect (Green et al. 2000).

2.1.6 Atmospheric Correction or Radiometric Correction

Atmospheric correction can be used to address some of the problems with scattering and absorption of light and is usually carried out through three approaches; removal of path radiance, direct calibration using field-derived reflectance and atmospheric modelling (Green et al. 2000) such as the radiative transfer model (Schläpfer, Popp & Richter 2020). Removal of path radiance involves the removal of scattering effects by establishing the path radiance with the use of prior to band ratioing to cancel out atmospheric transmittance and topographic effects (Green et al. 2000). Field derived reflectance methods measure reflectance of two or more regions of the area with the use of a spectral radiometer on field and convert the image acquired to reflectance using a linear extrapolation method (Green et al. 2000). Atmospheric modelling is a complex method that uses existing knowledge of the amount of atmospheric absorption and scattering to develop a model that can predict the result of electromagnetic radiation acquired by the sensor and then uses this to correct the issue on the image (Green et al. 2000).

The atmospheric issues presented by different sensors capturing imagery at varying altitude have many similarities such as absorption and scattering by aerosols, water vapour and other gases but there are differences to some extent (Schläpfer, Popp & Richter 2020). For instance, satellite imagery are affected by factors such as cloud cover along with scattering from aerosols and its related adjacency effect which is stronger because of the low spatial resolution of images (Green et al. 2000; Tait et al. 2019). In contrast, due to the low flying altitude of UAVs, the adjacency effect is reduced. Furthermore, due to the low spatial extent of images captured from UAVs, the aerosol and water vapor effect may be considered constant (Schläpfer, Popp & Richter 2020). Such differences lead the development of separate atmospheric models such as the DROACOR model by Schläpfer, Popp and Richter (2020), which is a very new area of research.

2.1.7 Confounding Effect of Sun-glint

Other than the complex issue of light attenuation and water depth the most confounding issue when collecting images over water is sun glint. Sun glint is defined by Kay, Hedley and Lavender (2009) as the mirror like reflection generated over water by the direct reflectance of sunlight from the surface of water. It is captured as bands of bright white reflectance over water when the sun is bright but the water is not flat due to wave movement (Hedley, Harborne & Mumby 2005; Mustard, Staid & Fripp 2001). Any information underneath these white bands is lost (Hedley, Harborne & Mumby 2005) limiting the amount of data captured and its accuracy (Kay, Hedley & Lavender 2009). Therefore, sun glint is a major issue that affects the image classification process and its accuracy (Hedley, Harborne & Mumby 2005). Sun glint is formed on the windward side of waves (Hedley, Harborne & Mumby 2005) and is influenced by wind speed, the length and height of the waves, swell conditions and should coincide with favourable sun angle or viewing geometry (Mustard, Staid & Fripp 2001; Tait, Orchard & Schiel 2021)

2.1.8 Sun-glint removal

There are various methods used to remove sun glint from images captured over water. These methods were divided into two broad classes by Kay, Hedley and Lavender (2009). The first set of methods uses radiative transfer models along with statistical models of the state of the sea to predict the amount of light reflected from the water surface. The statistical models predict the probability of sea surface roughness causing sun glint using the speed and direction of the wind (Kay, Hedley & Lavender 2009). The speed of the wind is assumed to be related to roughness of the sea surface (Cox & Munk 1954). This method is usually used for imagery with larger pixel sizes (Kay, Hedley & Lavender 2009).

The second method is applicable for images with pixel sizes smaller than 10m (Kay, Hedley & Lavender 2009). It uses reflectance from (Near Infra-Red) NIR which is rapidly absorbed by water and therefore is used as a proxy of the amount of sun glint in a pixel (Kay, Hedley & Lavender 2009). This method assumes NIR is rapidly absorbed by water (Kay, Hedley & Lavender 2009). However, in shallow waters with aquatic vegetation such as seagrasses and macroalgae, NIR and parts of SWIR of the spectrum is reflected as all types of vegetation have a high reflectance in this spectrum (Kutser, Vahtmäe & Praks 2009). This is especially true if the vegetation reaches the water surface or is separated by a thin layer of water in shallow water environments. (Kutser, Vahtmäe & Praks 2009). Some methods such as the de-glinting algorithm by Hochberg, Andrefouet and Tyler (2003) uses Near Infra-Red (NIR) to remove sun glint. When NIR is not available sun glint can be removed from hyperspectral images by using the depth of the oxygen absorption feature at 760 nm which is assumed to be proportional to the amount of glint in the pixel (Kutser, Vahtmäe & Praks 2009).

Sun glint can also be removed by a much simpler method by flying the sensor towards or away from the sun as explained by Mustard, Staid and Fripp (2001). It is recommended to carefully plan the flight to ensure the implementation of sun glint reduction considerations such as setting the flight path to head towards or away from the sun when the sun altitude is 30-60° (Mustard, Staid & Fripp 2001). However, Mount (2005) explains that the recommended time frame for capturing nadir images (pointing vertically straight down) is very limited because of the effects created by the water surface due to sun angle, reflection and refraction. The time frame recommended by Mount (2005) is a very short duration in the morning when the sun angle is high enough to illuminate the water but before it is too high to cause sun glint and before the sea breeze starts for the day. Mount (2005) disagree with Mustard, Staid and Fripp (2001) regarding images captured above sun altitudes higher than 30-35°. Mount (2005) explains that nadir images that are captured when the sun angle is greater than 30-35° are likely to capture sun glint in the direction of the sun azimuth. Furthermore, images captured with wind speed greater than 9 to 18 km/hr will contain sun glint because of glitter diameters and increased multiple scattering (Mount 2005). However, when sun angle is lower than 20-25° sunlight penetrating the water is limited (Mount 2005). Therefore Mount (2005) establishes that a sun altitude between 20-30° is the ideal time for nadir image capture and this agrees with recommendations from (Joyce et al. 2019).

2.1.9 UAV Image Capture Over Shallow Water

Several factors such as need of the user, scale of the study area, availability of funds and resources and the skill of the user influence the selection of the remote sensing method for data collection (Lu & Weng 2007). However, the most important factor is the spatial extent and image resolution at which the user needs information (Lu & Weng 2007). Despite advancements in satellite imagery, easily accessible satellite imagery does not provide the high spatial resolution that is suitable for benthic mapping of reefs (Roelfsema et al. 2018a). Consequently, to map reef habitats there is a need to acquire expensive commercial satellite imagery for larger spatial extent or UAV imagery for smaller spatial extent (Joyce et al. 2019; Roelfsema et al. 2018a). Furthermore, satellite imagery over shallow water environments are affected by factors such as cloud cover, aerosols in air and poor synchronisation with ideal tidal conditions (Tait et al. 2019). UAVs (Unmanned Aerial Vehicles), are known as Remotely Piloted Aircrafts (RPAs) or drones, have the high spatial resolution which can be adjusted to the users need by varying the flying altitude to very fine accuracies (eg mm to cm accuracy) (Flynn & Chapra 2014; Riniatsih et al. 2021). High spatial resolution reduces the issue of misclassification (Lu & Weng 2007). It provides control and flexibility for the user to deploy it at the exact time and place of interest and at every frequency needed (Joyce et al. 2019). This control by the user solves some traditional issues such as poor synchronisation with desired tides and weather conditions that satellite images commonly present (Tait et al. 2019). However, some advantages such as the ability to capture more detail from low flying altitudes presents other issues like shadow

(Lu & Weng 2007). Furthermore, the need for textual and contextual information becomes more significant in the image classification process (Lu & Weng 2007).

2.1.10 Environmental Conditions for Image Collection Over Shallow Water

Image capture over shallow water for benthic habitat mapping is challenged by issues such as light attenuation in water, which is primarily based on depth of water and complicated by factors such as water turbidity, sedimentation, and nutrient load (Davies-Colley et al. 2014; Gallegos & Moore 2000; Green et al. 2000). Therefore, it is no surprise that it is recommended to collect images at the lowest tide possible over shallow water (Tait, Orchard & Schiel 2021) and to avoid capturing images when water is turbid to improve visibility (Tait et al. 2019). It is recommended to fly the sensor when wind speeds are lower than 18 km/hr and when the sun altitude is ideally between 25° to 35° with the sensor moving towards or away from the sun azimuth to minimise the effect of sun glint in nadir images (Mount 2005; Mustard, Staid & Fripp 2001).

2.2 Image Classification

Image classification usually begins by identifying an appropriate classification algorithm, pre-processing of images, training the algorithm, image processing to extract features, and accuracy assessment (Lu & Weng 2007). Some of the major types of digital image processing includes image pre-processing (i.e. that includes radiometric and geometric correction), image enhancement, photogrammetric image processing of stereoscopic images, and parametric and non-parametric information extraction, expert system (eg decision tree) and neural network image analysis, hyperspectral data analysis and change detection (Jensen 2015). This review will touch upon image pre-processing and major image classification methods.

2.2.1 Image pre-processing

Radiometric correction involves correcting the effects of noise introduced into the system from the sensor and from the environment; for example from atmospheric scattering of light which can be usually corrected by simple normalisation techniques or more advanced absolute radiometric calibration of the data to scaled surface reflectance (Jensen 2015).

Geometric correction involves positioning imagery into its correct planimetric position in a standard map projection (Shepherd et al. 2014) to ensure accurate use of imagery to extract spatial information (Jensen 2015) such as area of coverage by a habitat. Two most common geometric correction includes, georeferencing and mosaicking. Georeferencing is aligning an image to its geographical coordinate system so that what is measured on the image represent measurements on ground (Selvaraj 2021). This is most accurately done when targets are captured in imagery with that represents ground control points (GCPs) which have known coordinate location values (usually measured with RTK equipment of handheld GPS systems with accurate positioning capability

(Selvaraj 2021). Mosaicking is the process aligning together multiple such georeferenced images into one image (Selvaraj 2021). This is usually done with software such as Pix4D Mapper that can automatically perform radiometric calibration, geometric corrections, georeferencing and mosaicking (Selvaraj 2021).

2.2.2 Key Image Classification Approaches

Image classification methods have been grouped in various ways. Lu and Weng (2007) classify types of image classification to supervised or unsupervised approaches, parametric and nonparametric classifiers, hard and soft (fuzzy) classification, pixel classification, empirical and knowledge or physics based and various combining various approaches. All the various groupings of classification will not be discussed here. This review will discuss the relevant classification approaches for my study that includes visual interpretation, supervised and unsupervised classification, parametric and non-parametric classification, pixel and spectral classification, object-oriented classification and will finally focus on machine learning and Support Vector Machine (SVM) classifier.

Visual Interpretation

Visual interpretation is an image classification method for benthic mapping began with visual interpretation of aerial photography with habitats identified and marked to create habitat maps (Kutser et al. 2020). This method, although subjective, is still practiced in shallow water benthic mapping because the ability of an expert to visually interpret benthic habitats from images cannot be challenged by developments in artificial intelligence technologies such as machine learning or deep learning (Kutser et al. 2020). However, machine interpretation and quantification methods of digital imagery has the advantage of automation and the reduction of effort from the user increasing productivity and repetition (Kutser et al. 2020)

Supervised and Unsupervised Classification

Automated image classification in benthic mapping can either be supervised or unsupervised (Kutser et al. 2020). Unsupervised classification is when the algorithm delineates classes based on mathematical principles of clustering and similarity initially to as many classes possible (Hedley et al. 2016; Kutser et al. 2020). These classes are then grouped if needed and named by the operator based on fieldwork or experience (Green et al. 2000). Image classification can be supervised when the classifier is provided guidance of what is found where (Hedley et al. 2016). This guidance can come from fieldwork which may be used to train the classifier to identify classes (Roelfsema et al. 2018b). For both supervised and unsupervised classification there is a need to collect a large amount of field data preferably over the areas where image data was collected (Kutser et al. 2020). These empirical classification methods are robust and easy to use but are usually sensor and image specific, require a large amount of field data, results cannot be transferable from image to image, or

sensor to sensor and water depth and benthic data cannot be collected simultaneously (Kutser et al. 2020).

Parametric and Nonparametric Classification

Parametric classification algorithms assume that observed measurement vectors obtained for each class in each spectral band during the training phase of the supervised classification are Gaussian, as they are normally distributed (Schowengerdt 2007). However, pixel distribution does not follow a normal curve in most natural environments (Lu & Weng 2007). Conversely nonparametric classification algorithms make no such assumptions and are therefore more suitable to incorporate non-spectral data into its classification process (Lu & Weng 2007). One of the most used non-parametric classifiers is Support Vector Machine (SVM). Nonparametric classifiers are considered to generate better classification outputs than parametric classifiers (Foody 2002).

Per-pixel and spectral classification

Per-pixel method classifies each and every pixel of an image based on its spectral characteristics (Lu & Weng 2007). These pixels are then sorted into to groups depending on their spectral characteristics (Lu & Weng 2007). The assumption made in the categorisation process can make a per-pixel classification method either parametric or nonparametric (Lu & Weng 2007). Per-pixel classification results in noisy outputs, especially in complex physical landscapes and environments, due to the variation in spectral reflectance that exists within a single class (Lu & Weng 2007).

Object Oriented Classification

Object oriented classification takes place in two stages, of image segmentation and classification. Image segmentation is when pixels of similar spectral attributes are combined into objects called segments and these segments are used in the classification process rather than the pixels (Lu & Weng 2007). Using segments in the classification results in better outputs especially when working with high spatial resolution imagery (Lu & Weng 2007)

A more recent addition to classification methods is object-based image analysis (OBIA). OBIA segments the imagery into smaller objects or polygons with similar spectral, textual and thematic properties (Kutser et al. 2020) and classifies them into groups based on membership rules (Blaschke, T. 2010). The backbone of OBIA is segmentation of imagery, which has existed for a long time (Blaschke, T. 2010). More recent OBIA methods have combined the physics-based method or use knowledge of depth, slope and wave climate (Roelfsema et al. 2018a; 2018b) to differentiate habitat classes at various levels (Kutser et al. 2020)

Segments are areas that have been created based on homogeneity of one or more dimensions of the dataset (Blaschke, T. 2010). Therefore, segments have an additional layer of spectral information

such as mean values per band of the feature, maximum and minimum values, means, variance etc., as opposed to single pixel information. This diverse set of spectral information is more importantly linked to a spatial object called a segment (Blaschke, Thomas & Strobl 2001).

Knowledge based or Physics based Classification

The disadvantages of the empirical methods of classification can be dealt with by using physics-based methods of image classification (Kutser et al. 2020). These methods model the physical properties of the environment and targets for instance uses reflectance spectra of all substrates and benthic classes at varying depths and at varying optical types of water (Kutser et al. 2020). The classes are then simultaneously separated based on classes of variation and depth using a spectral matching method. Because the broad information in the models used about reflectance's and bottom types are relatively consistent throughout the world, there is no need to carry out fieldwork to capture the coarse information (Kutser et al. 2020).

Knowledge based classification (physics-based classification) incorporates ancillary data (i.e. digital elevation models, bathymetry data, water attenuation models and spectral reflectance data) into the classification in different ways (Lu & Weng 2007). This extra layer of information that describes the complex spatial relationship classes have with the physical environment is used to improve the classification outcome (Lu & Weng 2007). Knowledge based approaches are becoming increasingly popular due to their ability to incorporate multiple ancillary data, however the selection of such a classification method depends on the availability of the ancillary data, software, equipment and resources, the analysts experience, and time available for the project (Lu & Weng 2007)

2.2.3 Machine Learning and SVM

Machine learning is defined as the capacity of solving a given problem with the use of examples provided before (Jo 2021). The building of this problem-solving capacity is called training and the process of doing it is called learning (Jo 2021). Support Vector Machine (SVM) is defined as the dual hyperplane classifier with the maximum margin in the mapped space that is called feature space (Jo 2021). The SVM that is derived from a single linear classifier, which is called a Perceptron, is intended for solving nonlinear classification problems (Jo 2021).

A hyperplane is a classification boundary in the simple machine learning algorithms. It is a line in the two-dimensional space or a plane in a three-dimensional space that separates two classes (Jo 2021). It is expressed as a linear combination of products, each of which consists of a variable and a coefficient, which becomes a boundary between the positive class and negative class (Jo 2021). The learning process of the hyperplane is to manipulate the coefficients for minimising the misclassification or the error (Jo 2021). Linear separability is defined as the situation where examples are separable category by category by a hyperplane that is expressed as a linear combination (Jo

2021). Even if the training examples are classified perfectly there is no guarantee that training examples from a novice are classified correctly (Jo 2021). This issue becomes the motivation for making the idea of the Support Vector Machine (Jo 2021). Nonlinear separability is more common than linear separability, thus the Perceptron was expanded into the Multiple Layer Perceptron (MLP) and Support Vector Machine (Jo 2021) The kernel function is defined as the similarity metric or the inner product between two vectors in the mapped space (Jo 2021). When a scale value results from applying the inner product or vector in any dimension, the similarity or the inner product of two vectors in the feature space through kernel function can be computed without mapping individual vectors in the original space into ones in the feature space (Jo 2021). Mapping the original space with its nonlinear separability into the feature space with the linear separability is originally the idea of the SVM (Jo 2021)

Support Vector Machine (SVM) is a supervised machine learning model with associated learning algorithms that analyse data used for classification and regression analysis (Mahesh 2020). SVM can perform linear classification and nonlinear classification using what is called a kernel trick, implicitly mapping inputs into high dimensional feature spaces (Mahesh 2020). It basically draws margins between the classes (Mahesh 2020). The margins are drawn in such a fashion that the distance between the margins and the classes is maximum and hence, minimising the classification error (Mahesh 2020)

2.3 Golden kelp *Ecklonia radiata* in southern Australia

Ecklonia radiata is the most commonly found seaweed or kelp in Australia (Wernberg et al. 2019b). It is commonly known as Golden Kelp (ALA 2021) because of its distinctive golden colour. Seaweed species, such as *E. radiata*, that belong to the order Laminariales, are commonly grouped as kelp, macroalgae or brown algae (Bolton, 2016). They can be found across the world and especially in temperate and polar coasts where they are ecologically important habitat forming species (Filbee-Dexter et al. 2019). *E. radiata* is a dominating feature of temperate reefs throughout Australasia and south-eastern Africa (Wernberg et al. 2019b). The rocky temperate Australian coastline forms an interconnected temperate rocky reef system known as the Great Southern Reef (GSR) (Layton et al. 2020). Kelp forests dominate these rocky reefs and form complex and ecologically important habitats with high biodiversity and endemism which provides significant ecological and socioeconomic services (Layton et al. 2020). *E. radiata* is also the main type of kelp in GSR, making it a defining feature of the reef (Wernberg et al. 2016a). Further, *E. radiata* is the only laminarian kelp in most of its distribution and forms large areas of monospecific forests (Wernberg et al. 2019b). In Australia, the GSR and the dominant *E. radiata* forests, contribute \$10 billion per year to the GDP (Bennett et al. 2016b). Also, Aboriginal Australians use kelp from GSR as a source of food, for making utensils including water carriers, and have used the kelps fronds as footwear and as a

therapy for sore feet (Akerman 2005; Clarke, PA 2011; Wessen 2009). Furthermore, they have been used in Aboriginal cultural events and ceremonies (Wessen 2009).

2.3.1 Classification and reproduction

Laminarian kelps emerged in the northern hemisphere around 80 million years ago (Wernberg et al. 2019b). However, the *E.* genus emerged in the southern hemisphere more recently around 25 million years ago (Silberfeld et al. 2010). It is believed that *E. radiata* emerged in the shallow waters of Australia less than 3 million years ago (Durrant et al. 2015).

Ecklonia spp has previously been classified into different families such as Laminariaceae, Alariaceae and Lessoniaceae, but today its placed in the new family; Arthrothamnaceae (Jackson et al. 2017). Recent studies conclude that *Ecklonia* spp. from the northern and southern hemisphere emerged from two separate clades and all southern hemisphere samples except for the South African *Ecklonia maxima*, formed the single species *E. radiata* (Rothman et al. 2015).

Image removed due to copyright restriction.

Figure 2:3 Life cycle of *Ecklonia radiata* (Figure 5 from Wernberg et al. (2019b))

The life cycle (Figure 2:3 and Figure 2:4) of *E. radiata* begins with the formation of zoospores within the tissue of the main lamina and at the base of the laterals (Wernberg et al. 2019b). This development can be identified as slightly raised and discoloured patches of tissue along the lamina (Wernberg et al. 2019b). The seasonal timing of this process seems to vary geographically (Wernberg et al. 2019b). In Western Australia this process peaks between January and May and is directly related to seawater temperatures (Mohring et al. 2012). However, in Tasmania this process occurs throughout the year and peaks in autumn and winter when temperature is lowest (Sanderson 1990). The released zoospores settle and grow into separate male and female gametophytes (Wernberg et al. 2019b). The zoospores have the capability of dispersal in the water column for more than 24 hours before settling to the substratum to germinate (Mohring et al. 2014). Gametophyte recruitment peaks between 16-20°C and declines with increasing temperatures (Mohring et al. 2014) and in low light intensity that is usually related to high cover of understory algae (Tatsumi & Wright 2016). Furthermore, sedimentation, scour (Tatsumi & Wright 2016), grazing and pollutants are considered factors that negatively affect gametophyte recruitment (Wernberg et al. 2019b). The next stage is sperm dispersal and where oogonia or female gametophytes are fertilised and juvenile microscopic and macroscopic sporophytes are formed (Wernberg et al. 2019b). Less than 0.6% survive this transformation from microscopic to macroscopic sporophytes (Tatsumi & Wright 2016), yet the ones that do get through this transformation have a high chance of survival as adults (Wernberg et al. 2019b). After settlement, *E. radiata*, undisturbed, is considered to have a lifespan of around seven years (Schiel & Choat 1980).

Image removed due to copyright restriction.

Figure 2:4 Morphological stages of *E. radiata* (Figure 1.1 from Fairhead (2002))

2.3.2 Distribution and factors that contribute to distribution of *Ecklonia* species

Ecklonia species can be found distributed across various global latitudes within temperatures ranging between 8 to 25°C (Bolton & Anderson 1987). However, its distribution is strongly related to temperature and substratum availability (Marzinelli et al. 2015). *E. radiata* is found in temperate to subtropical reefs across Australia (Womersley 1984) including reefs along the open coast and within estuaries and can even be found growing on artificial structures such as jetties (Coleman, Melinda A. 2013). Further, *E. radiata* is normally found in subtidal zones although it is occasionally found in intertidal zones (Wernberg et al. 2019b). This broad distribution of *E. radiata* gives reason to believe that it may be due to the greater tolerance to desiccation compared to other kelp species (Larkum & Wood 1993). However, it is argued that, for *E. radiata*, this is an area that is still not fully investigated (Wernberg et al. 2019b). Therefore, the reason for its predominant presence in subtidal zones is mostly speculated as reduced competition and grazing, and light inhibition with less UV damage which all needs further investigation (Wernberg et al. 2019b).

Although it is established that *E. radiata* is a subtidal species, the water depth at which it is found varies. They are usually found in a water depth that ranges from the subtidal low tide mark to around 40 m to 50 m depth (Marzinelli et al. 2015). However, in New Zealand *Ecklonia* species have been found in depths of up to 80 m (Nelson et al. 2018).

Ecklonia radiata in shallow water (less than 20 m depth) that is distributed in disjointed patches may be affected by winter storm disturbances (Kennelly 1987b). Also, *E. radiata* patches decrease in size with higher temperatures, herbivory (Vergés et al. 2016) and with increasing population of sea urchins (e.g. *C. rodgersii*; Connell & Irving 2008). However, the distribution of the sea urchin (*C. rodgersii*) is restricted to the east coast of Australia (Connell & Irving 2008) and usually sea urchins cannot be found in *E. radiata* forests located in waters deeper than 30 m (Wernberg et al. 2019b). A significant decrease in temperature (e.g. less than 20°C in early summer), is usually associated with depth greater than 30-40 m, which appears to be a favourable condition for *E. radiata*, observed by an improvement in its density at low altitudes (Marzinelli et al. 2015). *E. radiata* is considered to have a very high capacity to acclimatise to increasing temperature, which can be observed by how it adjusts its photosynthesis, respiration and cellular processes across the temperature gradient over latitudes (Staeher & Wernberg 2009). However, the optimal temperature for photosynthesis of *E. radiata* is between 21.2 to 26.5°C (Wernberg et al. 2016b) and its growth is inversely related to temperatures in such a way that the least growth and productivity occurs in seasons with warmer water (Fairhead & Cheshire 2004a, 2004b).

Water action and wave motion also affects the performance of *E. radiata* (Wernberg et al. 2019b). Wave exposure plays a major hydrodynamic force that can influence *E. radiata* and in comparison, the role of tidal forcing is minor (Wernberg et al. 2019b). At low wave exposure environments, *E. radiata* gets slowly replaced by other canopy forming macroalgae (such as *Sargassum* spp) and turf

forming species (Wernberg & Connell 2008). Overall, *E. radiata* seems to thrive in clear oligotrophic waters with less nutrients and more dissolved oxygen (Wernberg et al. 2010)

Nitrogen enrichment has been related to the loss of *Ecklonia* forests (Gorman & Connell 2009). Water enriched with nitrogen and nitrates along with eutrophication has been linked to an increase in turf and disturbances such as storms have been the cause of sediment input and resuspension into coastal waters (Connell et al. 2008). The presence of both turfing algae and sediment load in the water column have long been reported to inhibit the recruitment of canopy forming macroalgae (Kennelly 1987a). Adult *E. radiata* are known to withstand varying amounts of sediment loads (Wernberg 2005). However, sediment tends to hinder the attachment and cause burial of the younger microscopic stages of *E. radiata*, negatively affecting the gametophyte recruitment process (Connell 2007). Also, *E. radiata* is rare or sparsely distributed in locations of high levels of sedimentation (Connell 2005), which may arrive from human development such as coastal development, effluent discharge and catchment modification (Turner 2004). It is believed that macroalgal communities have a mechanism to cope with normal amounts of sedimentation associated with natural events but populations collapse under additional loads from these human activities (Turner, David J. 2004)

Ecklonia radiata needs a hard substratum to attach for successful growth of the kelp holdfast (Figure 2:4) (Wernberg et al. 2019b). However, *E. radiata* does have the ability to form monospecific forests on a variety of rock types from softer sandstones and limestones to harder granite and basalts (Wernberg, Kendrick & Phillips 2003). Harman and Kendrick (2003) reports that *E. radiata* density is higher on limestone reefs in comparison to granite and high relief reefs. Furthermore, *E. radiata* attaches itself to artificial coastal structures including vertical ones such as concrete seawalls (Marzinelli et al 2018)

Overall, there are multiple factors that contribute to the distribution of *E. radiata*. These factors can primarily be divided into two categories; (1) biological and human factors and (2) physical and geographical factors (Figure 2:5). Biological factors include herbivory from natural predators (e.g. sea urchin) and competition from turfing algae, whereas human disturbances include coastal development and effluent discharge that may lead to sediment load and nutrient enrichment. The other main category is physical and geographical factors, which are categorised together because they contribute to the natural foundation of *E. radiata* settlement and distribution. The summary in the diagram (Figure 2:5) also highlights the complex interconnectivity between factors that was highlighted in the literature. Some factors are more interconnected than others and these factors are grouped together. For instance, temperature and light availability or light penetration decreasing with increasing water depth. However, the key factors identified that affect the distribution of *E. radiata* can be identified as, rock substratum, sediment and nutrient load in water, wave action, water depth and biological competition.

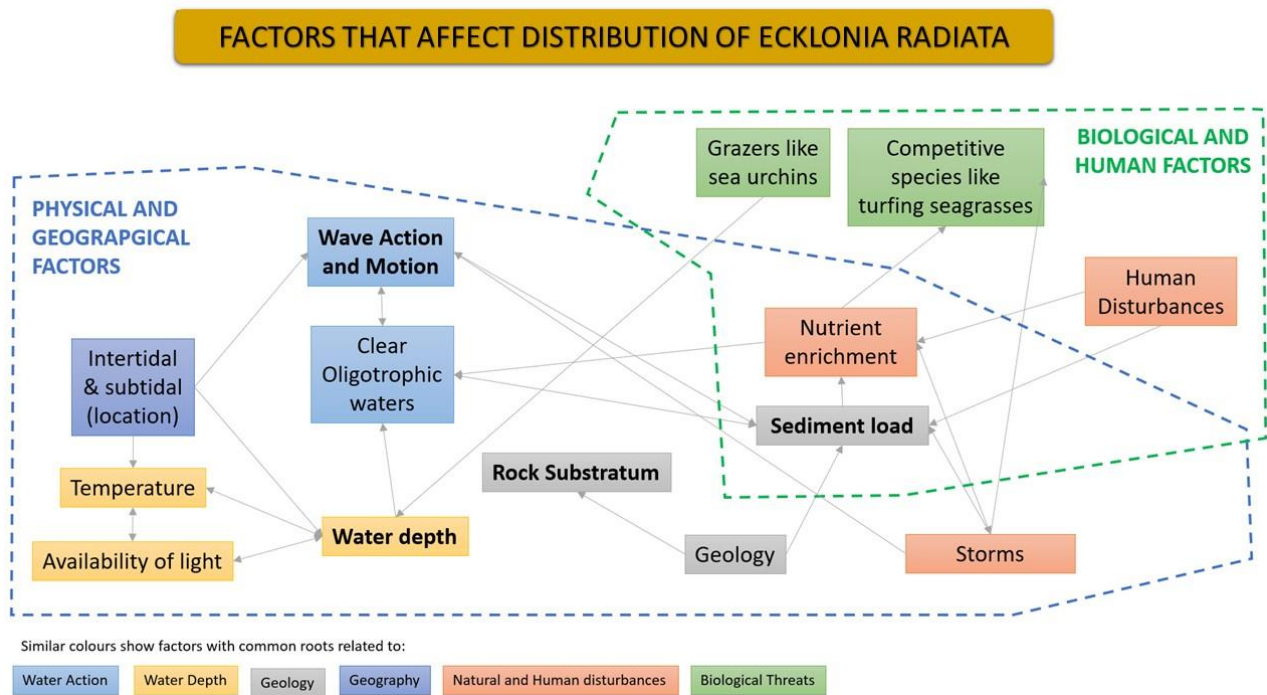


Figure 2:5: A summary of factors that influence the distribution of *Ecklonia* species from literature

2.3.3 Reflectance properties, spectral signature and remote sensing of *Ecklonia radiata*

It is a challenge to detect accurately macroalgae cover from imagery captured from above the water surface (Tait Orchard & Schiel 2021) due to the size variation in macroalgae species, the canopy structure (Tait & Schiel 2018), vertical orientation (Harrer et al. 2013) and the inability to detect understory canopy (Murfitt et al. 2017). Furthermore, remote-sensing is a challenging task because reflectance recorded by remote-sensing is not only from the vegetation but also from the sun glint, water column, and atmospheric disturbance. Hence, the variation of reflectance is not only due to the variation within the object, (i.e., species, biomass) but also due to the variation of atmospheric condition, sun glint, water column condition (Wicaksono & Lazuardi 2018), variation in location, and seasonal variation in the environment (Selvaraj, Case & White 2021)

Optical properties of broad classes of main substrates and biota (e.g. brown macroalgae) are similar across climatic zones including in tropical and temperate environments and across fresh water and sea water environments (Kutser et al. 2020). The reflectance spectra of many “brown” benthic types such as brown macroalgae (e.g. *Sargassum* spp.), brown corals (e.g. *Porites* spp., *Acropora florida*) and soft corals (*Sarcophyton* spp.) are extremely similar (Kutser et al. 2020). This similarity within broad classes makes it almost impossible to use reflectance spectra to differentiate species of brown macroalgae (Kutser et al. 2020).

Most of the studies that attempt to distinguish between species using reflectance spectra are carried out in very shallow water (1-2 m depth), where the number of species present is very low and growing

on brightly distinguished substrate (Kutser et al. 2020). However, when spectral and textual information of species is combined in hyperspectral imagery it is possible to distinguish them as shown by Roelfsema et al. (2014). Furthermore, physics-based classification methods that model environmental characteristics such as atmospheric and water column characteristics combined with the spectral library of various bottom substrates at varying depths plus the use of hyperspectral or multispectral sensors at varying spatial resolution is becoming more common to improve species level separation (Harvey 2009; Selvaraj 2021; Selvaraj, Case & White 2021; Tait, Orchard & Schiel 2021) with varying levels of success. Other studies have investigated spectral reflectance and properties of *Ecklonia* spp. (Fyfe 2003; Garcia et al. 2015; Rand 2006; Selvaraj, Case & White 2021; Tin et al. 2015; Uhl, Oppelt & Bartsch 2013) in various environments and water depths that contribute to further development of the physics-based classification methods that usually use high spectral resolution imagery. Hyperspectral sensors with their narrow band widths have the ability to classify seaweeds at the taxa level, yet they do not yield a high accuracy when attempting to classify seaweeds present in heterogeneous patches and when spatial resolution of the images used are low (Ashraf, Brabyn & Hicks 2012; Casal et al. 2012).

The mean reflectance of *E. radiata* along with other brown macroalgae of similar spectra (Figure 2:6) show low reflectance values which rise towards a small peak at both approximately 590 and 650 nm and then decrease until approximately 670 nm and increase rapidly above that level (Chao Rodríguez et al. 2017; Harvey 2009). This reflectance spectra aligns with the yellow-to-orange colour or the unique golden colour of *Ecklonia radiata* that is visible to the naked eye.

Image removed due to copyright restriction.

Figure 2:6 Reflectance spectra of *E. radiata*, *Sargassum* spp. and *S. doryocarpa* (adapted from Harvey (2009))

Seasonal and location variations affect the spectral reflectance in macroalgae and affect the accuracy of mapping macroalgae when using remote sensing methods (Selvaraj 2021). Spectral reflectance of *E. radiata* varies greatly in summer, and higher rates of photosynthesis is considered the cause of it (Selvaraj 2021). Locational variation in spectral reflectance is not very marked for *E. radiata* (Selvaraj, Case & White 2021), however depth and water turbidity are reported to have an impact on spectral reflectance (Selvaraj 2021).

2.3.4 Future environmental threats on *Ecklonia radiata*

Ecklonia radiata like other kelp species are under threat from climate change and ocean warming. Connell et al. (2008) reported an alarming loss of up to 70 % of canopy forming algae along the Adelaide metropolitan coast since major settlement and urbanisation in the area. Wernberg et al. (2016a) reported a large-scale loss of kelp forest after the 2010 marine heatwave in GSR forcing a transition to turfing seagrass. Kelp forests previously dominated more than 800 km of the west coast and covered an area of 2266 km² of rocky reef. Prior to the heatwave it was reported that kelp forests covered around 70 % of the rocky reefs in the mid-west of Australia (Wernberg et al 2016a). By 2013 there was a 43 % loss of kelp forests along the western coast. In 2015, there were s no signs of *E. radiata* recovering from the heatwave. Wernberg et al. (2016a) indicated that *E. radiata* may have reached a tipping point due to the increasing temperature.

3 METHODS

This section describes the methods used to collect data and analyse the data that was collected in this study. The flow chart shown in Figure 3:1 below is a summary of the methods used for data collection.

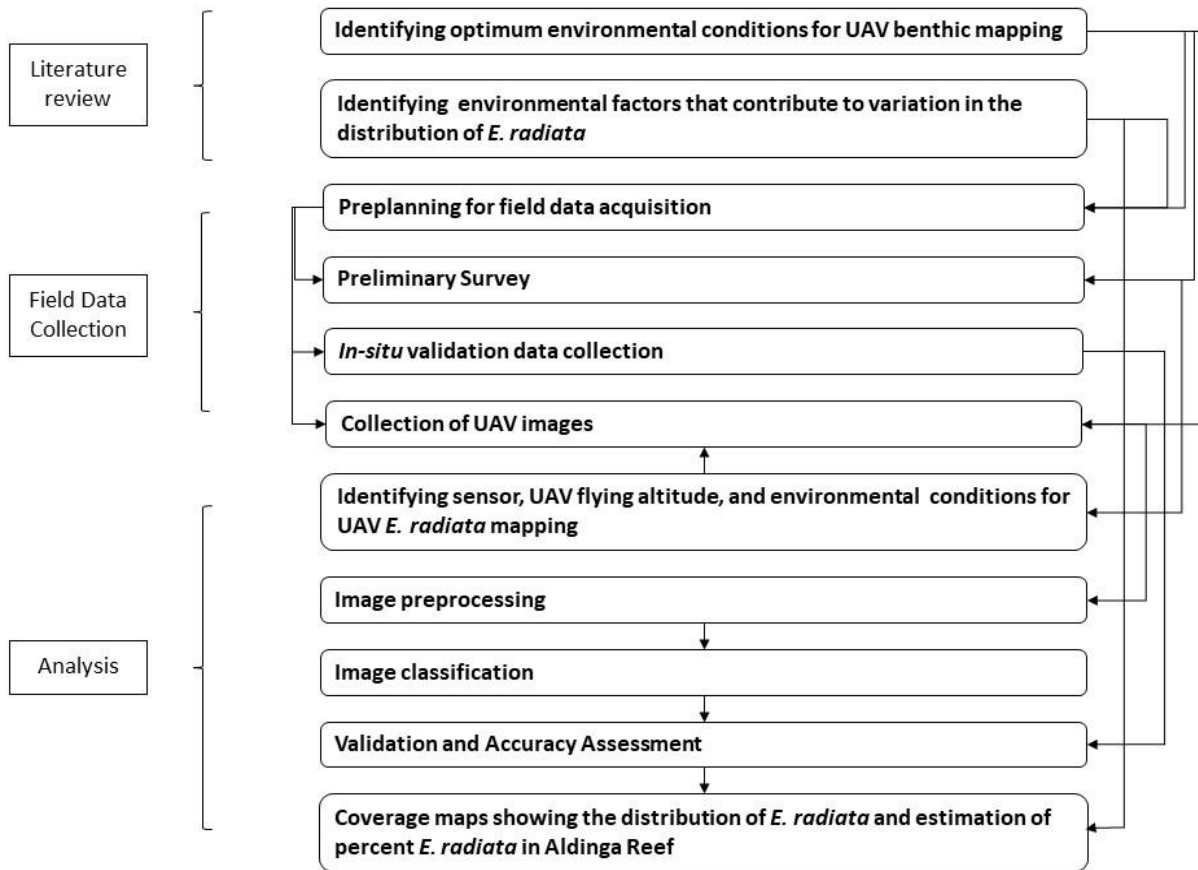


Figure 3:1: An overview of the methods used to collect data and analysis of images and mapping.

3.1 Planning for Field Data Collection

Field data collection required planning the field work logistics and acquiring the required permissions and permits. UAV flying training was received from Flinders University’s Department of Geospatial Information Science (GIS). This was followed by the acquisition of Department and Civil Aviation Safety Authority (CASA) RPA operator accreditation. As Aldinga Aquatic Reserve is a protected area, a Marine Park Permit to undertake scientific research was acquired from the Department for Environment and Water (DEW). Risk Assessments for field outings were prepared and submitted to Flinders University. Fieldwork was always carried out with a field partner and CASA regulations were followed when collecting data in the field. Dive Validation was carried out by a Flinders University Scientific Dive Team. All related documents are attached in Appendix 8.1.

3.2 Preliminary Survey

3.2.1 Identifying sensor and flying altitude of UAV

Traditional habitat mapping using quadrat and transect sampling can be time consuming (Underwood 2000), covers only a small spatial area, and replicating the same quadrats and transects are usually challenging (Murfitt et al. 2017). It is challenging to monitor exposed rocky reef environments due to factors such as ecological variability and heterogeneity in species over space and time, and because of structural, spatial variation of the reef platform (Tait, Orchard & Schiel 2021). Due to its periodical exposure to swell and tides the accessibility for *in-situ* data collection is challenging (Tait, Orchard & Schiel 2021). The use of remote sensing platforms, such as satellite and manned aircrafts, do have the ability to capture data over a large spatial extent (Murfitt et al. 2017). However, a very high spatial resolution (i.e. cm accuracy) is needed to capture the structure of *E. radiata* and its fronds, thus satellite imagery could not be used in this project. Furthermore, satellite imagery has the disadvantage of revisits with undesirable tidal and meteorological conditions, which can obstruct the view underwater (Tait, Orchard & Schiel 2021). These issues can be resolved using an UAV, because it can capture very high spatial resolution imagery and can be deployed when environmental and meteorological conditions are suitable for the study (Murfitt et al. 2017; Tait, Orchard & Schiel 2021). Furthermore, UAVs have the potential to bring together traditional *in-situ* data collection methods and remote sensing methods (Anderson & Gaston 2013) to develop a data collection method as proposed in this study.

Preliminary data was collected on 28th April 2021 during lowest tide at Aldinga Reef using a DJI Mavic 2 Enterprise UAV (SZ DJI Technology Co., Ltd, China) and a Parrot Sequoia multispectral sensor. Images were captured in lines across the intertidal and subtidal zone of the reef at varying altitudes. RGB and thermal images were taken from a Mavic Enterprise UAV camera. The Parrot Sequoia camera have five separate sensors. Four of them that captured images in separate spectral bands using individual optics per band. These four sensors captured separate monochrome images for each spectral band of green (530-570 nm), red (640-680 nm), red edge (730-740 nm) and near infrared (770-810 nm) (Pix4D 2021). The fifth sensor captured RGB images. The images captured by both Mavic Enterprise sensors and Parrot Sequoia sensors were studied to identify the image types and sensor that could identify *E. radiata* over shallow water at Aldinga Reef.

Table 3:1: A comparison of Mavic 2 Pro, Mavic 2 Enterprise, and Parrot Sequoia multispectral sensor (DJI 2018b, 2021a, 2021b; Pix4D 2018, 2021)

	Mavic 2 Pro (RGB)	Mavic 2 Enterprise (RGB)	Mavic 2 Enterprise (Thermal ¹)	Parrot Sequoia (RGB)	Parrot Sequoia (Multispectral)
Sensor width (mm)	13.2	6.17		3.6	3.6
FOV, HFOV, VFOV	77, 40, 60	84, 40, 60	HFOV:57		
Focal Length (mm)	28	24		4.88	3.98
Image width (pixels)	5472	4000	480	4608	960
Image height (pixels)	3648	3000	640	3456	1280
	¹ Thermal band width: 8-14µm				

Additional images were captured on 2nd June 2021 using a DJI Mavic 2 Pro (SZ DJI Technology Co., Ltd, China) for two purposes. The first purpose was to compare the RGB image quality of three available sensors. Table 3:1 shows a comparison of some key attributes of interest of the UAVs and their sensors explored for comparison. The second purpose was to find the best flying altitude to capture images to identify *E. radiata* with structural details, that could be used in a supervised object-oriented classification algorithm. For this purpose, images were captured at varying altitudes. Selvaraj (2021) reported that *E. radiata* can be discriminated from *Undaria pinnatifida* using five-band multispectral UAV imagery at its best accuracy at a flying altitude of 30 m. Riniatsih et al. (2021) suggested a UAV flying altitude of 20 m above water to capture RGB and IR images to capture the details of the thin leaves of seagrasses. Thus, in my study, flying altitudes were varied to observe the altitude at which the structural detail of *E. radiata* fronds can be identified with UAV imagery.

All RGB images captured from the Mavic 2 Pro, Mavic Enterprise and Parrot Sequoia were inspected to find the best sensor form the three that can capture the structure of *E. radiata* at the highest altitude. The Mavic 2 Pro and Mavic 2 Enterprise had similar sensor properties. The Mavic 2 Pro was selected because of its slightly larger image dimensions in pixels and larger sensor width (Table 3:1), and visual inspection of images showed better quality images from it.

Furthermore, flights were flown to identify rough estimates of the distance out from the edge of the intertidal zone, which was unable to detect *E. radiata* visually to define the outer edge boundary of Zone S in the study area (Table 3:3).

3.2.2 Identifying appropriate environmental conditions for UAV detection of *Ecklonia radiata*

The quality of images captured over shallow waters in Aldinga Reef was analysed by collecting UAV imagery across varying environmental conditions. Environmental data along with imagery is considered useful for a better understanding of data captured from imagery (Hedley et al. 2016).

Cloud cover is considered to reduce sun glint, yet cloud cover also means reduction in the intensity of light and the amount of light that reaches the subsurface (Joyce et al. 2019). Capturing images in cloud cover during midday is reported an alternative (Kay, Hedley & Lavender 2009). Low turbidity in water, low windspeed, low tide and shallow water are also favourable conditions in aerial imagery (Joyce et al. 2019; Mount 2005).

For this study, images were captured in late autumn and winter. Environmental factors that were recorded include wind speed, temperature, humidity, cloud cover and sun illumination, tides, sun angle and azimuth and atmospheric pressure. Weather conditions were measured using the SkyWatch® portable weather station. Tide data for Aldinga was collected from WillyWeather®. Sun altitude and azimuth were collected from Geoscience Australia (2021). Data were collected between 11th June 2021 to 26th August 2020 (Table 3:2).

Table 3:2: Environmental factors recorded and observed to analyse the suitable conditions for collecting UAV images

Date	Wind (km/hr)	Temp (°C)	Humidity (%RH)	Atmospheric Pressure (hPa)	Cloud cover and sun illumination (observations)	Measured Tide (m) and Observations	Water Turbidity Observations	Sun altitude and azimuth angles at low tide (degrees)	
11/06/2021	17	12	-	-	Completely cloudy	0.7	Calm clear waters	Altitude: 25° 32' 29 Azimuth: 29° 35' 27	
15/06/2021	19	15.9	73.1	1005.6	Completely cloudy	0.8 (observed tide is higher: around 2m)	Very turbid and cloudy water	Altitude: 31° 21' 19 Azimuth: 03° 41' 56	
20/06/2021	7.6	15.7	67.7	1025.2	Mostly Sunny	High tide 1.7 to 1.8m	Wave action over zone I; higher turbidity	Altitude: 22° 52' 20 Azimuth: 34° 16' 55	
28/06/2021	10-24	14.9 - 16.1	- 72.9 - 67	1027 - 1025.7	-	Very sunny with very few clouds	0.9, 0.8, and 1m	Very calm waters	Altitude: 25° 36' 32, 28° 13' 60, 30° 01' 34 Azimuth: 28° 57' 23 , 21° 48' 55, 14° 44' 55
29/06/2021	17 -30	15.5	60.3	1022	Very sunny with no clouds at all	0.9, 0.8 & 1 m	Calm waters	Altitude: 29° 14' 57, 31° 13' 15, 31° 32' 02 Azimuth: 18° 23' 34, 06° 55' 08, 359° 07' 33	
26/08/2021					Very sunny with very few clouds	0.6, 0.9, 2	Calm water	Altitude: 41° 17' 06, 41° 10' 32, 18° 52' 11 Azimuth: 23° 54' 30, 335° 33' 04, 298° 12' 15	

3.3 Collection of UAV images

A main consideration when identifying the sensor for a shallow water remote sensing project is that the pixel size of the image should be smaller than the target measured under water as pixel mixing

is a primary limiting factor of benthic remote sensing (Hedley et al. 2012). The fronds of *E. radiata* were observed to have an average width of around 3-5 cm in the intertidal zone. Images were captured using the Mavic 2 Pro at 20 m flying altitude with a ground sampling distance (GSD) of 0.5 cm/pixel, to ensure a good coverage of pixels on each frond. An UAV flying altitude of 20 m was identified for this research to allow for the capture of more detail of *E. radiata* (Riniatsih et al. 2021) over some areas of the subtidal zones. Different methods of UAV image collection were employed depending on the need and type of data required for the research. All images were collected on 28th, 29th June and 26th August 2021. However, all images were captured at a flying altitude of 20m.

Images were acquired for the following purposes.

1. To estimate the cover of *Ecklonia radiata* across the study area
2. To validate the classification model across the deep subtidal zone
3. To validate the classification model over very shallow subtidal and intertidal zones

3.3.1 Image Collection to Estimate Cover of *E. radiata*

To estimate the cover of *E. radiata* over the study area, UAV Flight missions were planned using a DJI Ground Station Pro (DJI GS Pro) Application (DJI 2018a). Multiple Way Points Mission was used to collect stratified random individual images over the study area. The stratified random points for the centre of the images were generated by creating a buffered zone of intertidal and subtidal areas (Zone I and S as described in Table 3:3 and shown in Figure 3:2 and generating random points over the zones using ArcGIS Pro (Esri 2021a) Create Random Points Tool.

Table 3:3: Description of zone created to capture individual images of the study area

Zone Name	Description of the environment	Zone Creation Method
Zone I	The edge of intertidal zone of Aldinga Reef that includes rock pools and transition (abruptly at north and west and more gently at south) to a shallow subtidal zone.	Zone I was created by drawing a line on the edge of the intertidal zone and buffering 50 m on both sides both of the line. Random stratified points of image centres were generated from ArcGIS Pro software.
Zone S	This area includes shallow and deep subtidal zones of Aldinga Reef	This area was created by drawing a line on the edge of the intertidal zone and creating a 300 m buffer seawards from the line and cropping the Zone I from it. Random stratified points of image centres were generated from ArcGIS Pro software



Figure 3:2 The shallow subtidal and intertidal zone (Zone I) and deeper subtidal zone (Zone S) where individual images were captured to estimate percent cover of *E. radiata* at Aldinga Reef

As the dataset contained hundreds of images and was spanning a wide area that went beyond the line of vision of the UAV pilot it was divided into sections to be flown for safety and practical purposes (screen captures of flight plans in Appendix 8.2)

The optimum conditions to view objects under water is when the sun altitude is less than 35° according to Mount (2005) and between 35° and 50° and with the sensor oriented towards or away from the sun as explained by Mustard, Staid and Fripp (2001). Furthermore, ideal orientation of images for habitat mapping are nadir images because oblique images distort progressively towards the horizon affecting its geometry along with it (Green et al. 2000). However, when taking the above explained conditions into consideration, the ideal time to capture nadir images gets limited to a very narrow time frame in the morning (Joyce et al. 2019). This is when the sun angle is high enough to illuminate the water but not so high to create sun glint. Also, consideration is needed about the sea breeze later in the day when it increases and creates larger wave crests, which reflect sun glint (Mount 2005). Sticking to a narrow time frame may also mean missing the time window of low tide,

which can also limit the data collection to a very specific and narrow period of time (Joyce et al. 2019). To increase the narrow time frame for UAV, images can be captured with a flight heading that aligns with the sun azimuth and with a slight camera tilt (Joyce et al. 2019) that aligns with the sun altitude angle.

For this study, the flight plans were made with the UAV heading aligned to the sun azimuth and its gimble pitch angle aligned with the sun altitude to minimise sun glint (Joyce et al. 2019; Mount 2005; Mustard, Staid and Fripp 2001). Oblique images with a tilt that was the same as the sun altitude angle at the time of UAV deployment was captured. The data for sun altitude and sun azimuth data were collected from Geoscience Australia (2021) in the field and the pre-planned flight plans were adjusted before deploying the UAV. UAV data was collected when the tide was at the lowest point during the day (usually between 9am and 3pm) and when the underlying water was properly illuminated by the sun. Winter early morning low tides and late afternoon low tides were avoided. Furthermore, as winter brings stormy weather, limiting data collection to an ideal low wind speed less than 18 km/hr (Mount 2005) was not considered practical because it would further diminish the available time for data collection. Therefore, data was collected when windspeed was below 30 km/hr which is the maximum windspeed for flying a DJI Mavic 2 Pro (DJI 2019).

3.3.2 Image Collection to Validate Classification Model

Zone I: Image collection to validate classification model over rockpools in the intertidal zone (Zone I)

Rock pools at the sites in Zone I (i.e., the intertidal and shallow subtidal zone) were used to validate the classification model. The rock pools can be captured in a single image taken at 20 m altitude; images were captured by free-flying the UAV to the area of interest. Nadir images were captured over the rock pools because it was observed that, even at mid-day, in very shallow waters, bright sun glint was not an issue with the camera positioned away from the sun. Water in rock pools and the intertidal zone remained quite calm during low tide and did not contribute to the bright sun glint in the same way as incoming waves in subtidal areas.

Rockpools were selected to ensure pool size, depth, and *E. radiata* cover varied in the rockpools so that good representative sample rockpools could be used for validation of the classification model (Figure 3:3).

Table 3:4: Description of rockpools used as validation areas in the shallow subtidal and intertidal zones (Zone I).

Validation Rockpool	Description of the environment	Area Creation Method
West Deep (WD) Rockpool	This is a large rock pool with high <i>E. radiata</i> cover from visual assessment, with a depth that is similar to shallow areas of subtidal zones.	Rock pools of interest were identified and transect lines for validation were entered and mapped with a 0.25m buffer zone. Transect lines were laid out in field and images were captured and used to position on the map. UAV individual images were taken over the rockpools for classification.
West Shallow (WS) Rockpool	This is a large but shallow rockpool with sparse <i>Ecklonia</i> cover on visual assessment.	
North Shallow (NS) Rockpool	This is a small and shallow rockpool with sparse <i>Ecklonia</i> cover on visual assessment	



Figure 3:3: Location of rockpools used for validation at Aldinga Reef in 2020.

Zone S: Image collection to validate classification model over subtidal zone (Zone S)

To estimate *E. radiata* cover over validation areas in subtidal zones 3D Map Area Missions from the Ground Station Pro (GSP) App. were used to make flight plans over the areas of interest. Validation areas were selected from subtidal zones in the north, west, and south of the study area. These areas were selected to ensure that variable environmental characteristics observed in the subtidal zones of the study area were represented. Table 3:5 Description of areas for validation in the subtidal zone (Zone S) describes the variation in the environment and Figure 3:4 shows the location of the validation sites.

Images were captured with 50% image overlap to generate a mosaic over areas allocated for validation. A 50% overlap was used because it was observed, from images captured at the preliminary stage, that individual images over the subtidal zone had sun glint on the image which sometimes covered almost half of the image depending upon various variables such as wave action, wind speed, tide, and camera angle (Joyce et al. 2019; Mount 2005; Mustard, Staid and Frip 2001). Therefore, a 50% forward and sideways overlap was used to minimise the impact of sun glint from the mosaic created.

Table 3:5 Description of areas for validation in the subtidal zone (Zone S)

Validation Area	Description of the environment	Area Identification Method
North*	Subtidal zone with large patches of sediment and no evidence of <i>E. radiata</i> present on visual assessment	Area of interest was identified. ArcGIS Pro software was used to define transects lines for dive validation. Three lines of 30 m in length separated by approximately 30 m were created in each area of interest. These lines were placed in parallel, and horizontal to the coastline, progressing away from it. The area that contained all three validation transect lines were defined as a polygon and 3D Map Area Missions were flown over these areas.
West	Subtidal zone with <i>E. radiata</i> in very shallow water and deeper water environments. <i>E. radiata</i> growing over rock pinnacles or rock outcrops elevated <i>E. radiata</i> to very shallow water environments during low tide. <i>E. radiata</i> also found on the reef base on the rocky platform. These large patches of <i>E. radiata</i> were visible on visual assessment.	
South	Shallow subtidal zone with large patches of <i>E. radiata</i> and large patches of other types of seagrasses that were visible in visual assessments.	

***Note:** Due to the placement of one transect line over the border between Zone I and S (during validation) the North Area intersect slightly with the intertidal zone. However, because a larger part of the area falls to Zone S and most of the transect line in question is on the border (NT1 in Figure 3:9), it is considered a validation area for Zone S

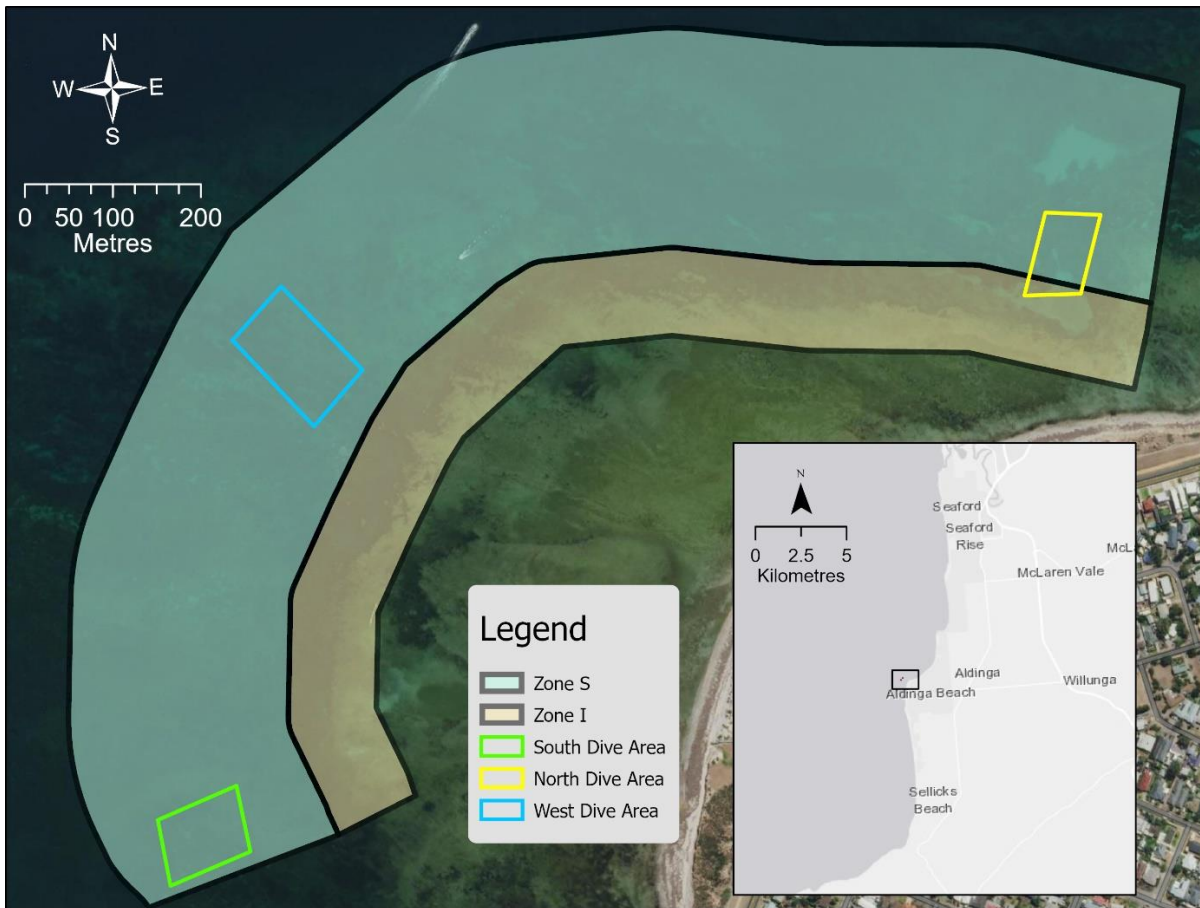


Figure 3:4: Dive Validation Areas in North, South and West of the study area at Aldinga Reef

UAV images over each area (North, South and West) were captured from separate flights. The heading and gimble angle of the UAV was aligned to the sun's azimuth and sun's altitude immediately before the flight. Images in these datasets were oblique with a tilt that aligned with the sun altitude angle.

3.4 Pre-processing of UAV Images

Images were not subjected to complex pre-processing. The two stages of pre-processing involved in this study included georeferencing of images and mosaicking of overlapping and non-overlapping images. Water attenuation models to alter the reflectance of images was not used due to the lack of detailed bathymetry data. The available bathymetry data was too coarse to be used for this research.

3.4.1 Georeferencing and Mosaicking

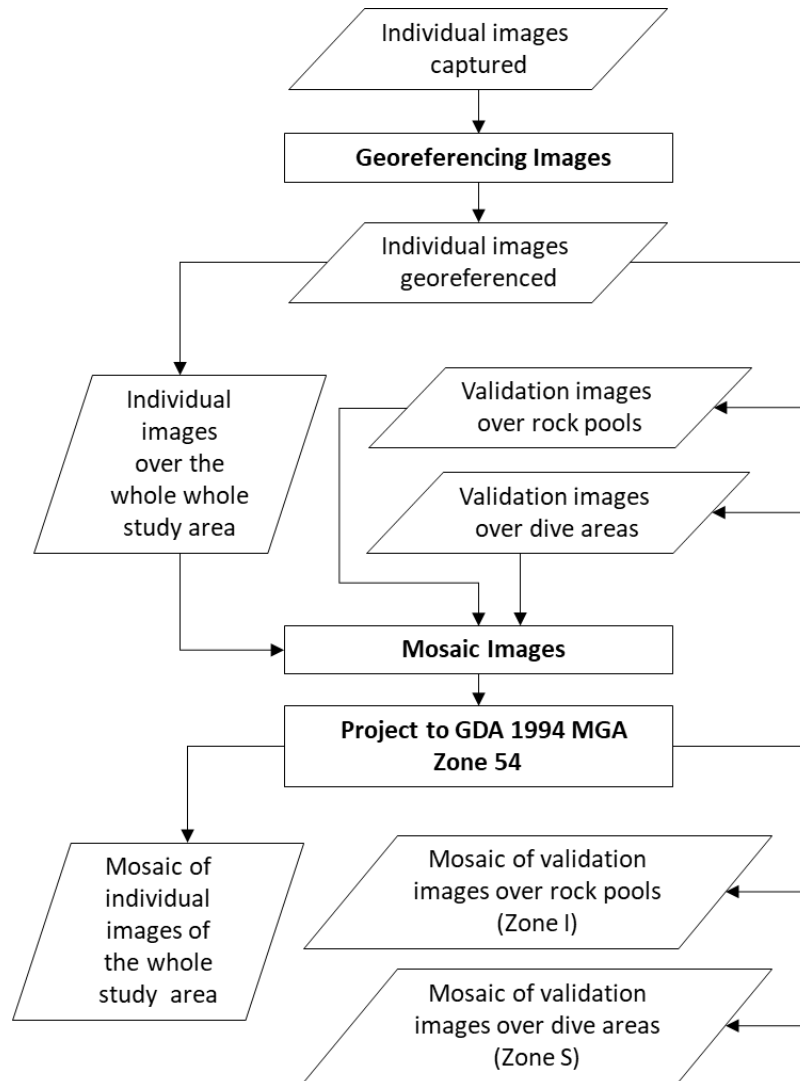


Figure 3:5: An overview of georeferencing and mosaicking of all input data

Images captured by remote sensing methods need geometric processing and georeferencing to position the image in the correct location and to carry out spatial measurements on it as part of image analysis (Joyce et al. 2019). UAV images have IMU and GNSS units that can tag the GPS location of the centre of the image to an average of ± 5 metres depending on the UAV, number of satellites the UAV is locked onto, environmental and atmospheric conditions, and oblique imagery with camera centres located beyond GPS location of the drone (Joyce et al. 2019). Therefore, it is important to properly georeference images with these possible error considerations. When cm to mm accuracy in location of imagery is required, ground control points (GCP) are measured using real time kinematic (RTK) differential GPS (Joyce et al. 2019). RTK equipment is expensive and can only be used in very shallow water areas such as an intertidal zone (Bryson et al. 2016). Furthermore, when capturing images that cover only the water surface it is challenging to collect enough GCPs

accurately (Selvaraj 2021). However, due to higher thanprecedented tides and the challenges of deploying targets GPCs and RTK measurements were not used in this study.

Geometrically corrected, nadir images that have global positioning data and ideally ground control points can be easily georeferenced and stitched together to make a mosaic or orthomosaic (Joyce et al. 2019). In this study, the data collection method deviated from this ideal by capturing oblique imagery. The weather conditions and higher tides observed in the location during winter made laying out ground control target points a challenge. Furthermore, the conservation status of the study area limited the use of permanent or semi-permanent targets that can withstand tidal movement and weather.

All images captured were manually georeferenced using ArcGIS Pro software (Esri 2021) and used a Projective Transformation Model, which is useful for oblique imagery (Esri 2021). Images were georeferenced against high resolution aerial imagery from Aerometrics Metromap (2021) with pixel sizes of 5cm. Dynamic Range Adjustment (DRA) and Histogram Equalizer were used to enhance the aerial image to facilitate the accurate georeferencing of UAV images.

Once all images were georeferenced, they were used to create mosaics. Prior to mosaicking individual images were arranged in the desirable order to eliminate sun glint and mosaiced as shown in Figure 3:6. Mosaics were generated using ArcGIS Pro (Esri 2021a) using the New Raster Tool. Each mosaic output was created in a tiff format with a cell size of 0.007 m and resampled using a cubic convolution method (Figure 3:6). Cubic convolution method was used because it this method used the greatest number of neighbouring cell (16) values to determine the new cell values when resampling compared to other resampling methods available in ArcGIS Pro (Esri 2021c). Furthermore, it was observed that this method retained the finer variation in the pixel values closest to the original image. The mosaics that were created were then projected to GDA 1994 MGA Zone 54 using both ArcGIS Pro software (Esri 2021a) and ERDAS imagine because reprojection of a large mosaic was time consuming in ArcGIS Pro (Esri 2021a).

The individual image mosaic was created to estimate *E. radiata* over the study area, which was very large, and therefore was compressed using the lossless compression Leperl-Ziv-Welch (LZW) algorithm (Esri 2021b). A detailed flowchart of mosaicking and projection of individual mosaics created for validation zones and for the whole study area is shown in Figure 3:6

Mosaics created area listed below.

1. Mosaics were created for the validation areas North, South and West and then these mosaics were mosaiced again to combine them. This combined all validation areas in Zone S.
2. A single mosaic was generated that combined images of rock pools that covered validation lines in Zone I.

- A very large single mosaic was created that combined all 150 individual images that covered Zone I and Zone S. This mosaic was used to estimate the cover of *E. radiata* at Aldinga Reef.

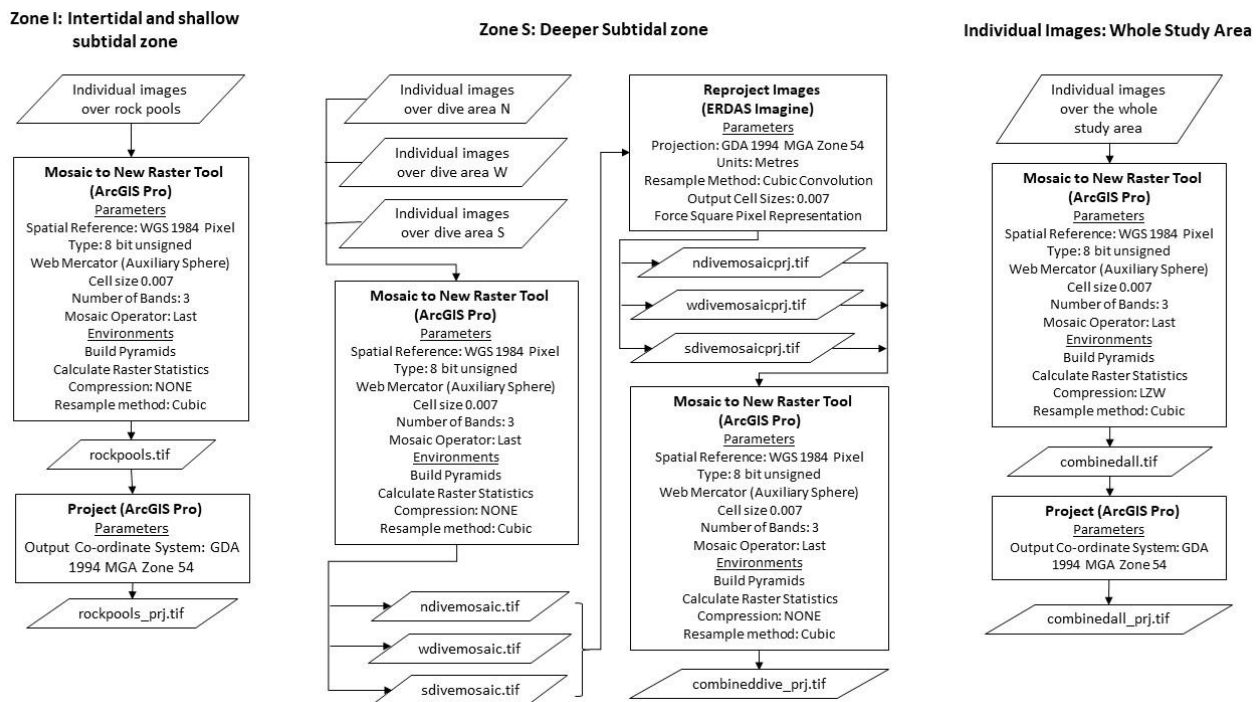


Figure 3:6: Detailed flowchart of mosaicking and reprojection process to create mosaics for validation and mosaic of individual images that covered the whole study area

3.5 Image Classification

An object based supervised (Hedley et al. 2016) nonparametric classifier such as SVM (Lu & Weng 2007) was identified as the most suitable classification method to classify *E. radiata* because it has the ability to use both spectral and spatial components to train and classify images. A spectral profile of main benthic classes seen in Aldinga reef is shown in Figure 3:7. Spectral detail can be used to separate main broad classes. However due to the spectral similarity of *E. radiata* in deeper water with the rest of seagrasses, an object-oriented classification method such as SVM was used. *Ecklonia* in deeper water spectrally very similar to other seagrasses as shown in Figure 3:7. However, the fronds of *E. radiata* even in deeper water helps to visually separate it from other seagrasses. SVM classifier was selected because with proper training SVM can learn to identify (Roelfsema et al. 2018a) *E. radiata* in deeper water with its structural differences despite its spectral similarity with other aquatic vegetation in deeper water.

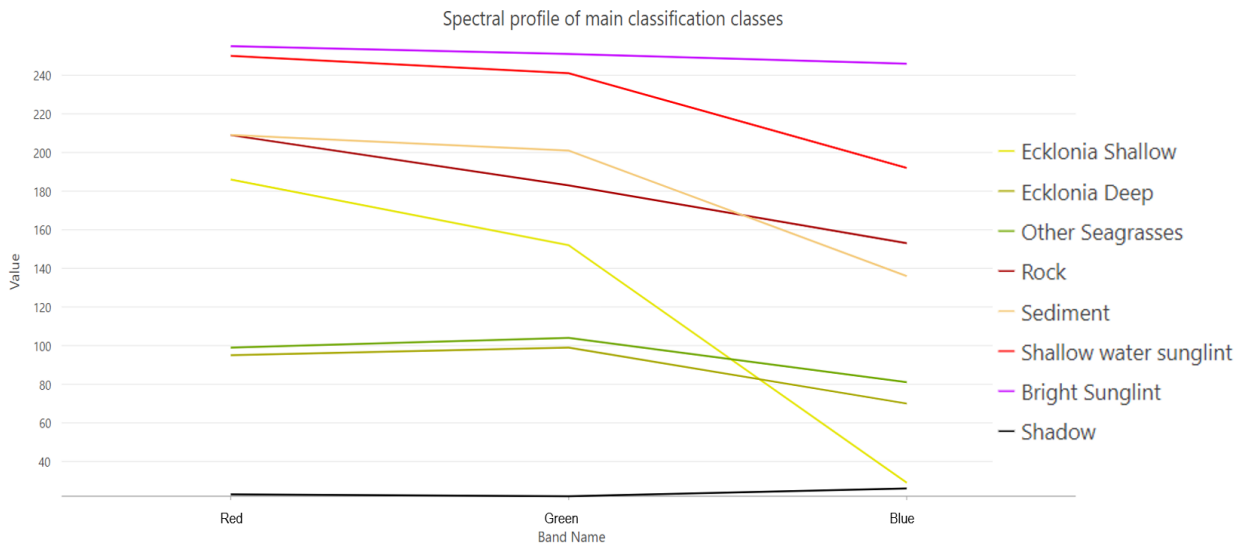


Figure 3:7: Spectral profile of broad benthic classes found in Aldinga Reef

The mosaics created for image classification (shown in Figure 3:6) were classified in ArcGIS Pro software (Esri 2021a) using Image Classification Wizard as shown in Figure 3:8. Supervised Object-Oriented Classification Method was used along with Support Vector Machine (SVM) Algorithm

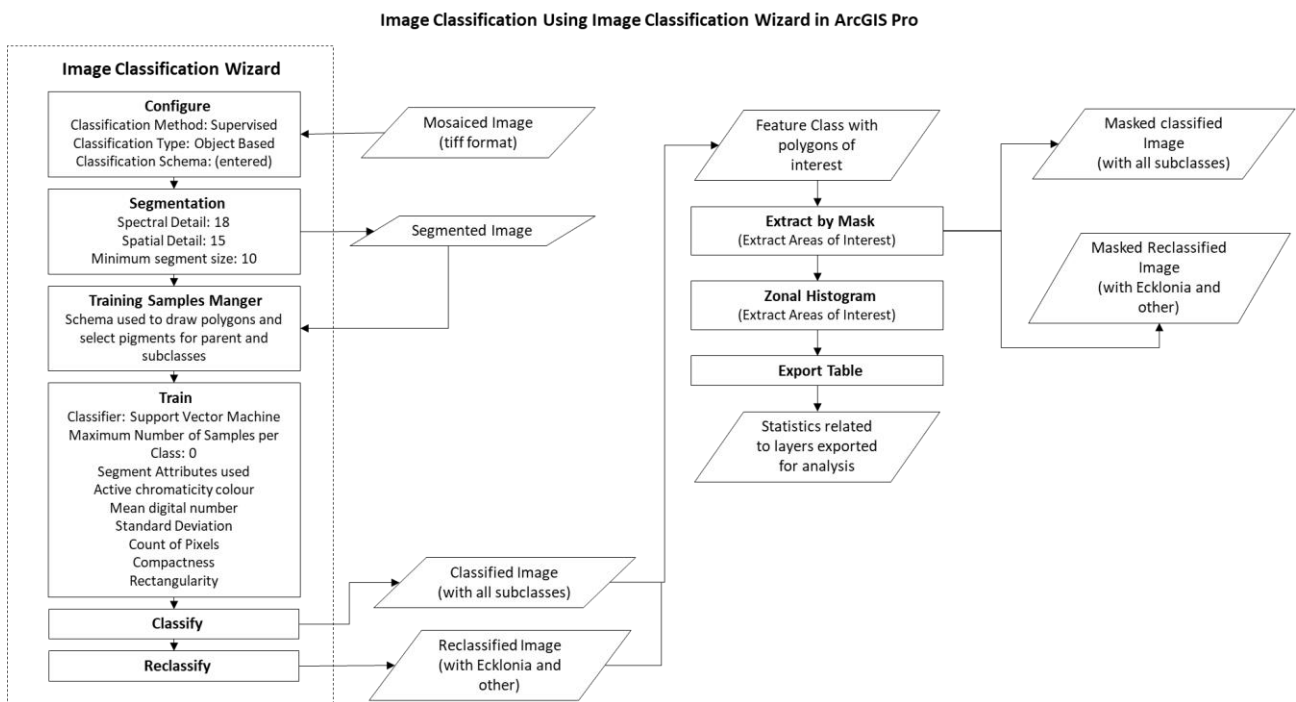


Figure 3:8: Flowchart showing the image classification process using the Image Classification Wizard in ArcGIS Pro

The mosaics generated were brought into the classification wizard as an input. The mosaics were segmented with a spectral detail value of 18, spatial detail value of 15 and a minimum segment size

of 10. A higher spectral detail value was used because major classes, including shallow *E. radiata*, has the potential of separability using spectra (see Figure 3.7). However, when multiple samples of the spectral signature of different classes were taken, an overlap between some classes, such as *E. radiata* and sun glint in shallow water was found. Furthermore, *E. radiata* in deeper water was spectrally similar to other macroalgae. However, all these classes had distinct morphological shapes, which can be used to classify them. Therefore, a higher spatial detail value of 15 was set. A minimum segment size of 10 pixels was used because an individual *E. radiata* frond that was visible usually had more pixels covering its area, but segments of shallow water sun glint were usually smaller than this value. Therefore, this segment size value helped remove shallow water sun glint. The mosaiced image was then trained with training samples. Training samples were used to train each major class into subclasses based on depth, object type, sun glint and shadow. The schema for different mosaics changed depending on the broad classes visible from the mosaic. All the parent and subclasses used in schemas are shown in Table 3:6.

Table 3:6: Classes of categories included in the schema for mosaiced image samples

Parent Classes	Subclasses
Ecklonia_shallow	
Ecklonia_deep	
Other	Other aquatic vegetation_deep Otheraquatic vegetation_shallow Sunlint_deep Sunlint_shallow Shadow Sediment_deep Sediment_shallow Rock

Training was carried out to include most training samples from *E. radiata* (at least 40% of the training was included from *E. radiata*). Other classes were also trained to have a training sample number that was representative to the percentage found in the images. Training was carried out using polygons to train *E. radiata* and other classes that had spectral variability within the object. However, segment picker was used in some instances, especially when the training shadow and bright sun glint were present, and they were segmented out neatly because of lack of variation in the spectra of these classes.

Once the classification and reclassification of the images were complete, they were masked using the Extract by Mask Tool to remove only the area of interest (i.e., transect borders in validation data or zone boundaries) and the Zonal Histogram Tool was used to calculate statistics on these areas of interest for the classified and reclassified images.

3.6 Data Validation

Data validation was carried out at validation sites in both intertidal and subtidal zones highlighted in Figure 3:3 and Figure 3:4

3.6.1 Validation in subtidal zone

Data Validation in subtidal zones were carried out by a Flinders University's scientific dive team on 8th September 2021. The validation was carried out by laying out a 30 m transect line with a measuring tape and a diver recorded a video along the transect line using a GoPro Hero 7 camera while holding it 0.5 m above the line. A dive watch was used to estimate the average depth of each dive transect. Each transect line was separated by 30 m. Three transect lines were recorded for each dive area in North, South and East (Figure 3:9 shows the transect lines validated by the dive team). The dive team used research vessel 'Tethys' equipped with a Garmin GPSMAP 720 to navigate to the dive transect line. As the accuracy of Garmin GPS usually ranges between 5-10 m (GARMIN 2021) the transect lines that were used by the divers were positioned on the map and buffered by 10 m to account for the accuracy of the Garmin GPSMAP 720. The imagery acquired over the dive transect was mosaiced, classified and cropped to the 10 m buffer zone.

The GoPro videos were analysed to identify the percentage cover of *E. radiata* along each transect and collectively for each dive area (North, South and West). A tape measure was used to calculate the total distance along the transect that intersected with *E. radiata*. This distance was used to calculate the percent cover of *E. radiata* found on each transect and collectively in each dive area.

An additional validation analysis was carried out on the three validation transects in the West site. This was due to the difference in the environment in the area compared to the other two dive validation sites (see Table 3:5). *Ecklonia radiata* growing on top of the rock pinnacles were measured separately and a percentage of *E. radiata* on these rock pinnacles were recorded. This percentage was calculated only in the West dive transects because such rock pinnacles were not found in the validation transects at North and South dive areas.

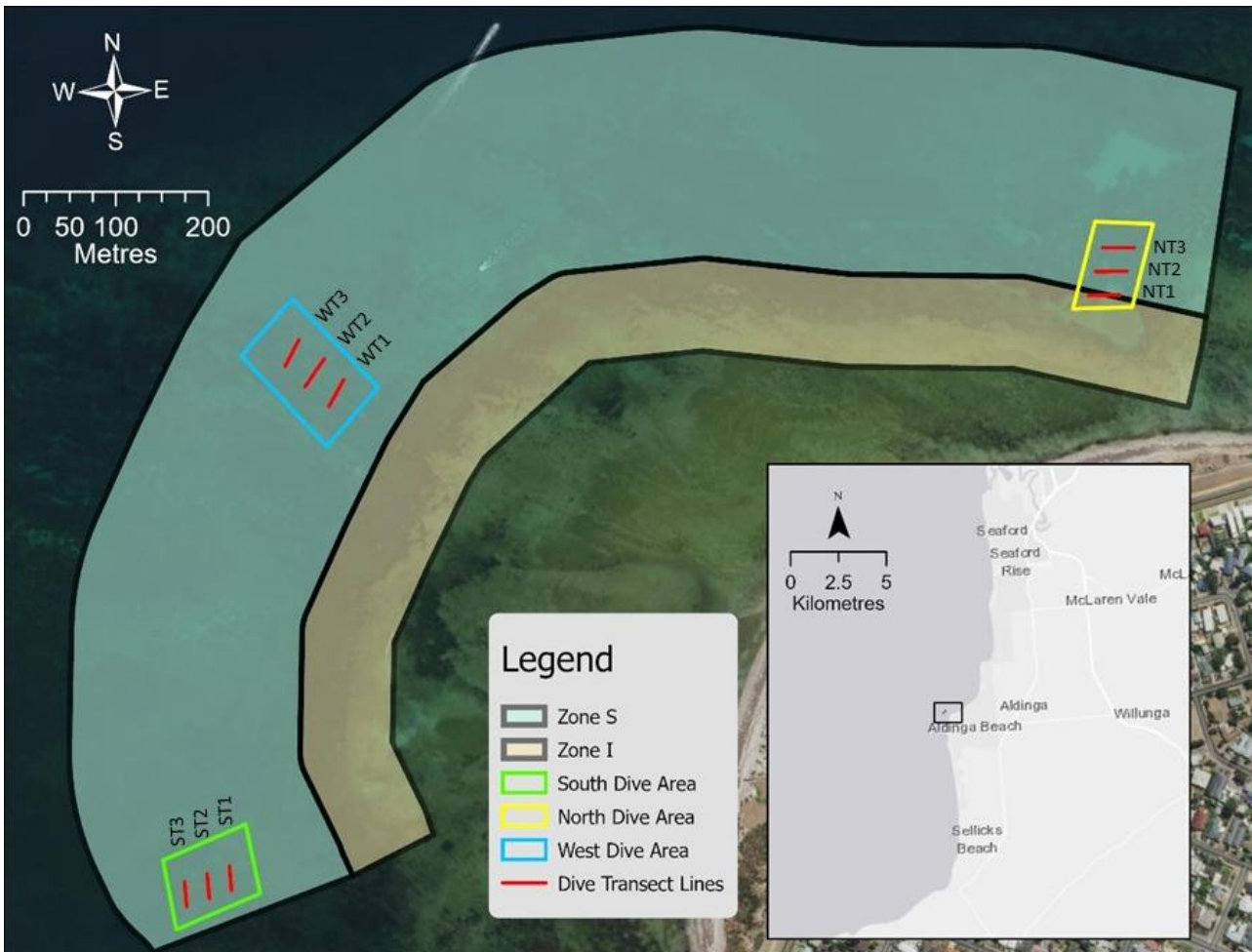


Figure 3:9: Showing dive transect lines (in red) in each validation area in South, West and North subtidal areas

3.6.2 Validation in rockpools

Data validations over rock pools were carried out on 26th August 2021. Validation was carried out by laying out line transects that were 1 m apart and covered the entire extent of each rockpool. Each transect line had knots that marked every 0.5 m distance. A one metre ruler was used to measure the depth of water and the presence and absence of *E. radiata* along each transect. Images were taken of the location of the beginning and end of each transect line to mark its position in the rock pool. The point measurements of the presence or absence of *E. radiata* and the depth at each point along the transect lines was used to calculate the percentage of *E. radiata* and the average depth of each transect line in each rockpool.

The transect lines and validation points were plotted over the rockpools using ArcGIS Pro (Esri 2021a). The transect line was buffered by 0.25 m to give way to the slight movement of the line in the water. Since the transect line was fastened at both ends with weights, this movement was

considered very slight, hence a buffer of 0.25 m was used. The images captured at both ends of each transect line were used to position the transect using ArcGIS Pro (Esri 2021a). The validation data that were collected for each transect were used to calculate the average depth and the percentage of *E. radiata* for transects in each rockpool.

3.7 Accuracy Assessment

An accuracy assessment is an important part of detecting the accuracy of the remote sensing method to detect different parts of a habitat (Green et al. 2000). In UAV, remote sensing accuracy assessment is especially important if the target studied is partially or fully submerged in water or when taking quantitative measurements of variables (Joyce et al. 2019). However, accuracy assessment of habitat maps is usually subjective to the need of its application and the lack of specific guidelines increases this subjectivity (Green et al. 2000). For instance, if the habitat map is used to create an inventory of a type of macroalgae for management purposes a thematic accuracy of 60 % is also considered useful. However, for an assessment of the impact of a development project on the health and distribution of macroalgae in a region, a higher accuracy (usually closer to 90 %) may be demanded (Green et al. 2000). Therefore, the level of accuracy required is related to the context and the need to which it is being catered for.

Accuracy is also defined and measured using different methods (Green et al. 2000). For instance, the accuracy of a geometrically corrected image may be determined by calculating the root mean squared. However, an error in the geometric correction applied in the image can result correctly classified pixels of an image, that aligns with *in-situ* classification, placed in the wrong location (Green et al. 2000). Georeferencing was the only geometric correction applied to the images and the positioning of dive validation transect lines had an estimated error of 10m and the rockpool validation transect lines had an estimated error of 0.25m. Due to these uncertainties a more robust accuracy assessment method such as the use of a confusion matrix (Green et al. 2000) was not used. Alternatively, a much simpler thematic accuracy assessment was carried out. A thematic accuracy assessment does not take into consideration the spatial accuracy of the dataset (Green et al. 2000). Instead, it assesses the extent to which the class identified from the classification represents the class observed *in-situ* on site (Green et al. 2000). In this study, accuracy of the dataset was assessed by comparing the percentage of *E. radiata* from validation with the percentage generated from the image classification. This was then converted to a percent accuracy

4 RESULTS

4.1 Preliminary Survey

The preliminary survey generated results on the capacity of different sensors and spectral bands in these sensors to detect *E. radiata*. It also helped to decide from the available sensors which one to use for data collection in this research. Furthermore, the survey was also used to identify the UAV ideal flying height, to detect *E. radiata*, and identify the environmental conditions that favoured *E. radiata* detection using UAV images.

4.1.1 Ability of Different Types of Sensors and Bandwidths to Detect *E. radiata*

The images collected from the Parrot Sequoia sensor showed that near infrared was unable to penetrate water. Thermal images from the Mavic Enterprise were also unable to detect *E. radiata*. However, RGB images from both the Parrot Sequoia and Mavic Enterprise cameras were able to capture *E. radiata* at low tide in both intertidal and subtidal zones at lower altitudes.

Table 4:1 Summary of the ability of different sensor and bands to capture *E. radiata*

Sensor type	Bands	Ability to Detect <i>E. radiata</i>
Parrot Sequoia	RGB	yes
	NIR	no
DJI Mavic 2 Enterprise	RGB	yes
	Thermal	no
DJI Mavic 2 Pro	RGB	yes

4.1.2 UAV Flying Altitude to Detect *E. radiata*

RGB images were able to capture the unique golden colour of *E. radiata*, growing on large rock pinnacles in deeper subtidal zones and in the shallow intertidal zones, in very bright sunlight at very low tide (e.g. 0.3 m tide level). More distinction between *E. radiata* and the rest of macroalgae begin to emerge in images captured at an altitude of 60 m and below. However, at this altitude the shape of fronds, even in shallow water, gets pixelated, as in many instances less than 20 pixels fell on an *E. radiata* frond at this altitude. The shape of *E. radiata* fronds begin to show their morphological form and structure in detail with images taken at an altitude below 30m. Table 4:2 summaries the changes in spectral and spatial detail with image altitude from UAV when captured in bright sunlight.

Table 4:2: A summary of how spectral and spatial detail changes with changes in image altitude.

Flying Altitude (m)	Spectral Detail	Spatial Detail
100	Faintly visible details in very shallow areas	No details
70	Shallow <i>E. radiata</i> distinguishable by colour in shallow areas	Faint details visible in very shallow <i>E. radiata</i>
60	Good spectral contrast between <i>E. radiata</i> and other aquatic vegetation begin to emerge in shallow waters	Details visible but blurred in shallow water
50	Good*	Details visible but blurred in shallow water
40	Good*	Details of <i>E. radiata</i> fronds begins to emerge more clearly in very shallow water
30	Very good*	Good details visible in shallow waters
20	Excellent*	Excellent details in intertidal and good details in subtidal areas
10	Excellent*	Excellent details of <i>E. radiata</i> in subtidal waters and can identify details of <i>E. radiata</i> fronds even in the shadow of some rock pools

**E. radiata* in deeper waters are spectrally different to *E. radiata* in shallow water. Its unique golden tint is visible in shallow water. In deeper water, even at lower altitudes images with more spatial detail are visible, spectrally *E. radiata* was closer to other macroalgae.

4.1.3 Environmental Conditions for UAV Image Collection

The environmental factors measured and observed are shown Table 3:2 and Table 4:3. It was observed that low tides helped to detect *E. radiata* by lowering the amount of water above the benthos. When tides were lowest, the tips of *E. radiata* were exposed for a brief amount of time in some parts of Aldinga reef (especially in the South) in the shallow subtidal zone and the intertidal zones. However, *E. radiata* can be easily detected from UAV images in a low tide between 0.8 to 1 m tidal height at Aldinga Reef.

Low tide alone, without bright sunlight, did not capture the unique golden yellow spectra of *E. radiata* in shallow water. In images captured with low tide and high cloud cover, *E. radiata* in shallow water was easily identified. However, *E. radiata* in deeper waters were not very easy to visually identify. In these conditions, *E. radiata* found in shallow water was spectrally similar to *E. radiata* in deeper waters. In contrast, on days of bright sun illumination with little or no cloud cover, *E. radiata* was visible in the intertidal zone on rock platforms and in shallow subtidal areas and on rock pinnacles over deep subtidal zones. *E. radiata* in shallow water in bright sunlight was easily identified by their golden colour and visibly distinguishable from *E. radiata* in deeper water. Wave action increased turbidity in areas with soft-sediments, thus *E. radiata* could only be captured successfully in the shallow subtidal zone and intertidal zone over areas with rocky substrates (rather than soft-sediments). High tide resulted in waves breaking over the intertidal platform and the form of those waves for UAV imagery was similar to bright sun glint obscuring what was underneath. *Ecklonia radiata* could be detected at low tide when wind speeds were lower than 30 km/hr. However, at high tide, and in strong windspeeds, *E. radiata* detection would be difficult due to increased water turbidity and wave action

Sun azimuth and angle played a role in the amount of sun light that penetrated the water and how UAV images could be captured to avoid sun glint. In the preliminary survey, the higher the sun altitude, the better illumination of water was observed. Bright sun glint was minimised by aligning UAV tilt according to the sun altitude angle and by setting the flight heading to align with the sun azimuth. However, increased wave action still contributed to sun glint problems. Also, low sun altitudes created shadow especially in rockpools and near rock pinnacles

Some environmental factors such as tides and illumination had a direct effect on the ability to detect *E. radiata*. Whereas other factors such as atmospheric pressure, temperature and humidity had indirect effects. Tides for example were affected by both low atmospheric conditions and wind direction. Low atmospheric pressure in combination with shoreward wind direction resulted in water levels that were much higher than the forecasted tide. Humidity and temperature had no direct effect on the ability to detect *E. radiata* over water. However, higher temperatures were observed along with high atmospheric pressure and bright sun illumination and high humidity was observed along with high cloud cover and lower atmospheric pressures. Overall, the most important environmental conditions for favourable detection of *E. radiata* were low tide levels and bright illumination from the sun. Table 4:3 summaries environmental conditions that favoured *E. radiata* detection in the preliminary surveys.

Table 4:3: Summarises the environmental conditions that are favourable for *E. radiata* detection

Environmental factors	Favourable conditions for UAV data collection
Tide	Lowest possible tides (ideally tides below 0.9m)
Illumination	Bright sun light with minimum or no cloud cover
Wave action and water turbidity	Calm, low turbidity water
Wind	Wind speeds below 30 km/hr (ideally below 18 km/hr)
Atmospheric Pressure	Higher atmospheric pressure (linked to tides and lowering of water column)
Sun Altitude	Higher sun altitudes illuminate water better and minimize shadow in rockpools and around larger rocks.

4.2 Image Classification Outputs for Validation sites

4.2.1 Classification of images over zone S

The benthic map outputs generated in the deeper subtidal zone (Zone S) over validation transect areas using the SVM classifier are shown in Figure 4:1 to Figure 4:6. These maps show the results from the classification outputs for all classes and the *E. radiata* class alone. In maps and tables labels are: *E. radiata* in shallow water “Ecklonia_shallow”; *E. radiata* in deep water, “Ecklonia_deep” and; the combined class of all *E. radiata*, both in shallow and deep water, “Ecklonia_combined”.

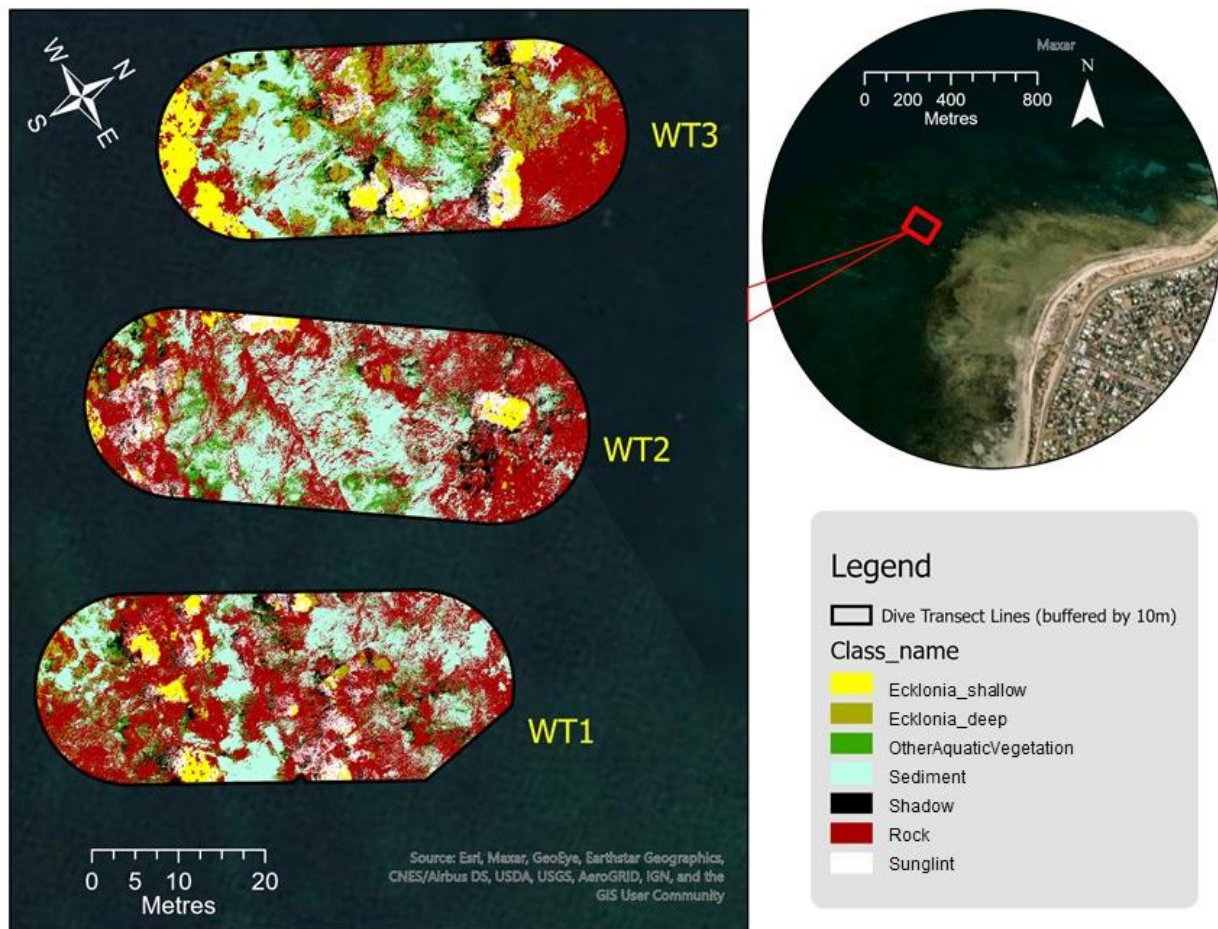


Figure 4:1: Classified validation transects in the West of the study area showing all classes within the area covered by the 10m buffered transect lines (WT1, WT2, WT3) of 30m in length each.

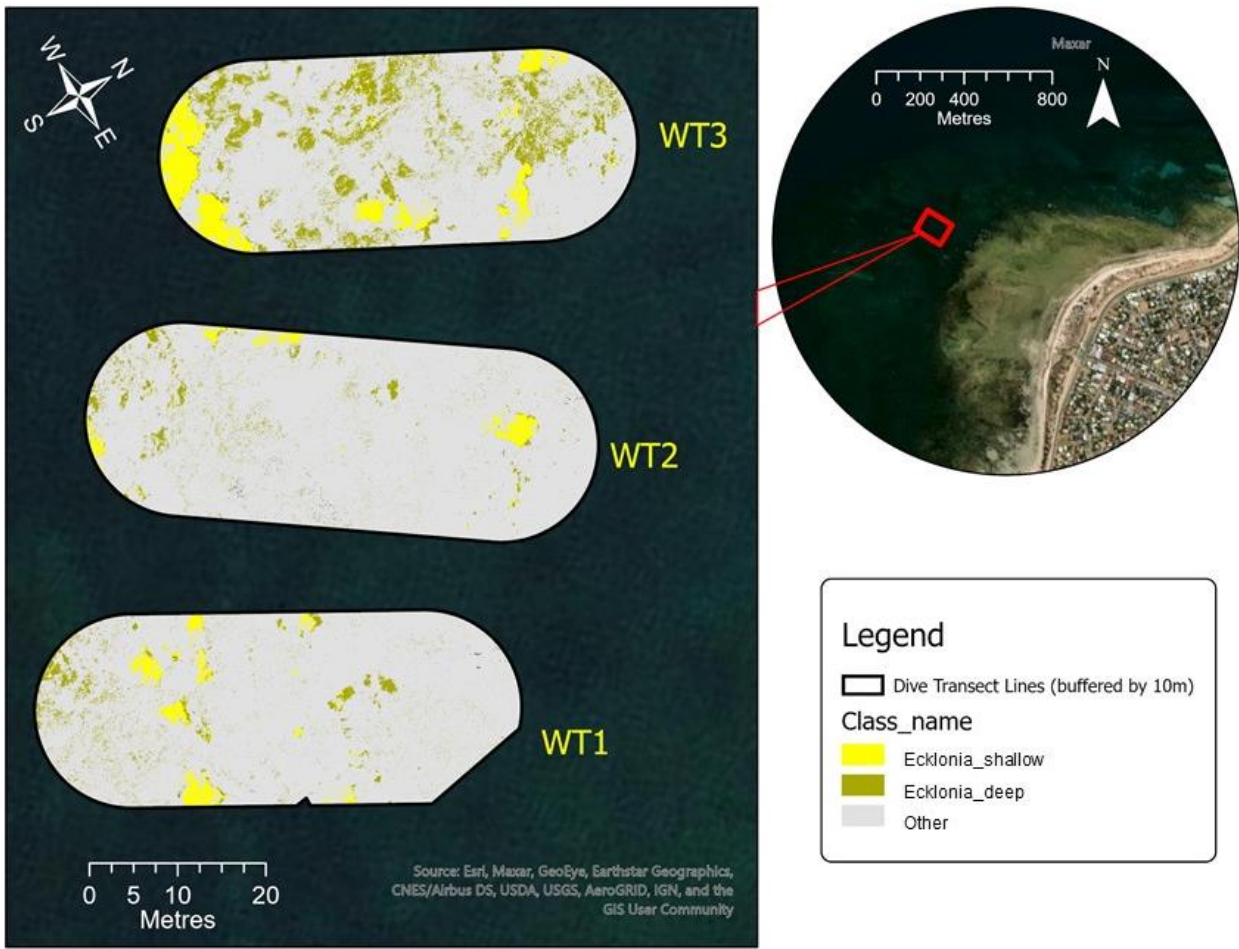


Figure 4:2: Classified validation transects in the West of the study area highlighting *E. radiata* within the area covered by the 10m buffered transect lines (WT1, WT2, WT3) of 30m in length each.

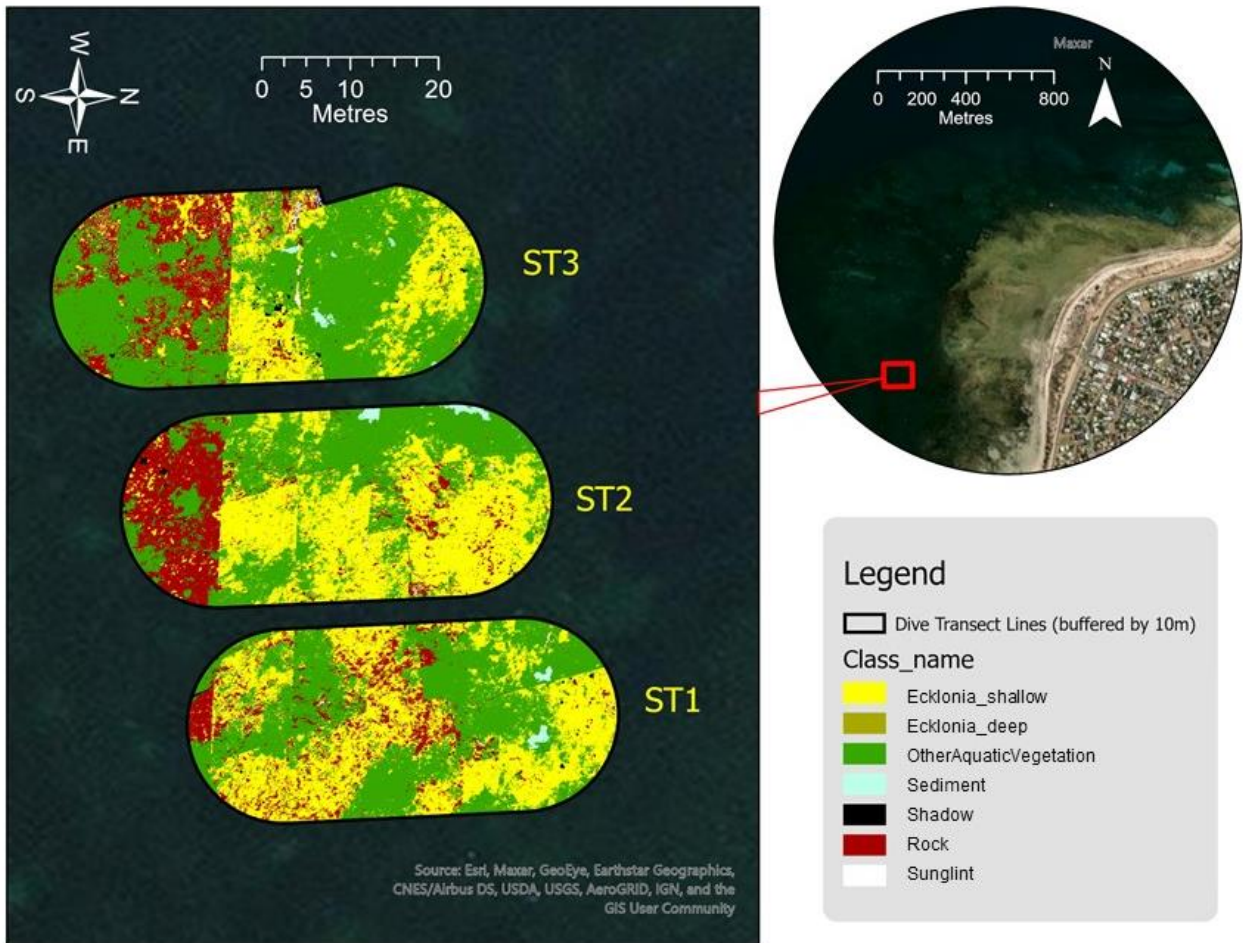


Figure 4:3: Classified validation transects in the South of the study area showing all classes within the area covered by the 10m buffered transect lines (ST1, ST2, ST3) of 30m in length each.

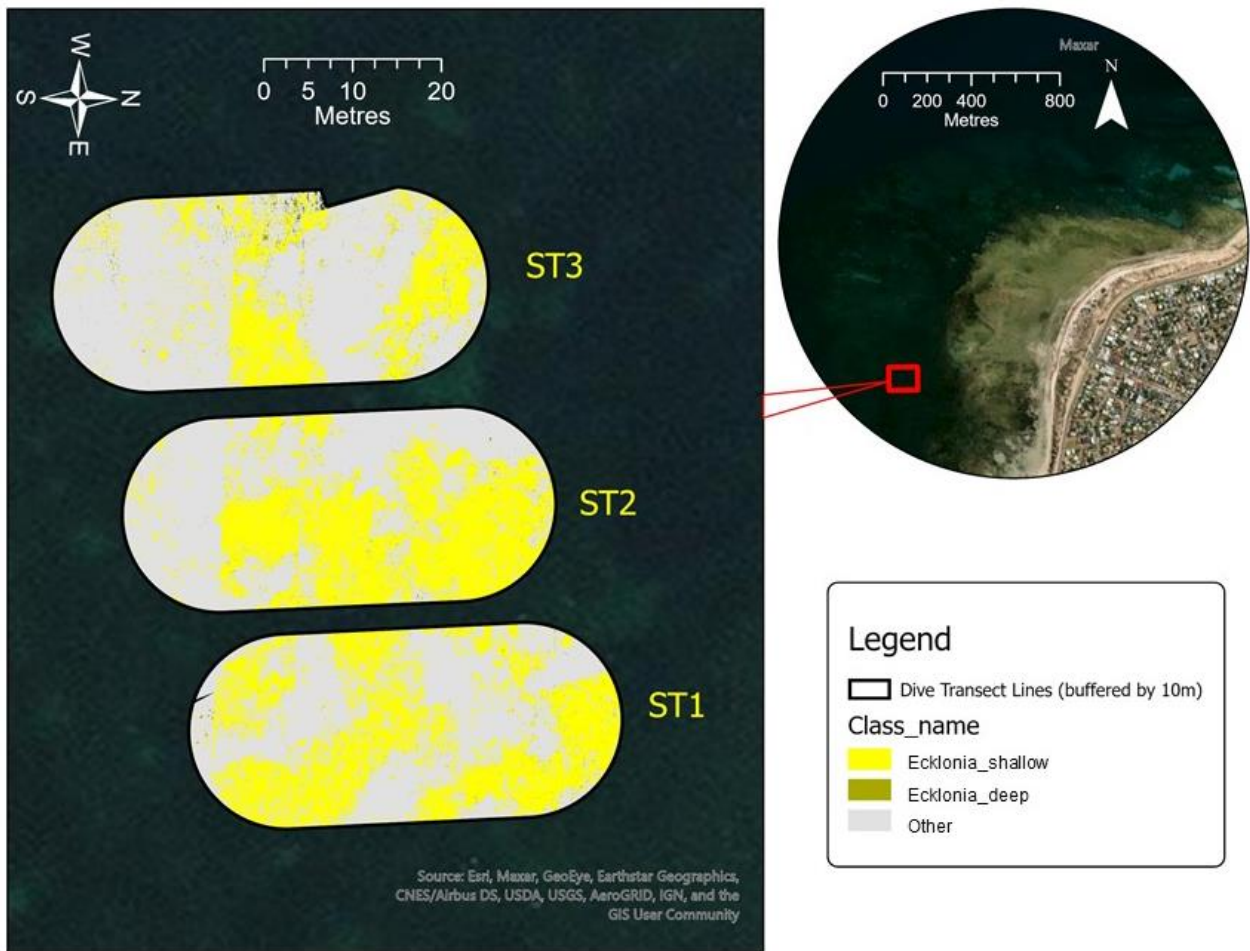


Figure 4:4: Classified validation transects in the South of the study area highlighting *E. radiata* within the area covered by the 10m buffered transect lines (ST1, ST2, ST3) of 30m in length each.

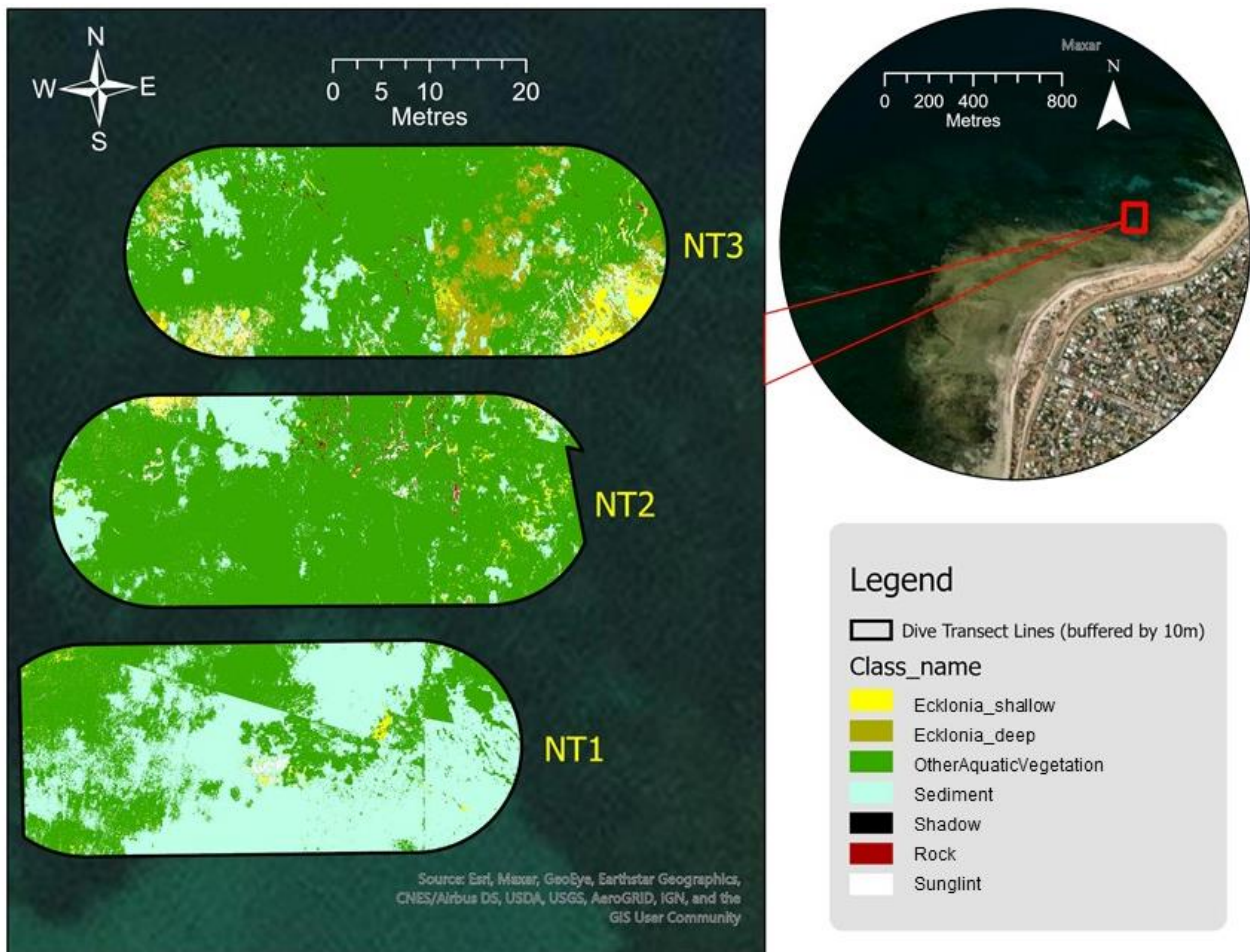


Figure 4:5: Classified validation transects in the North of the study area showing all classes within the area covered by the 10m buffered transect lines (NT1, NT2, NT3) of 30m in length each.

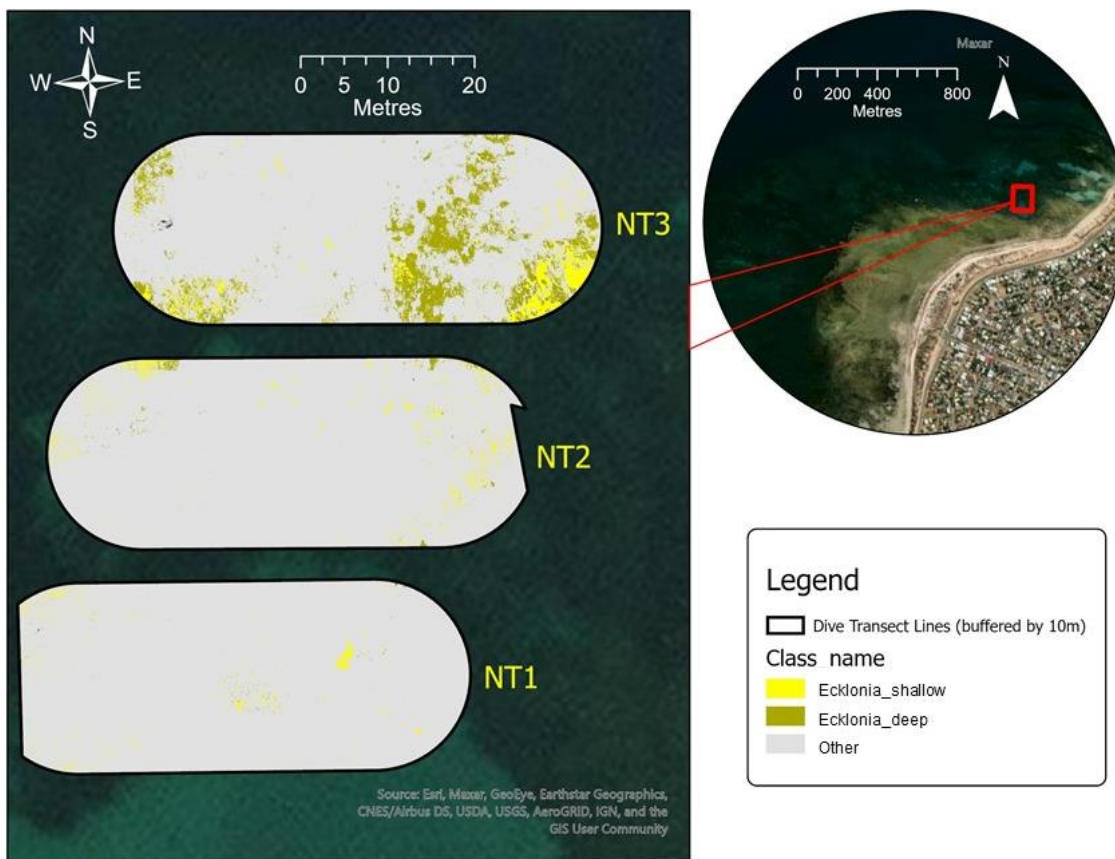


Figure 4:6: Classified validation transects in the North of the study area highlighting *E. radiata* within the area covered by the 10m buffered transect lines (NT1, NT2, NT3) of 30m in length each.

Table 4:4: Percentage of *E. radiata* from SVM classifier for individual transects lines of each validation area (north, south, west) in the Deep Subtidal Zone (Zone S) and percentage of *E. radiata* for each validation area separately.

	West Dive Transects			North Dive Transects			South Dive Transects		
	WT1	WT2	WT3	NT1	NT2	NT3	ST1	ST2	ST3
<u>SVM Classifier</u>									
% Ecklonia_Shallow	3	2	8.1	1	1.9	3.9	42.2	42.7	23.9
% Ecklonia_Deep	4.4	3.5	14	0	0.4	10.9	0.4	0.3	0.7
% Ecklonia_Combined	7.4	5.4	22.2	1.1	2.3	14.8	42.5	43.1	24.6
Combined transects									
	West	North	South						
<u>SVM Classifier</u>									
% Ecklonia_Shallow	4.3	2.3	36.3						
% Ecklonia_Deep	7.2	3.9	0.5						
% Ecklonia_Combined	11.5	6.2	36.8						

The percentage of *E. radiata* classified in Zone S, varied across different validation areas. The overall percentage of *E. radiata* detected in the West, South and North dive areas from the SVM method was 11.5% in the West, 36.8% in the South and 6.2% in the North (Table 4:4). When comparing these values with the overall validation values for the same area (W:37.5%, S:21% and N:0%) the lowest level of accuracy in classification was in the West area. The accuracy of in the individual transect lines (WT1, WT2 and WT3) in the West for shallow *E. radiata* or *E. radiata* on the rock pinnacles, was very high (97.4%, 87.5% and 98.2% respectively) along with the overall accuracy at 97%. In comparison, accuracy for the individual transects without the distinction of shallow and deep *E. radiata* were less for individual transects (83.4%, 72.8% and 66.6%) as well as the average for all three transects at 74%.

4.2.2 Classification of Images over zone I

Figure 4:7 to Figure 4:9 shows classified benthic habitat maps over transect lines in rockpools. The maps show broad classes used for classification and simplified maps that also show *E. radiata* across the transects surveyed

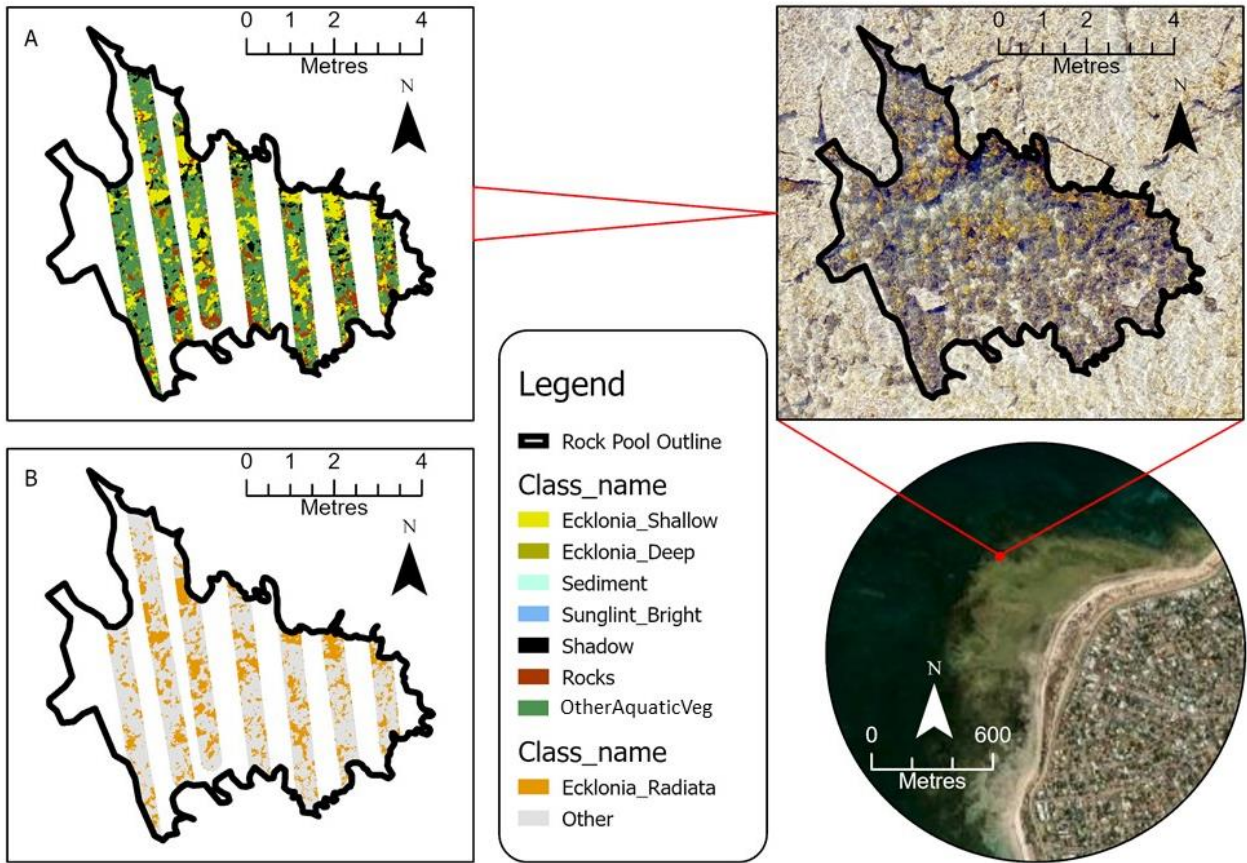


Figure 4:7: Classified validation transects in the North Shallow (NS) Rockpool

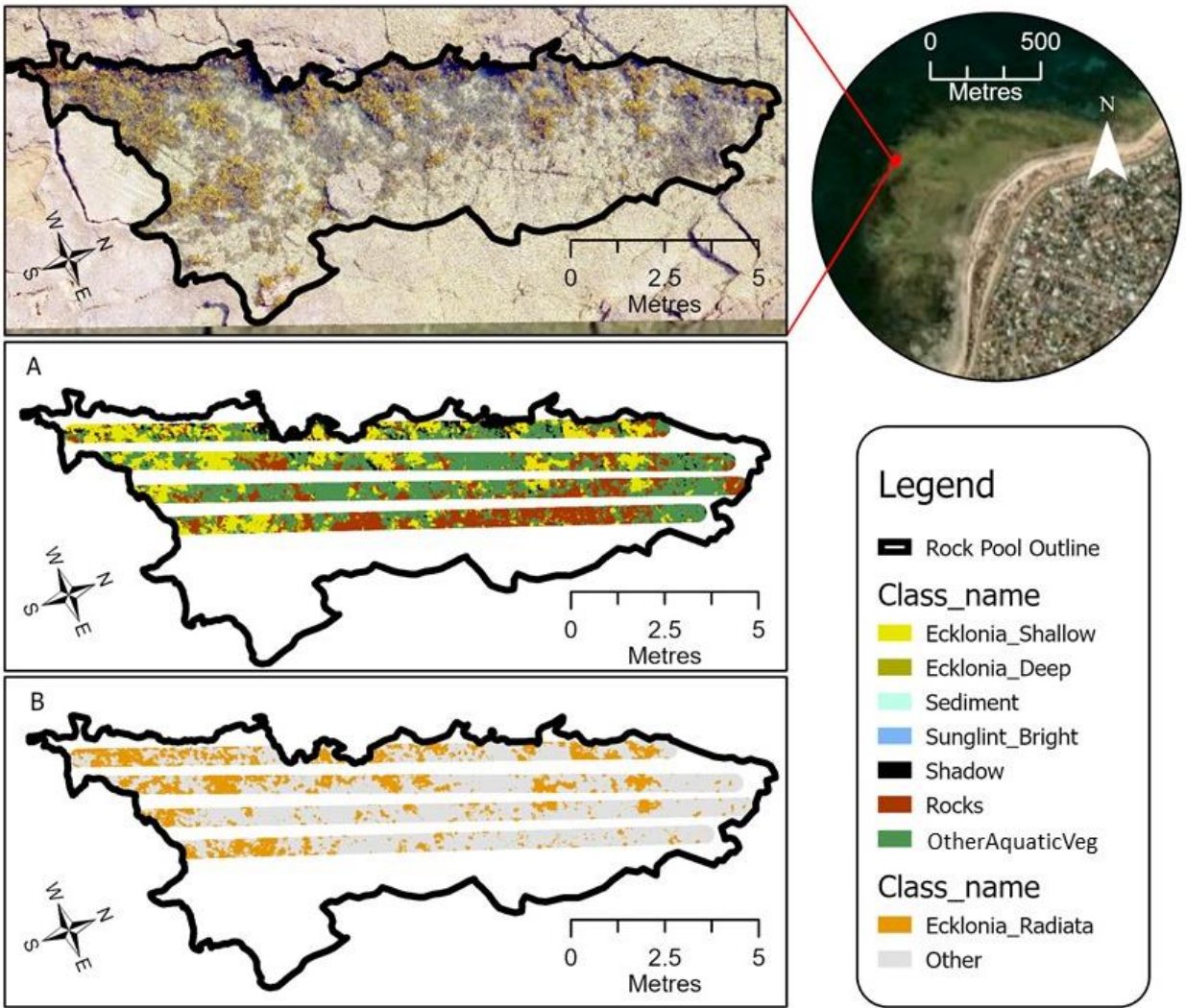


Figure 4:8: Classified validation transects in the West Shallow (WS) Rockpool

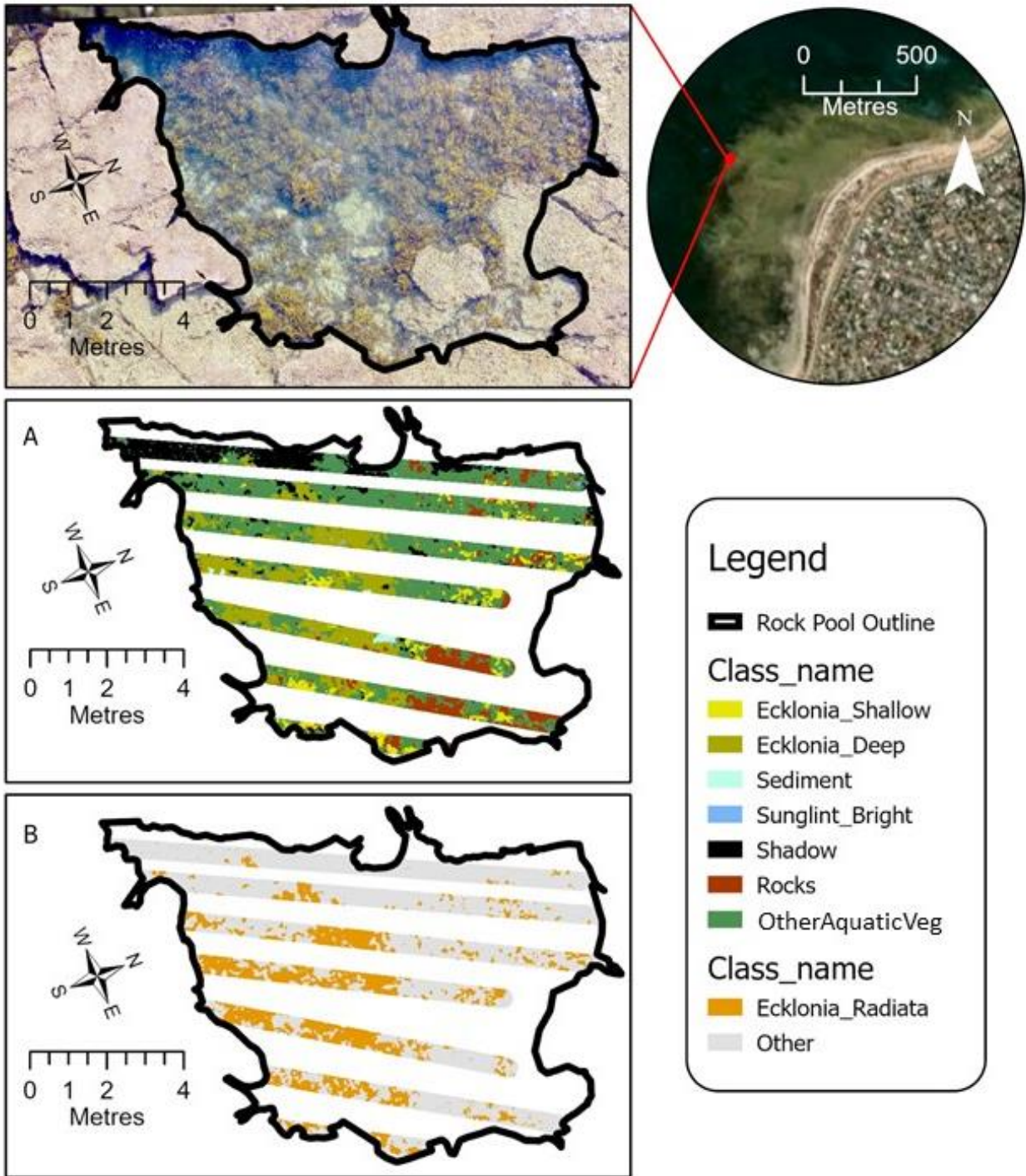


Figure 4:9: Classified validation transects in the West Deep (WD) Rockpool

Table 4:5: Percentage of *E. radiata* from SVM classifier for individual transects lines of all rockpools in shallow subtidal and intertidal zone (Zone I) and percentage of *E. radiata* for each rockpool separately.

<i>Rockpool Name</i>	<i>Individual Transects</i>	<i>Percent E. radiata</i>
<i>North Shallow (NS)</i>	NS_T1	13.87
	NS_T2	24.39
	NS_T3	34.13
	NS_T4	24.36
	NS_T5	24.13
	NS_T6	23.39
	NS_T7	20.79
<i>West Shallow (WS)</i>	WS_T1	36.47
	WS_T2	30.63
	WS_T3	15.95
	WS_T4	19.98
<i>West Deep (WD)</i>	WD_T1	2.49
	WD_T2	11.01
	WD_T3	29.85
	WD_T4	50.07
	WD_T5	44.42
	WD_T6	29.11
	WD_T7	19.06
<i>Rockpool Name</i>	Combined transects for each rockpool	Percent <i>E. radiata</i>
<i>North Shallow (NS)</i>	NS	23.52
<i>West Shallow (WS)</i>	WS	25.93
<i>West Deep (WD)</i>	WD	24.63

The percentage cover of *E. radiata* identified for individual transect lines and for the whole image can be seen in Table 4:5. It shows that the overall percent of classification of *E. radiata* in all these rock pools are very similar with the highest cover of 25.93% in WS. 24.63 in WD and the least cover of 23.52% in NS. The transect line with the lowest percent of *E. radiata* 2.4% is located over DS and a quick look at the unclassified UAV image on top of Figure 4:9 shows that this is the line with the highest amount of shadow.

4.3 Image Classification Outputs for Individual Images Over Study Area

Figure 4:10 and Figure 4:11 shows the result of image classification of the individual image mosaic over the whole study area, with broad classes (Figure 4:10) and the *E. radiata* class alone (Figure 4:11). The image also shows Zone S in light green, which is the deeper subtidal zone and in the shallow subtidal and intertidal zone, Zone I, in cream colour.

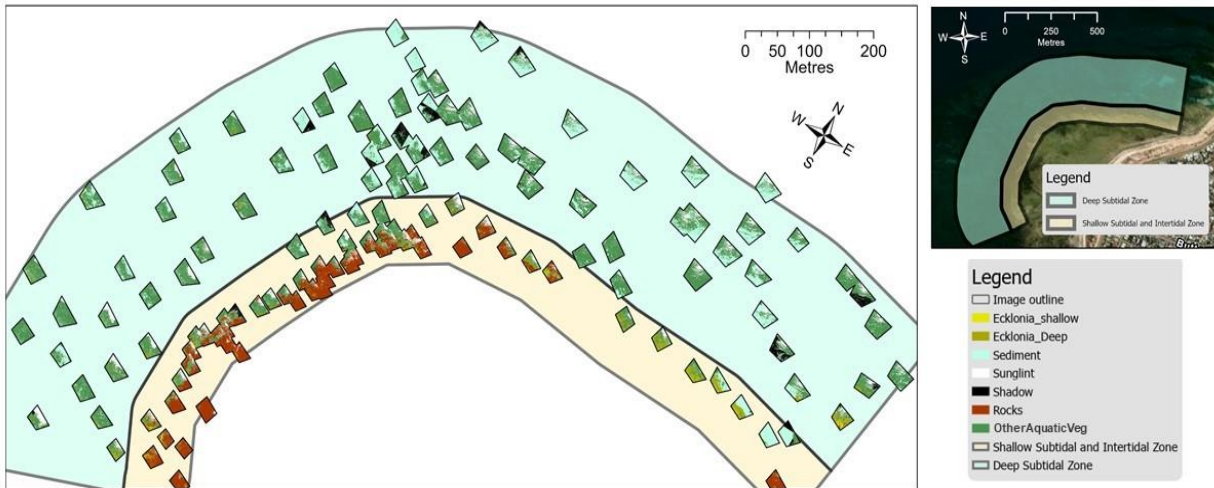


Figure 4:10: Classified individual images over the study area

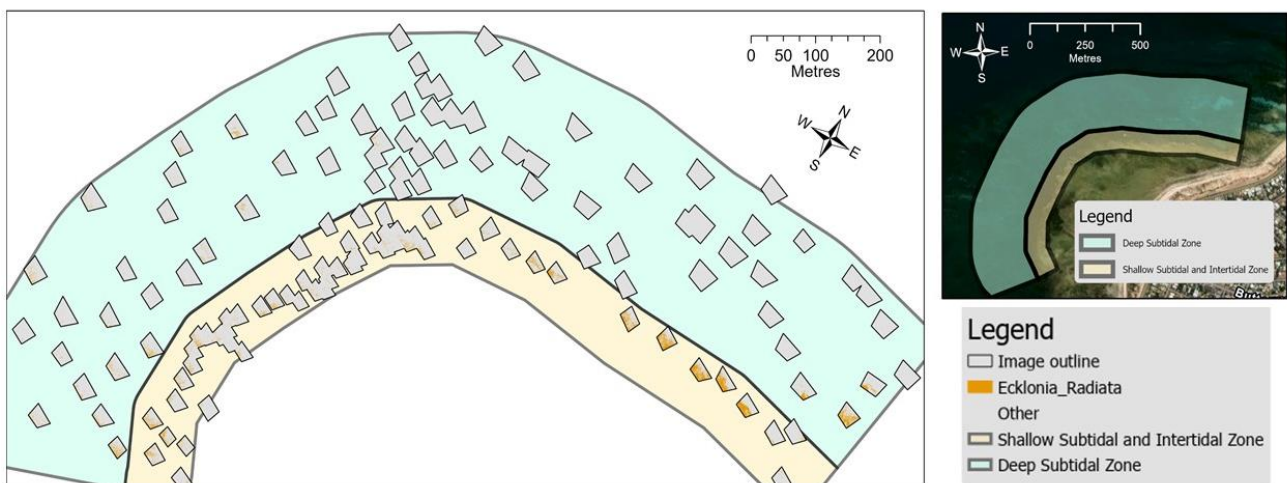


Figure 4:11: Reclassified individual images over the study area

Table 4:6: The percentage and area covered in *E. radiata* in the study area of Aldinga Reef

	Zone I	Zone S	Study Area
E. radiata in shallow water (%)	4.26	0.48	1.83
E. radiata in deep water (%)	5.09	1.50	2.78
E. radiata (%)	9.35	1.98	4.60
Total Area covered in the study (m ²)	28733.04	52075.48	80808.53
Area covered in shallow E. radiata (m ²)	1224.72	250.78	1475.50
Area covered in deep E. radiata (m ²)	1462.68	780.98	2243.66
Area covered in E. radiata (m ²)	2687.40	1031.76	3719.16
Area covered in the study (ha)	2.87	5.21	8.08
Area covered in shallow E. radiata (ha)	0.12	0.03	0.15
Area covered in deep E. radiata (ha)	0.15	0.08	0.22
Area covered in E. radiata (ha)	0.27	0.10	0.37

Table 4:6 shows the quantitative results from SVM classification of individual image mosaic over the whole study area. Zone I covered an area of 2.87 ha of land calculated from images and Zone S covered 5.21 ha. Across this area 9.4% in Zone I was covered by *E. radiata* (e.g. 2687 m²) and only 2 % was covered by *E. radiata*. *Ecklonia radiata* cover percentage for the whole study area was calculated at 4.6 %, which is 3719 m².

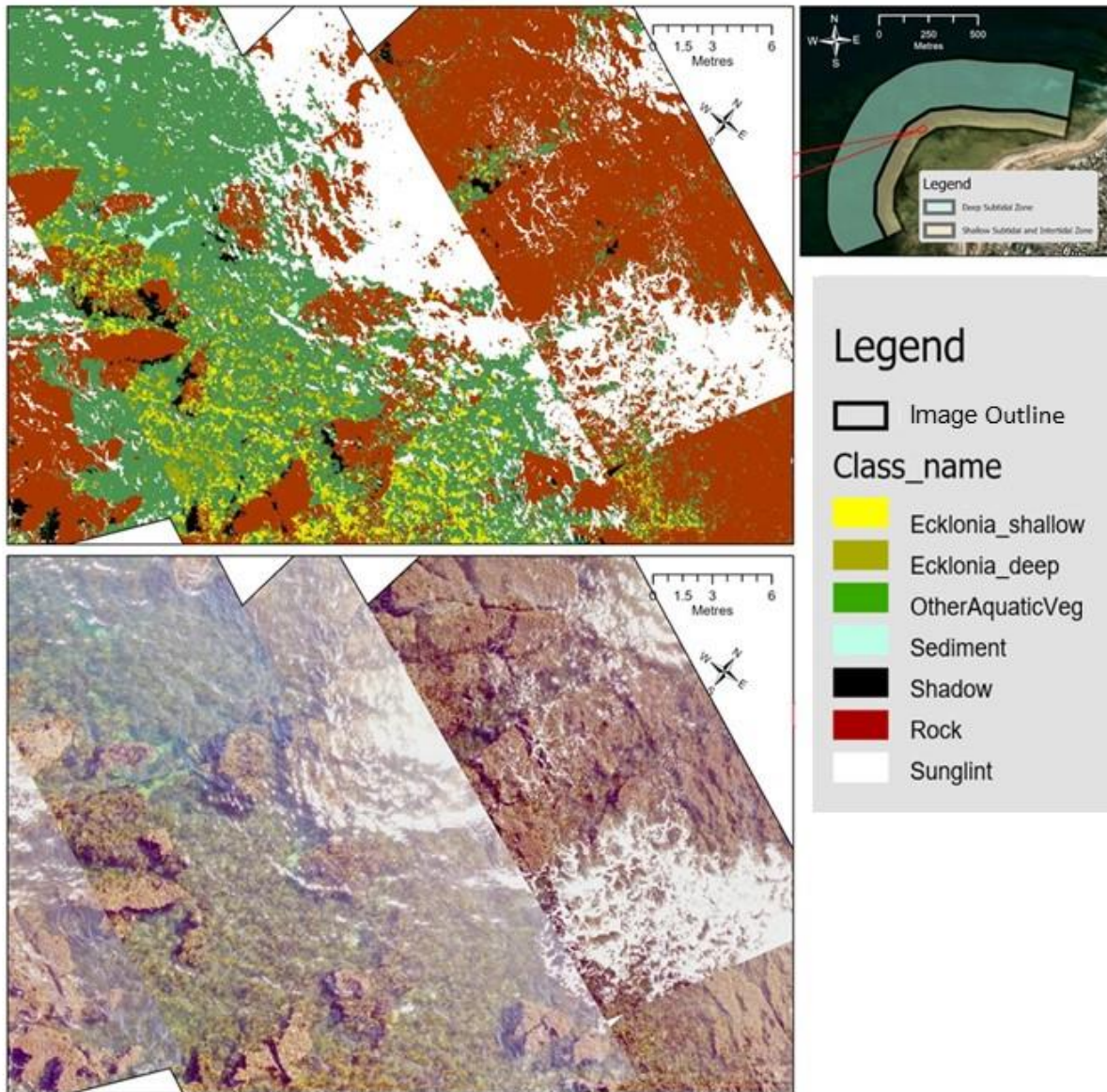


Figure 4:12: This figure shows classified individual images in the West of the study area at the top, and unclassified RGB mosaic of the same area at the bottom.

Figure 4:12 shows a section of the mosaic of individual images captured over the study area. It can be seen that the classification model was able to classify *E. radiata* in shallow water in the intertidal and shallow subtidal environments. It managed to classify the broad classes of rock, sediment, bright sun glint and shadow. Because of the spectral similarity of foam (from breaking water) and sun glint, foam it was classified into the bright sun glint class. Boundaries between images as a result of changes in illumination in across an oblique image, was also a problem in the individual image datasets and is obvious where images overlapped (Figure 4:12).

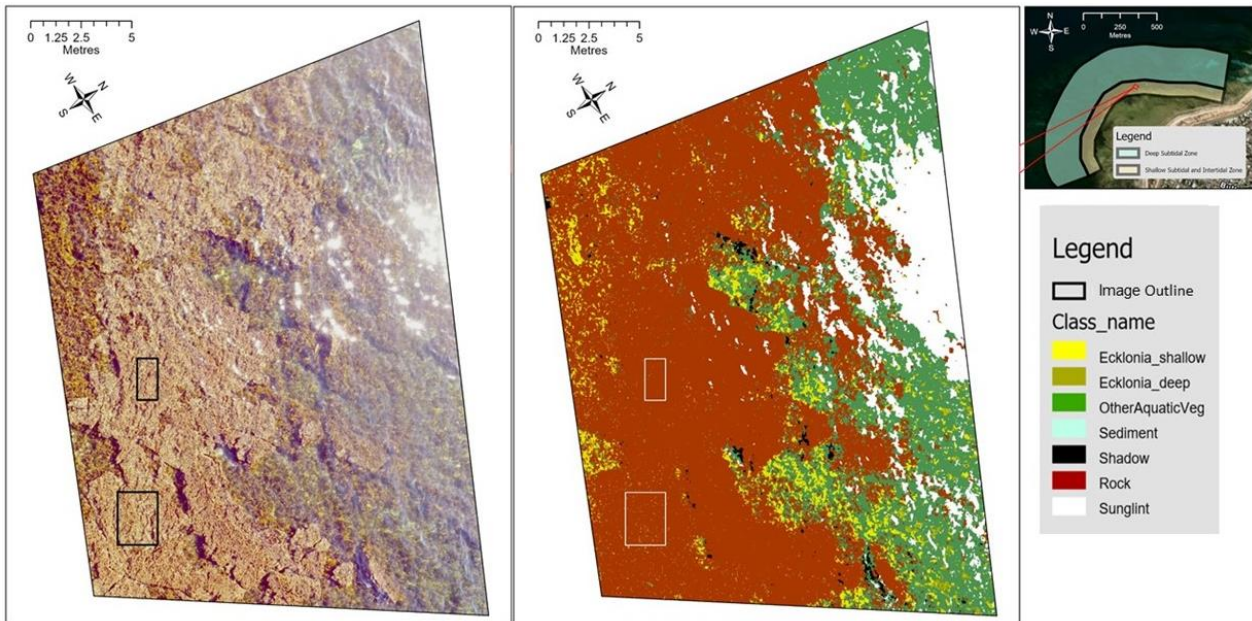


Figure 4:13: Classified individual image in Northwest of the study area showing good classification of Ecklonia in shallow water and boxes showing good removal of sun glint.

Shallow water sun glint was initially a problem identified in shallow water (Zone I) which resulted in it being misclassified as shallow water *E. radiata*. This issue was resolved by increasing segment size in the classification wizard from 5 pixels to 10 pixels. As seen in Figure 4:13, there is very little misclassification (highlighted by boxes) of shallow water sun glint as *E. radiata* in the intertidal zone of the image. However, in the subtidal area, bright sun glint appeared in the most spectrally distorted part of the image to the left where even bright sun glint was over classified and visibility underneath it was obstructed.

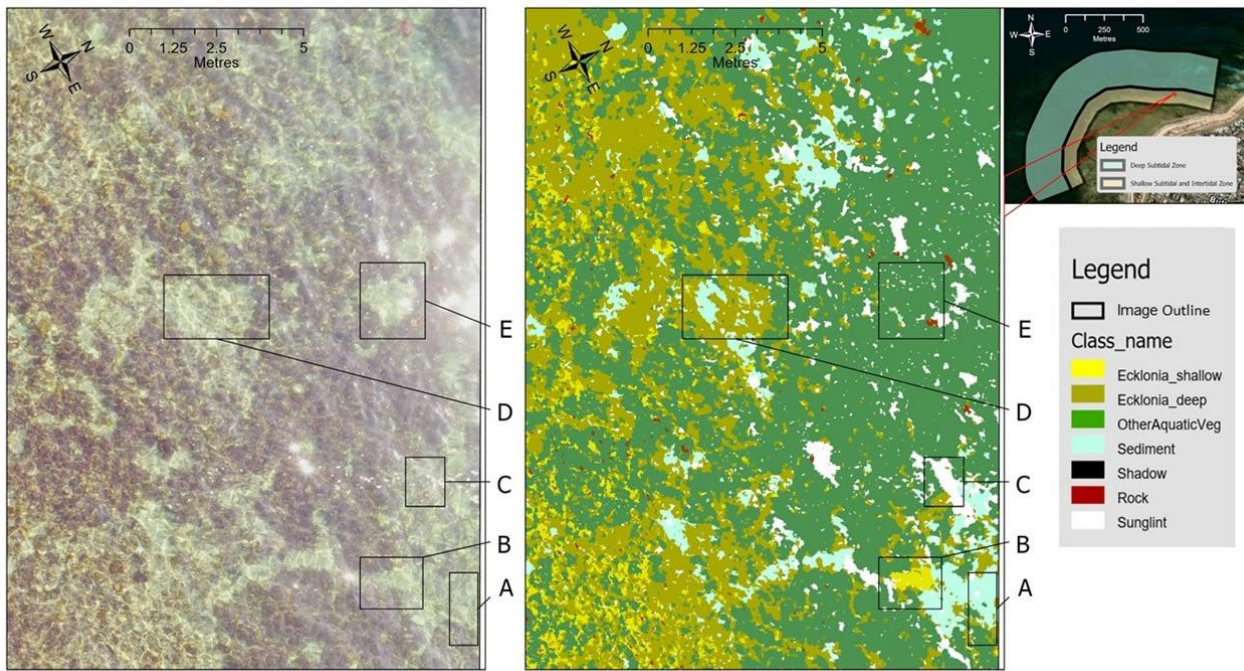


Figure 4:14: Sediment in shallow water misclassified as various classes

The issue of shallow water sun glint misclassification was resolved over rock substrate as seen in Figure 4:13. However, when shallow water sun glint was present over sediment, it gets misclassified into various classes. Sometimes sediment was correctly classified as seen in box A of Figure 4:14. But it gets misclassified as *E. radiata* in shallow water (box B), as *E. radiata* in deep water (box D), as other aquatic vegetation (box E) and when next to bright sun glint, as bright sun glint (box C). More sediment is present in very shallow water in the North and South side of zone I, which means this issue may lead to sediment getting classified as *E. radiata* in these environments.

4.4 Validation and Accuracy Assessment

Validation data collected from the field observations of rockpools and from dive transects were compared to the results from SVM classification on UAV images to identify the accuracy this method.

4.4.1 Validation and accuracy assessment in Zone S

Table 4:7 Percent accuracy of the SVM classifier to detect *E. radiata* in the deep subtidal zone (Zone S)

	West Dive Transects			North Dive Transects			South Dive Transects		
	WT1	WT2	WT3	NT1	NT2	NT3	ST1	ST2	ST3
SVM Classifier									
% Ecklonia_Shallow	3	2	8.1	1	1.9	3.9	42.2	42.7	23.9
% Ecklonia_Deep	4.4	3.5	14	0	0.4	10.9	0.4	0.3	0.7
% Ecklonia_Combined	7.4	5.4	22.2	1.1	2.3	14.8	42.5	43.1	24.6
Validation									
% Ecklonia_Shallow	11.9	17.9	24.6	-	-	-	-	-	-
% Ecklonia_Combined	24.2	32.6	55.7	0	0	0	9.4	10	44
Percent Accuracy									
Ecklonia_Shallow	97.4	87.5	98.2	-	-	-	-	-	-
Ecklonia_Combined	83.4	72.8	66.6	98.9	97.7	85.2	66.9	66.9	80.6
Combined Transects									
	West	North	South						
SVM Classifier									
% Ecklonia_Shallow	4.3	2.3	36.3						
% Ecklonia_Deep	7.2	3.9	0.5						
% Ecklonia_Combined	11.5	6.2	36.8						
Validation									
% Ecklonia_Shallow	18.2	-	-						
% Ecklonia_Combined	37.5	0	21						
Depth estimate (m)	2.7	1.9	1.5						
Percent Accuracy									
Ecklonia_Shallow	94	-	-						
Ecklonia_Combined	74	93.8	84.2						

Table 4:7 shows the percentage of *E. radiata* identified from SVM classifier, from validation and the percent accuracy of SVM classifier. This is given for each individual transect line and the combined value from all transects for each dive validation area (north, south, and west) is given. In the West dive transects the percentage of *E. radiata* on rock pinnacles were calculated and labelled as "Validation % Ecklonia_Shallow". This information is absent in other areas (North and South) due to the lack of such large rock pinnacles.

The dive validation data from Zone S showed that the highest percentage of *E. radiata* was found in the West with an overall percent cover of 37.5 % and the transect with the highest percent *E. radiata* was WT3 at 55 %. In contrast, validation data from Northern transects yielded no records of *E. radiata*. Validation data showed that there was a percent cover of 21% *E. radiata* in the South transects. The validation videos showed that larger homogenous patches of *E. radiata* were found

in the transects in the West area. In comparison, *E. radiata* found in South transects were patchy and more mixed with other types of vegetation.

The percentage of *E. radiata* classified in Zone S varied across different validation areas as seen from Table 4:7 The overall percentage of *E. radiata* detected for each validation area, was identified by combining the three transects in each area. It showed that the SVM method under-classified the percent cover of *E. radiata* in the West (SVM: 11.5%, Validation: 37.5%, % Accuracy 74%), and North validation area (SVM: 6.2%, Validation: 1.9%, % Accuracy 93.8%), and overclassified *E. radiata* in the South validation area (SVM: 36.8%, Validation: 21%, % Accuracy 84.2%). However, *E. radiata* over rock pinnacles (e.g. shallow Ecklonia) in the West transects had a higher accuracy (SVM: 11.5%, Validation: 18.2%, % Accuracy 94%) compared to the same transects when distinction of pinnacles was not made.

4.4.2 Validation and accuracy assessment in Zone I

Table 4:8: Percent Accuracy of SVM classifier to detect *E. radiata* in shallow subtidal and intertidal zone (Zone I)

Transect Label*	Av Depth (cm)	SVM	Validation	% Accuracy
NS_T1	35.78	13.87	20.00	93.87
NS_T2	38.50	24.39	20.00	95.61
NS_T3	34.00	34.13	27.27	93.14
NS_T4	45.00	24.36	20.00	95.64
NS_T5	36.85	24.13	37.50	86.63
NS_T6	35.00	23.39	50.00	73.39
NS_T7	33.40	20.79	0.00	79.21
WS_T1	53.91	36.47	78.79	57.68
WS_T2	55.32	30.63	45.71	84.92
WS_T3	48.88	15.95	12.12	96.17
WS_T4	44.29	19.98	21.88	98.10
WD_T1	78.80	2.49	73.07	29.42
WD_T2	98.60	11.01	90.48	20.53
WD_T3	98.80	29.85	56.52	73.33
WD_T4	108.40	50.07	58.82	91.25
WD_T5	99.20	44.42	33.33	88.91
WD_T6	78.1	29.11	35.71	93.40
WD_T7	89.3	19.06	75.00	44.06

Rockpool Label*	Av Depth (cm)	SVM	Validation	% Accuracy
NS	37.3	23.52	22.54	99.02
WS	49.9	25.93	38.41	87.52
WD	89.3	24.63	63.11	61.52

*NS: North Shallow Rockpool, WS: West Shallow Rockpool, WD: West Deep Rockpool, and T: Transect

The overall validation values and the classification values for the rockpools are much closer as seen in Table 4:8. Based on validation values the highest percentage of *E. radiata* is found in West Deep (WD) rockpool 63.1%, followed by West Shallow (WS) rockpool (38.4%) and North Shallow (NS) rockpool (22.5%). However, the accuracy is the lowest in WD with SVM classifying much lower (24.6%) than the validation value. It shows that an overall classification accuracy is highest in both the shallow rock pools (NS: 99% and WS: 87.5%). Accuracy is much lower in the deeper rockpool (WD:61.5%). To observe this trend, the average depth and percent accuracy of *E. radiata* detection of all transects were plotted against each other as shown in Figure 4:15. This identified that percent accuracy of *E. radiata* detection declined with increasing water depth. Accuracy of classification of *E. radiata* in rock pools declined from 80% at a depth of around 55 cm to an accuracy of 70% at 81 cm.

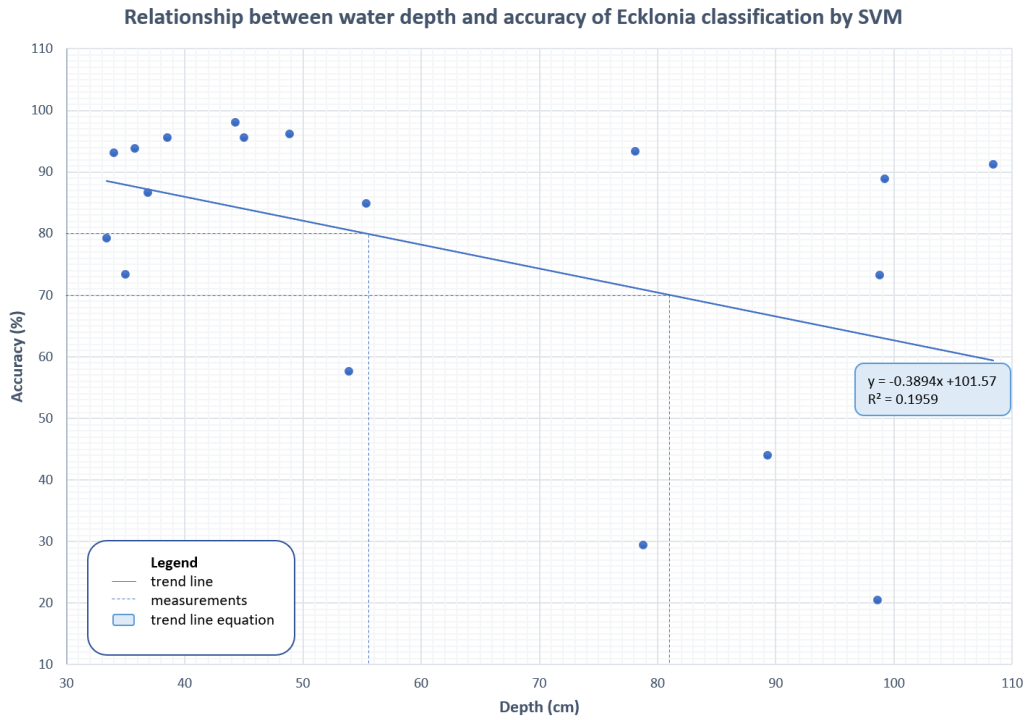


Figure 4:15: Exploring the relationship between accuracy and *E. radiata* detection using SVM changes with depth in rockpools (validation sites in zone I)

The extent of shadow formation in the deeper rockpool (WD) can be seen in Figure 4:9. Both Figure 4:9 and Table 4:5 shows the effect that shadow had on the classification of transect line WD-T1. WD-T1 has a validation value of 73% *E. radiata* but SVM classifies only 29% *E. radiata* in this transect line.

5 DISCUSSION

5.1 Optimum observational requirements and conditions for mapping *E. radiata* using UAV imagery at Aldinga Reef

5.1.1 Sensors and multispectral bands

As literature suggests the best bands to use for optical benthic mapping is within the visible spectrum due to its ability to penetrate water (Hedley et al. 2016). The RGB bands of all the sensors tested were able to capture *E. radiata* underwater. The NIR band from the Parrot Sequoia sensor was tested to check if it could be used as a proxy for sun glint removal with the assumption that NIR would be totally absorbed by water (Kay, Hedley & Lavender 2009). However, the data collected was not useful as reflectance was not measured over water in this study.

The chlorophyll content in aquatic vegetation reflects Near Infrared (NIR) and Short Wave Infrared (SWIR) wavelengths and can be easily detected if it emerges over water at low tide, or if it is present in very shallow water (< 2 m) (Kutser, Vahtmäe & Praks 2009). Therefore, it was considered that the NIR sensor could be useful to detect *E. radiata* in this study. However, in the subtidal zones where the Parrot Sequoia was tested, there were no reflectance identified in the NIR band and it was deduced that the water was not physically or optically shallow enough to reflect NIR from *E. radiata*.

Due to the lack of measured IR reflectance over water for vegetation detection or for NIR based sun glint correction methods, it was concluded that the spectral resolution of the Parrot Sequoia sensor was not sensitive enough to be useful in this research. Furthermore, RGB images captured structural detail of *E. radiata* in both shallow and deep water. Therefore, RGB images were considered more useful and practical for this research.

5.1.2 Operational Conditions and UAV flying requirements

Depending on the need of the research, *E. radiata* maybe detected at higher UAV flying altitudes as identified in this study (shown in Table 4:2). Recommendation of a 30 m flying altitude by Selvaraj (2021) for UAV multispectral imagery when tested out on RGB images for this study was adequate to detect *E. radiata*. However, in order to compensate for the lack of multiple 4 or 5 bands, it was decided to improve on spatial detail as suggested by Riniatsih et al. (2021) for RGB images. Flying at varying altitudes showed that flying and hovering the UAV at 20 m altitude to capture images provided more details on fronds despite its movement under water with wave action in subtidal zones. Higher flying altitudes could be used in more complex classification models because *E. radiata* was visible to the naked eye at 60-50 m. Flying at such an altitude may work out when using a physics-based classification with atmospheric and water column correction and spectral library incorporation into the classification model to detect *E. radiata*, rather than when using a simple empirical classification model as the one used in this study. However, the flying altitude of 20 m

combined with the simple empirical classification model proposed was able to distinguish between *E. radiata* in shallow water and *E. radiata* in deeper water. Furthermore, this flying altitude may vary depending on the sensor specifications such as sensor width, FOV and image dimensions of the sensor.

The decision to collect low altitude images meant that the spatial extent of imagery collected was compromised for higher spatial detail. Flying at such an altitude, was carried out with the awareness that generating an image mosaic of the whole study area cannot be practically achieved for a research project of this scale and time frame. This was especially true considering the logistics of fieldwork and the stormy weather conditions that are typical of a South Australian winter. Also, the restrictions in conditions that heighten the sensitivity of *E. radiata* detection to tide and illumination and the restriction of UAV flight to weather conditions (Davies-Colley et al. 2014; Gallegos & Moore 2000; Green et al. 2000; Mount 2005; Mustard, Staid & Fripp 2001; Tait et al. 2019; Tait, Orchard & Schiel 2021)

Light attenuation with increasing water depth as identified in this study and by Gallegos and Moore (2000) showed that even a slight depth variation can lead to exponential loss of image clarity. As a result of this rapid change images captured at low tide is recommended when using RGB without water column correction for classification of *E. radiata* in shallow water (Tait, Orchard & Schiel 2021). However, careful consideration must be given to wind direction and atmospheric pressure when considering tidal levels, as onshore winds and low atmospheric pressure push up the water level on to the intertidal and shallow subtidal zones, increasing the depth of predicted tides (Shan, Hannah & Wu 2020). Consequently, low tide levels in combination with high atmospheric pressure are important considerations to reduce water column depth in order to detect *E. radiata* using UAV.

In the visible spectrum, the light absorption is much faster in the red band than in the blue band (Gallegos & Moore 2000). *Ecklonia radiata* in shallow water had a unique golden colour that was useful to visually delineate them from the other benthic features. The spectral profile in Figure 3:7 showed this colour in shallow water which disappears rapidly with red band as a result of water attenuation, hence *E. radiata* in deeper water is spectrally similar to other macroalgae. Therefore, the lowest possible tide is recommended (Tait Orchard & Schiel 2021) for collecting images of *E. radiata* in shallow water.

UAV images were captured when the sun altitude was between 22° - 41°. Images captured with sun altitudes as low as 22° can be used to identify *E. radiata* if the sun is bright, cloud cover is minimum, and the tide is low. UAV image capture with high sun altitude is not recommended by Mount (2005) and Joyce et al. (2019). However, high sun altitude had little impact from bright sun glint in images captured over the intertidal zone. This observation agrees with the favourable sun altitude range suggested by Mustard, Staid & Fripp (2001). Although, in this study higher sun angle generated sun

glint in the subtidal zone where wave action was also higher. Capturing imagery at midday in cloud cover is considered an alternative when polarising filters are not available to reduce sun glint over water (Joyce et al. 2019; Kay, Hedley & Lavender 2009). However, images captured in these conditions lose the unique golden spectra of *E. radiata*. Furthermore, dull, sun glint was observed over water which obstructed the view underneath. Therefore, image capture with cloud cover to identify *E. radiata* is not recommended.

Joyce et al. (2019) recommends tilting the image by a slight angle roughly 15° to reduce glint from the edges of the images. Images in this study were captured with camera tilt that aligned to the sun altitude with tilt angles that ranged from 22° - 41° , which were at a higher tilt range than recommended. The increase in tilt had little impact on individual images used to map the study area if it was in the intertidal zone. Mosaicking of overlapping oblique imagery over the dive validation transects also minimised some issues that emerged with this distortion as suggested by (Flynn & Chapra 2014). However, the impact of distortion from oblique imagery with higher tilt angles experienced geometric issues as suggested by (Joyce et al. 2019). Oblique images captured had a change in illumination across the image with better visibility in the less distorted side of the image details. This issue can be corrected with cosine function if the tilt angle is known or can be calculated (Li & Guo 2015). It can also be corrected with the use of a polarising filter (Cherian et al 2021). However, this correction was not made on the images used in this study due to time and resource constraints. The low radiometric resolution of 8-bit imagery from Mavic 2 Pro meant that the change in illumination in oblique images and from sun glint contribute to the loss of spectral detail in order to discriminate details needed to identify *E. radiata* in individual oblique images in Zone S. Furthermore, the impact of this loss is visible in individual image dataset with poor segmentation (Orych et al 2014) in the distorted part of the oblique images over deeper water. This issue was minimum in the mosaics of overlapping images over validation transects in Zone S. Yet, even in these overlapping images, as a result of mosaicking without correction for the change in illumination, resulted in straight boundaries that led to abrupt changes in classification accuracy along these straight lines (Figure 4:3Figure 4:4Figure 4:5Figure 4:12)

Ripples and waves over shallow water contributed to reduced quality of images, which are not favourable conditions for data collection (Mount 2005). However, in images captured at both low and high tide, if the sun angle is in the ideal $20-35^\circ$ range and even a higher angle such as 41° , ripples and waves do not obscure shallow *E. radiata* despite adding a slight blurring effect from wave motion. Ripples and waves over shallow water are less of an issue if the water column is illuminated properly. When a wave breaks over the subtidal zone creating foam which is spectrally similar to bright sun glint, or when the crest of the wave reflects bright sun glint it obscures the features in the water beneath it rendering classification difficult. Therefore, bright sun light penetrating the water column is a key factor and ripples and wave action from wind speeds less than 30 km/hr is not a severe

issue. Further, if the environment has a higher sediment content, like in the North validation transects, low wind speeds below 18 km/hr are recommended (Mount 2005) and lower wave action can greatly increase visibility. The best quality images captured over the high sediment validation area in the North were captured on a day with wind speeds between 10-24km/hr in agreement with Mount (2005). However, good quality images of *E. radiata* for SVM classification in shallow water can be captured with wind speeds around 30 km/hr within the desirable sun angle and without cloud cover.

5.2 Extent to which UAV RGB imagery can be used to detect *E. radiata*

5.2.1 Deep Subtidal Zone (Zone S)

The percentage of *E. radiata* classified in Zone S showed variation in percentage of *E. radiata* present (validation), classified (SVM) and in accuracy of detecting it. It showed that the SVM method under-classified in the West and the North validation area and overclassified in the South validation area. However, *E. radiata* over rock pinnacles (shallow Ecklonia) in the West was classified with a higher accuracy. The results from the West dive transect lines were of interest because the dive validation data generated the highest overall cover of *E. radiata* (37.5%) in this area along with large homogeneous patches of it observed from the validation videos. The accuracy of SVM classification of *E. radiata* over the rock pinnacles was higher (94%) but the accuracy dropped in the SVM classification when no such depth related distinction was made (74%) This indicates that the SVM method was struggling to classify *E. radiata* in water that is approximately at a depth of 2.7 m but classified *E. radiata* over the rock pinnacles very accurately. This observation supports the effect the water column has on spectral properties of *E. radiata* (Selvaraj, Case & White 2021; Wicaksono & Lazuardi 2018) due to light attenuation (Gallegos & Moore 2000; Green et al. 2000).

South dive transects were of interest because this area had high heterogeneity due to a complex mix of various macroalgae and seagrass communities. Furthermore, this area had the highest vegetation cover as observed from dive validation videos and aerial images. Small, segmented patches of *E. radiata* were detected in ST1 (9.4%) and ST2 (10%) in contrast to large homogenous patches of *E. radiata* observed in ST3 (44.4%). The estimated water depth in the South dive transects (1.9m) was lower than the West transects (2.7m). Despite the shallower water, In ST3 with the largest homogenous *E. radiata* patches (44%), SVM under classified (24.6%) but displayed the highest overall accuracy (80.6%) in comparison to the rest of the transects (both ST1 and ST2 = 66.9%). It is interesting to note that heterogeneous environments present poor accuracy issues even within high spectral resolution in hyperspectral imagery (Ashraf, Brabyn & Hicks 2012). Furthermore, it should be reiterated that other macroalgae such as *Sargassum* spp. are reported to have a very similar spectral signature to that of *E. radiata* (Harvey 2009) and those other species are found in abundance at Aldinga reef (Wegener 1995). Kutser et al. (2020) noted that spectral similarities exist in general even between broad classes of seaweeds. Ashraf, Brabyn and Hicks (2012) suggest the

use of high spatial resolution imagery to resolve this issue. Considering the issue of spectral similarities of *E. radiata* with other macroalgae species (Kutser et al. 2020; Harvey 2009) both high spatial and high spectral resolution is needed to resolve the misclassification in heterogeneous environments. In contrast to ST1 and ST2 the issue of under classification in ST3 over homogeneous patches of *E. radiata* can be attributed to water attenuation.

The North transects (NT1, NT2, NT3) did not yield any *E. radiata* cover from validation. This aligns with SVM classification of very low percent cover (NT1:1.1 % and NT2: 2.3 %) in those transects. North transects also had the highest amount of sediment and turbidity. The attenuation of light due to this turbidity maybe the cause of spectral confusion (Davies-Colley et al. 2014; Gallegos & Moore 2000; Green et al. 2000) in NT3 misclassifying *E. radiata* because of turbid conditions. Furthermore, despite high accuracy of classification (93.8%) the lack of *E. radiata* in the validation transects make this area a poor location to assess SVM's accuracy for detecting *E. radiata*, especially in deeper waters.

5.2.2 Deep Subtidal Zone (Zone I)

The percentage accuracy at which of *E. radiata* was very high in the shallow rock pools in Zone I with an accuracy of 99% in the shallowest NS rockpool and 87.5% in WS shallow rockpool. However, the deepest rockpools accuracy is low to (61.5%). This clear transition from high accuracy to low accuracy in SVM classifiers ability to detect *E. radiata* reinforce the effect of light attenuation in water. The percent accuracy of *E. radiata* in each validation transect was plotted against its average depth and a best fit line shows a decline in accuracy at a rapid rate (-0.4 percent by cm of water depth) which supports light attenuation even in very shallow water ((Gallegos & Moore 2000; Green et al 2000). The confounding effect of shadow in high spatial resolution imagery (Lu & Weng 2007) and its negative effect on image classification can be seen in transect line WD-T1 in West Deep rockpool. WT-T1 had a validation value of 73% *E. radiata* but SVM classified only 2.5%. Hence, the overall and individual transects lines indicate how depth and water attenuation changes the ability of SVM to detect *E. radiata* accurately.

5.2.3 Individual Images Over the whole study area

The classification outputs of individual image dataset showed an issue that was not dominant in the images over the validation zones. The issue of change in illumination across the oblique image, in section 5.1, was more obvious in the individual image dataset. This was because there was less overlap of imagery to minimise it. As a consequence of the diminished quality of the most distorted part of the image, segmentation was poor (Orych et al 2014) and the classified images showed abrupt boundaries in classification. This could have been corrected with a cosine function (Li & Guo 2015) or with the use of a polarising filter (Cherian et al 2021) as explained in section 5.1 above. The dataset also showed that SVM misclassified sediment in shallow water into various classes

including deep and shallow Ecklonia classes which was again a source of error which was not identified over validation rock pools. This issue may be linked to the loss of spectral quality in oblique images captured in the dataset. This issue may not have been identified in validation images captured over rock pools because they were nadir images with no oblique illumination.

5.3 Percentage Cover and Distribution of *E. radiata* in Aldinga Reef

5.3.1 Distribution of *E. radiata* at Zone S

The validation transects showed that the highest percent cover of *E. radiata* from validation data was in the western transects (37.5%) followed by the southern transects (21%) and lowest in the northern transects (0%). Although the differences across these areas may not be accurately aligned with SVM classification (highest 36.8% in South, followed by 11.5% in West and 6.2% in North) due to misclassification, the validation data is useful to describe possible variation in *E. radiata* distribution across various locations in Aldinga reef with varying environments factors.

The physical variability in the subtidal zones can be seen from the descriptions in Table 3:5. The validation videos showed that there was a high amount of sediment in the North transects, very low visibility and visible suspended load. *E. radiata* is normally rare where sediment content is high (Connell, SD 2005) as high sediment content inhibits the recruitment of *E. radiata* gametophytes (Kennelly 1987a; Tatsumi & Wright 2016). This may explain the lack of *E. radiata* observed in the validation transect in the North area. The sediment in the Northern side of the reef may be explained by the predominant southerly wind and net northerly movement of beach sediment with longshore drift along the Adelaide Metropolitan Coastline (McDowell, Green & Griffante 2009). Wegener (1995) identified Sellicks Creek Catchment as a main source of sediment load in Aldinga Reef. Erosion of sediment from the soft dunes at Aldinga beach is highlighted as an issue (Western et al 2020), which might be contributing to higher sediment and organic content to the Northern side of the reef. In addition to sediment, nitrogen enrichment has been a cause of *E. radiata* loss elsewhere (Gorman & Connell 2009) and it is worth noting the presence of two storm water drains in Aldinga with one draining into the dune while the other in the north draining to the beach opposite to where North transects were collected (see Figure 1:6). Sediment, organic matter and nutrients accumulating in the Northern area may explain the lack of *E. radiata* found in North validation transects, which are representative of the northern area of the beach.

Unlike the Northern validation area, both South and West validation areas had clearer water with less sediment but more rock substrate. The beach profile on the South is more gradual compared to the West where there is an abrupt step from the intertidal to subtidal zone allowing waves to break on the intertidal platform. Aldinga Reef is exposed to moderate wave energy (Wegener 1995), which is considered favourable for *E. radiata* (Wernberg & Connell 2008) along with clear oligotrophic water

with more dissolved oxygen and less sediment (Wernberg et al. 2010). The gradual slope in the South section of Aldinga reef may give more time for the waves to dissipate and refract (Hughes 2016) compared to the Western side of the reef. This may explain the heterogeneity in vegetation as lower wave exposure environments lead to *E. radiata* being replaced by other canopy macroalgae (Wernberg, & Connell 2008). In contrast to the Southern area of the reef, the sudden step in the reef platform from the intertidal to subtidal zone in the Western area of the reef has waves with higher energy. At low tide, waves break on the intertidal zone, and this is where the deepest rockpools, with abundant *E. radiata*, are also located. This continuous movement and circulation of water at the Western side could be the reason for the higher percentage of *E. radiata* observed in the Western transects, as water action, and clear oligotrophic water are conditions favoured by *E. radiata* (Wernberg et al. 2019a; Wernberg et al. 2010)

5.3.2 Percent Cover of *E. radiata* in the Study Area

The image classification over Zone S estimated *E. radiata* percent cover of 1.98 %, which is 1032 m² (0.1 ha) of area covered. However, this percentage cannot be used as good estimate of *E. radiata* in deeper subtidal zones because of the poor accuracy of SVM to detect *E. radiata* in deeper waters. The accuracy of *E. radiata* classification in the validation transects in Zone S (deeper subtidal zone) was lower than desired. Therefore, the individual image dataset cannot be used with a high confidence to estimate the percent cover of *E. radiata* in Zone S of the study area.

The percentage of *E. radiata* cover in the shallow subtidal and intertidal zone (Zone I) was 9.3 % of the area covered from the imagery (excluding sun glint and shadow). This accounts to an area of 2687 m² (0.27 ha), which can be used as an estimate of area covered by *E. radiata* in Zone I of the study area. Thus, the estimated percent cover of *E. radiata* can be reported with a very high accuracy (99-87%) in intertidal zones but with a more variable accuracy in shallow subtidal zones (87-62%), depending on water depth and shadow.

However, it should be noted that the individual images mosaic used to estimate percentage of *E. radiata* cover in Zone I was different from the validation mosaic with overlapping images. The individual image mosaic had the confounding effect from image distortion, bright sun glint and depth, reducing its accuracy to values lower than estimated from validation sites in Zone I. This is because the mosaicked imagery over the transect lines minimised the confounding issues previously mentioned.

6 CONCLUSION AND RECOMMENDATION

6.1 Conclusion

6.1.1 Optimal observational conditions for mapping *E. radiata* using UAV imagery over Aldinga Reef

Ecklonia radiata can be detected very accurately in shallow subtidal and intertidal zones in Aldinga Reef when flying at an altitude of 20 m with broad RGB wavelengths. It is recommended to collect imagery when tide height is lowest because of the effect water attenuation has on *E. radiata*'s red spectral reflectance, making it spectrally similar to other aquatic vegetation in deeper water. Bright sunlight plays an equally important role when separating *E. radiata* in shallow water compared to deeper waters (e.g. > 2 m depth). It is important to observe wind direction and atmospheric pressure when identifying days of low tide for flying, especially in winter. This is because low atmospheric pressure and wind towards the coast pushes the water up further into the intertidal zone. When collecting imagery over intertidal zones both oblique and nadir images can be captured. Cloud cover, even at low tide and during mid-day is not recommended because the golden colour of shallow water *E. radiata* significantly reduce without bright sun light. It is recommended to capture images while flying direction is aligned to the sun azimuth angle and when capturing oblique images with tilt aligned to the sun altitude the UAV and camera should be flying away from the sun with the back of the camera facing the sun. The lack of bathymetry data at the fine scale needed for this study hindered its use for water column correction. However, if available it is recommended to use bathymetry data in future to modify pixel values for water attenuation (Green et al. 2000; Mumby et al. 1998)

In the intertidal zone images can be captured at high sun altitudes, while flying the UAV with a tilt that is greater than the recommended 15° by aligning the tilt to the angle of sun altitude. This captures shallow water sun glint which is spectrally similar to *E. radiata* in shallow water. However, it can be minimised by adjusting the minimum segment size to be smaller than the smallest kelp fronds visible in imagery. Furthermore, the study identified that images can be captured in wind speeds as high as 30 km/hr in intertidal zones.

In subtidal zones bright sun glint over water is an issue and can be reduced by flying at windspeeds lower than 18 km/hr (Mount 2005) and capturing nadir or oblique images as recommended by Joyce et al. (2019). Images captured with higher tilt angles, and stronger winds can work better when mosaiced as identified in validation transects in this study. Therefore, instead of individual images, small overlapping image mosaics of transects or quadrat areas could be flown as a sampling method.

6.1.2 *Ecklonia radiata* detection in intertidal and subtidal zones using UAV RGB imagery

Ecklonia radiata can be detected using the simple empirical method of image classification, using the Support Vector Machine (SVM) classifier, in shallow water (e.g. < 2 m depth) at Aldinga. However, accuracy of classification declines rapidly with increasing depth as observed at the validation sites in the rockpools at Zone I and from the dive validation transects, especially Western transects in Zone S. In the West transects, SVM struggled to classify *E. radiata* at 2.7 m water depth but managed to accurately classify *E. radiata* growing on rock pinnacles due to shallower depths. This shallow *E. radiata* found on rock pinnacles in the deeper subtidal zone were classified with similar accuracy to *E. radiata* found in very shallow water in Zone I. The South transects were over classified for percent cover of *E. radiata* where there was heterogenous aquatic vegetation as SVM struggled to differentiate between *E. radiata* and other vegetation with similar spectral properties when clustered together. However, the classification had higher accuracy in ST3 where more homogenous and larger patches were located. Due to the lack of *E. radiata* and due to the turbidity of water in the northern transects, the North transects were not the best to assess SVM's accuracy for classifying percent cover of *E. radiata*. However, it is worth noting that the area classified as *E. radiata* was low (in agreement with validation data) except in NT3 where there was possible misclassification due to higher turbidity

The rockpools in Zone I showed that *E. radiata* can be classified with accuracies ranging from 99-61% depending on the depth of water. The data from rockpools showed that SVM classification using this method over shallow subtidal zones (e.g. < 2m water depth) and intertidal zones will be very accurate.

Therefore, it can be concluded that *E. radiata* can be classified accurately in intertidal and shallow subtidal areas using the method proposed in this study. However, in deeper subtidal zones (i.e. > 2 m depth) this method is not very successful. However, the method can be tweaked to improve the classification outputs by flying UAV away from the sun, with a camera tilt or by capturing nadir images. If larger angles and higher windspeeds need to be included in future studies, then testing out the impact of a polarising filter is recommended

6.2 Recommendations

The design of this study may be enhanced in future by using a direct georeferencing method that has been proposed by Selvaraj (2021), which was not applied in this research due to its recent publication. However, it has the potential of speeding up the georeferencing process of imagery captured without ground control points over water. Furthermore, Increasing the positioning technologies and capabilities in drones may help speed-up the image capture and pre-processing

stage of images. RTK drones such as the Matrice 300 RTK, may help automatic geoprocessing and mosaicking of imagery over shallow water without *in-situ* measurement of ground control points.

A profound challenge faced when capturing imagery over water is the issue of sun glint. The study has shown that cloud cover, although it reduces sun glint (Joyce et al. 2019; Kay, Hedley & Lavender 2009) due to the lower intensity of light penetrating water (Joyce et al. 2019), it does this at the cost of compromising the magnitude of spectral reflectance of shallow water *E. radiata*. Therefore, when using a simple empirical method of image classification as proposed by this study, it is not recommended to capture images of *E. radiata* with cloud cover present. One possible solution could be the use of polarising filters to remove sun glint in future (Joyce et al. 2019; Mount 2005). This method was not explored, and it is worth investigating the ability of polarising filters to remove sun glint without compromising *E. radiata*'s spectral properties in shallow water. Based on the findings from this study it is also recommended to further explore the use of nadir images over intertidal zones. This is because nadir images that are captured, even during mid-day in bright sunlight over very shallow water, have very little sun glint issues. The shallow water sun glint issues encountered in the study was easily resolved at the classification stage by increasing the segment size, for the purpose of *E. radiata* classification. The proposed method of individual image capture in very shallow water, can be carried out using both oblique and nadir images. In shallow water environments nadir images can be captured at high sun altitude angles. Nadir images over shallow water is usually recommended due to geometry issues in oblique imagery (Joyce et al. 2019). Therefore, nadir imagery in very shallow water with high sun altitude angles are worth further exploration to increase the potential time frame to capture imagery over water. It is also recommended to use sensors with larger bit depth and exposure control to allow for better correction of illumination change in oblique imagery.

A confusion matrix method of data validation could be implemented in the intertidal zone of the study area with the improvement of the method used in this research. This improvement could not be made due to time constraints in this study. However, it could be done by laying out all the transect lines in bright colours, across the water in rockpools, with 0.5m marks on the transect where point data can be collected, and then capturing an UAV image of all the transect lines shortly before or after data collection.

At the very early exploratory stages of this research topic, UAV video data was collected at varying heights above Aldinga reef. On visual assessment, the videos showed that movement of *E. radiata* fronds with the action of waves, especially in the subtidal zone, distinguishes it from the rest of the aquatic vegetation. This area was not further explored due to the long timeframe that it takes to incorporate the learning curve required for such a project. However, it is worth further exploring the possibility of identifying *E. radiata* using video analysis and video classification methods with

machine learning methods as they are used successfully in some types of benthic mapping (Edgington et al, 2006)

To carry out accurate water column correction, to improve the accuracy of *E. radiata* mapping using UAV images, a high-quality bathymetry dataset is needed. Therefore, such a bathymetry dataset will be useful for future research.

As the research findings showed, the accuracy of *E. radiata* detection is high in very shallow water environments, such as in shallow rock pools, intertidal zones, and shallow subtidal zones below 2 m depth. This provides an opportunity to use the method to estimate the percentage of *E. radiata* in those shallow environments, which are often important areas for monitoring Marine Parks and areas of importance such as the Great Southern Reef. Individual images or small patches of overlapping images can be used as a sampling strategy that can cover larger spatial extents than field data collection in a shorter timeframe. This may be useful for understanding the spatial variation in the distribution of *E. radiata* in shallow reef areas. Thus, the method can allow for the merging of field data sampling and remote sensing methods, in a similar way that underwater photography and videos are used for diver data collection as validation.

7 REFERENCE LIST

Aerometrix Metromap 2021, Metromap, accessed June 2021, < <https://metromap.com.au/>>

Agrafiotis, P, Skarlatos, D, Georgopoulos, A & Karantzalos, K 2019, 'Shallow Water Bathymetry Mapping from UAV Imagery Based on Machine Learning', *ISPRS Annals of the Photogrammetry, Remote Sensing and Spatial Information Sciences*, vol. 42, no. 2, pp. 9-16.

Akerman, K 2005, 'Shoes of Invisibility and Invisible Shoes: Australian Hunters and Gatherers and Ideas on the Origins of Footwear', *Australian Aboriginal Studies*, vol. 2005, no. 2, pp. 55-64.

ALA 2021, *Ecklonia radiata* (C.Agardh.) J.Agardh - Golden Kelp, Atlas of Living Australia (ALA), viewed 14 November 2021 2021, <<https://bie.ala.org.au/species/NZOR-6-5237>>.

Anderson, K & Gaston, KJ 2013, 'Lightweight unmanned aerial vehicles will revolutionize spatial ecology', *Frontiers in ecology and the environment*, vol. 11, no. 3, pp. 138-46.

Ashraf, S, Brabyn, L & Hicks, BJ 2012, 'Image data fusion for the remote sensing of freshwater environments', *Applied Geography*, vol. 32, no. 2, pp. 619-28.

Bennett, S, Wernberg, T, Connell, SD, Hobday, AJ, Johnson, CR & Poloczanska, ES 2016a, 'The 'Great Southern Reef': social, ecological and economic value of Australia's neglected kelp forests', *Marine and freshwater research*, vol. 67, no. 1, p. 47.

— 2016b, 'The 'Great Southern Reef': Social, ecological and economic value of Australia's neglected kelp forests', *Marine and freshwater research*, vol. 67, no. 1, pp. 47-56.

Blaschke, T 2010, 'Object based image analysis for remote sensing', *ISPRS Journal of Photogrammetry and Remote Sensing*, vol. 65, no. 1, pp. 2-16.

Blaschke, T & Strobl, J 2001, 'What's wrong with pixels? Some recent developments interfacing remote sensing and GIS', *GIS – Zeitschrift für Geoinformationssysteme*, vol. 14, pp. 12-7.

Bolton, JJ 2016, 'What is aquatic botany?— And why algae are plants: The importance of non-taxonomic terms for groups of organisms', *Aquatic botany*, vol. 132, pp. 1-4.

Bolton, JJ & Anderson, RJ 1987, 'Temperature tolerances of two southern African *Ecklonia* species (Alariaceae: Laminariales) and of hybrids between them', *Marine biology*, vol. 96, no. 2, pp. 293-7.

BOM 2021, *Greater Adelaide in winter 2021: Warm days and nights, above average rainfall*, Australian Government - Bureau of Meteorology, viewed 15 November 2021 2021, <<http://www.bom.gov.au/climate/current/season/sa/adelaide.shtml>>.

Brook, J, Peters, K, Bryars, S, Owen, S, Hicks, J, Miller, D, Easton, D, Eglinton, Y, Meakin, C & Brock, D 2020, *Subtidal Reef Health Program: Baseline status of subtidal reefs and associated biodiversity patterns in the AMLR*, Adelaide.

Brown, CJ, Smith, SJ, Lawton, P & Anderson, JT 2011, 'Benthic habitat mapping: A review of progress towards improved understanding of the spatial ecology of the seafloor using acoustic techniques', *Estuarine, coastal and shelf science*, vol. 92, no. 3, pp. 502-20.

Bryson, M, Duce, S, Harris, D, Webster, JM, Thompson, A, Vila-Concejo, A & Williams, SB 2016, 'Geomorphic changes of a coral shingle cay measured using Kite Aerial Photography', *Geomorphology*, vol. 270, pp. 1-8.

Casal, G, Sánchez-Carnero, N, Domínguez-Gómez, JA, Kutser, T & Freire, J 2012, 'Assessment of AHS (Airborne Hyperspectral Scanner) sensor to map macroalgal communities on the Ría de vigo and Ría de Aldán coast (NW Spain)', *Marine biology*, vol. 159, no. 9, pp. 1997-2013.

Chao Rodríguez, Y, Domínguez Gómez, JA, Sánchez-Carnero, N & Rodríguez-Pérez, D 2017, 'A comparison of spectral macroalgae taxa separability methods using an extensive spectral library', *Algal Research*, vol. 26, pp. 463-73.

Cherian, A.K., Poovammal, E., Philip, N.S., Ramana, K., Singh, S., Ra, I.-H. 2021 *Deep Learning Based Filtering Algorithm for Noise Removal in Underwater Images*, *Water* 2021, 13, 2742, viewed 25 November 2021, < <https://doi.org/10.3390/w13192742>>

Cheshire, AC & Westphalen, G 2000, 'Assessing the status of reefs in Gulf St Vincent IV: Results of the 1999 survey. A report to the Environment Protection Agency of South Australia'.

Clarke, PA 2011, *Aboriginal People and their Plants*, Dural, NSW: Rosenberg Publishing, Dural, NSW.

Clarke, TM, Whitmarsh, SK, Fairweather, PG & Huveneers, C 2019, 'Overlap in fish assemblages observed using pelagic and benthic baited remote underwater video stations', *Marine and freshwater research*, vol. 70, no. 6, p. 870.

Coleman, MA 2013, 'Connectivity of the Habitat-Forming Kelp, *Ecklonia radiata* within and among Estuaries and Open Coast. e64667', *PLoS ONE*, vol. 8, no. 5.

Coleman, MA & Wernberg, T 2018, 'Genetic and morphological diversity in sympatric kelps with contrasting reproductive strategies', *Aquatic biology*, vol. 27, pp. 65-73.

Connell, S 2007, 'Water quality and the loss of coral reefs and kelp forests: alternative states and the influence of fishing', in S Connell & B Gillanders (eds), *Marine Ecology*, Oxford University Press, Melbourne, pp. 556-68.

Connell, SD 2005, 'Assembly and maintenance of subtidal habitat heterogeneity: synergistic effects of light penetration and sedimentation', *Marine ecology. Progress series (Halstenbek)*, vol. 289, pp. 53-61.

Connell, SD & Irving, AD 2008, 'Integrating ecology with biogeography using landscape characteristics: a case study of subtidal habitat across continental Australia', *Journal of biogeography*, vol. 35, no. 9, pp. 1608-21.

Connell, SD, Russell, BD, Turner, DJ, Shepherd, SA, Kildea, T, Miller, D, Airoidi, L & Cheshire, A 2008, 'Recovering a lost baseline: missing kelp forests from a metropolitan coast', *Marine ecology. Progress series (Halstenbek)*, vol. 360, pp. 63-72.

Cox, C & Munk, W 1954, 'Measurement of the Roughness of the Sea Surface from Photographs of the Sun's Glitter', *Journal of the Optical Society of America*, vol. 44, no. 11, pp. 838-50.

Davies-Colley, RJ, Ballantine, DJ, Elliott, SH, Swales, A, Hughes, AO & Gall, MP 2014, 'Light attenuation - A more effective basis for the management of fine suspended sediment than mass concentration?', *Water Sci Technol*, vol. 69, no. 9, pp. 1867-74.

DENR 2010, *Environmental, Economic and Social Values of the Encounter Marine Park*, Department of Environment and Natural Resources, South Australia.

DEW 2019, *Stormwater Drains*, Data.SA-South Australian Government Data Directory, Australia, <<https://data.sa.gov.au/data/dataset/stormwater-drains/resource/e8c09825-c621-4ac8-b300-f07386fac826>>.

DJI 2018a, *DJI GS Pro*, V2.0 2018.11 edn, Shenzhen Dajiang Baiwang Technology Co., Ltd, China.

— 2018b, *Mavic 2 PRO camera sensor physical dimensions*, 2018-9-20, <<https://forum.dji.com/thread-167017-1-1.html>>.

— 2019, *Mavic 2 Pro/Zoom User Manual v2.0*, vol. v2.0, Shenzhen Dajiang Baiwang Technology Co., Ltd.

— 2021a, *Mavic 2 Enterprise Series - Specs*, Shenzhen Dajiang Baiwang Technology Co., Ltd, <<https://www.dji.com/au/mavic-2-enterprise/specs>>.

— 2021b, *Mavic 2 Pro Specs*, Shenzhen Dajiang Baiwang Technology Co., Ltd, viewed 18/11/2021, <<https://www.dji.com/au/mavic-2/info>>.

Durrant, HMS, Barrett, NS, Edgar, GJ, Coleman, MA & Burrridge, CP 2015, 'Shallow phylogeographic histories of key species in a biodiversity hotspot', *Phycologia (Oxford)*, vol. 54, no. 6, pp. 556-65.

Edgington, D., Cline, D., Davis, D., Kerkez, I., & Mariette, J. 2006, 'Detecting, Tracking and Classifying Animals in Underwater Video'. OCEANS 2006, pp.1-5, viewed 25 November 2021, <<https://ieeexplore-ieee-org.ezproxy.flinders.edu.au/stamp/stamp.jsp?tp=&arnumber=4099033>>

Edyvane, K 2008, 'Macroalgal Biogeography and Assemblages of Gulf St Vincent', *Natural history of Gulf St Vincent*, pp. 248-63.

EPA 1998, *Changes in Seagrass Cover and Links to Water Quality off the Adelaide Metropolitan Coastline*, South Australia.

Esri 2021a, *ArcGIS Pro*, 2.8.0, computer software, Environmental Systems Research Institute (Esri) Inc, United States

— 2021b, *Raster compression*, Environmental Systems Research Institute (Esri) Inc, United States, viewed 24 November 2021, <<https://desktop.arcgis.com/en/arcmap/10.3/manage-data/raster-and-images/raster-compression.htm>>

— 2021c, *Resample (Data Management)*, Environmental Systems Research Institute (Esri) Inc, United States, viewed 24 November 2021, < <https://pro.arcgis.com/en/pro-app/latest/tool-reference/data-management/resample.htm> >

Fairhead, VA 2002, 'Ecophysiology and production ecology of the kelp *Ecklonia radiata* (C.Agardh) J.Agardh, at West Island, South Australia', PhD thesis, University of Adelaide.

Fairhead, VA & Cheshire, AC 2004a, 'Rates of primary productivity and growth in *Ecklonia radiata* measured at different depths, over an annual cycle, at West Island, South Australia', *Marine biology*, vol. 145, no. 1, pp. 41-50.

— 2004b, 'Seasonal and depth related variation in the photosynthesis–irradiance response of *Ecklonia radiata* (Phaeophyta, Laminariales) at West Island, South Australia', *Marine biology*, vol. 145, no. 2, pp. 415-26.

Filbee-Dexter, K, Wernberg, T, Fredriksen, S, Norderhaug, KM & Pedersen, MF 2019, 'Arctic kelp forests: Diversity, resilience and future', *Global and Planetary Change*, vol. 172, pp. 1-14.

Flynn, KF & Chapra, SC 2014, 'Remote Sensing of Submerged Aquatic Vegetation in a Shallow Non-Turbid River Using an Unmanned Aerial Vehicle', *Remote Sensing*, vol. 6, no. 12.

Foody, GM 2002, 'Status of land cover classification accuracy assessment', *Remote sensing of environment*, vol. 80, no. 1, pp. 185-201.

Fyfe, SK 2003, 'Spatial and temporal variation in spectral reflectance: Are seagrass species spectrally distinct?', *Limnology and Oceanography*, vol. 48, no. 1 part 2, pp. 464 - 79.

Gallegos, CL & Moore, KA 2000, *Factors contributing to water-column light attenuation*, EPA Chesapeake Bay Program.

Garcia, R, Hedley, J, Tin, H & Fearn, P 2015, 'A Method to Analyze the Potential of Optical Remote Sensing for Benthic Habitat Mapping', *Remote sensing (Basel, Switzerland)*, vol. 7, no. 10, pp. 13157-89.

GARMIN 2021, *GPS Accuracy*, GARMIN, viewed 19 November 2021, <<https://support.garmin.com/en-AU/marine/faq/aZc8RezeAb9LjCDpJplTY7/>>.

Gorman, D & Connell, SD 2009, 'Recovering Subtidal Forests in Human-Dominated Landscapes', *The Journal of applied ecology*, vol. 46, no. 6, pp. 1258-65.

Green, E, Mumby, P, Edwards, A & Clark, C 2000, *Remote Sensing Handbook for Tropical Coastal Management*.

Harman, N, Harvey, ES & Kendrick, GA 2003, 'Differences in fish assemblages from different reef habitats at Hamelin Bay, south-western Australia', *Marine and freshwater research*, vol. 54, no. 2, pp. 177-84.

Harrer, SL, Reed, DC, Holbrook, SJ & Miller, RJ 2013, 'Patterns and controls of the dynamics of net primary production by understory macroalgal assemblages in giant kelp forests', *J. Phycol*, vol. 49, no. 2, pp. 248-57.

Harris, P & Baker, E 2012, *Seafloor geomorphology as benthic habitat GeoHAB atlas of seafloor geomorphic features and benthic habitats*, 1st ed., Elsevier insights, London: Elsevier.

Harvey, M, J. 2009, 'Development of Techniques to Classify Marine Benthic Habitats Using Hyperspectral Imagery in Oligotrophic, Temperate Waters', Doctor of Philosophy thesis, Murdoch University.

Hedley, J, Roelfsema, C, Chollett, I, Harborne, A, Heron, S, Weeks, S, Skirving, W, Strong, A, Eakin, C, Christensen, T, Ticzon, V, Bejarano, S & Mumby, P 2016, 'Remote Sensing of Coral Reefs for Monitoring and Management: A Review', *Remote sensing (Basel, Switzerland)*, vol. 8, no. 2, p. 118.

Hedley, JD, Harborne, AR & Mumby, PJ 2005, 'Technical note: Simple and robust removal of sun glint for mapping shallow-water benthos', *International journal of remote sensing*, vol. 26, no. 10, pp. 2107-12.

Hedley, JD, Roelfsema, CM, Phinn, SR & Mumby, PJ 2012, 'Environmental and Sensor Limitations in Optical Remote Sensing of Coral Reefs: Implications for Monitoring and Sensor Design', *Remote Sensing*, vol. 4, no. 1.

Hemerly, EM 2014, 'Automatic Georeferencing of Images Acquired by UAV's', *International Journal of Automation and computing*, vol. 11, no. 4, pp. 347-52.

Hochberg, EJ, Andrefouet, S & Tyler, MR 2003, 'Sea surface correction of high spatial resolution Ikonos images to improve bottom mapping in near-shore environments', *IEEE Transactions on Geoscience and Remote Sensing*, vol. 41, no. 7, pp. 1724-9.

Hughes, M., 2016, Coastal waves, water levels, beach dynamics and climate change. CoastAdapt, National Climate Change Adaptation Research Facility, Gold Coast.<
https://coastadapt.com.au/sites/default/files/factsheets/T3I4_Coastal_waves.pdf>

Jackson, C, Salomaki, ED, Lane, CE & Saunders, GW 2017, 'Kelp transcriptomes provide robust support for interfamilial relationships and revision of the little known Arthrothamnaceae (Laminariales)', *J Phycol*, vol. 53, no. 1, pp. 1-6.

Jensen, JR 2015, *Introductory Digital Image Processing: A Remote Sensing Perspective*, Old Tappan: Pearson Education, Old Tappan.

Jo, T 2021, *Machine learning foundations : supervised, unsupervised, and advanced learning*, 1st ed. 2021. edn, Cham, Switzerland : Springer.

Joyce, KE, Duce, S, Leahy, SM, Leon, J & Maier, SW 2019, 'Principles and practice of acquiring drone-based image data in marine environments', *Marine and freshwater research*, vol. 70, no. 7, pp. 952-63.

Kay, S, Hedley, JD & Lavender, S 2009, 'Sun Glint Correction of High and Low Spatial Resolution Images of Aquatic Scenes: a Review of Methods for Visible and Near-Infrared Wavelengths', *Remote Sensing*, vol. 1, no. 4.

Kennelly, SJ 1987a, 'Inhibition of kelp recruitment by turfing algae and consequences for an Australian kelp community', *Journal of experimental marine biology and ecology*, vol. 112, no. 1, pp. 49-60.

Kennelly, SJ 1987b, 'Physical disturbances in an Australian kelp community. I. Temporal effects', *Marine ecology. Progress series (Halstenbek)*, vol. 40, no. 1/2, pp. 145-53.

Kutser, T, Hedley, J, Giardino, C, Roelfsema, C & Brando, VE 2020, 'Remote sensing of shallow waters – A 50 year retrospective and future directions', *Remote sensing of environment*, vol. 240, p. 111619.

Kutser, T, Vahtmäe, E & Praks, J 2009, 'A sun glint correction method for hyperspectral imagery containing areas with non-negligible water leaving NIR signal', *Remote sensing of environment*, vol. 113, no. 10, pp. 2267-74.

Larkum, AWD & Wood, WF 1993, 'The effect of UV-B radiation on photosynthesis and respiration of phytoplankton, benthic macroalgae and seagrasses', *Photosynth Res*, vol. 36, no. 1, pp. 17-23.

Layton, C, Coleman, MA, Marzinelli, EM, Steinberg, PD, Swearer, SE, Verges, A, Wernberg, T & Johnson, CR 2020, 'Kelp Forest Restoration in Australia', *Frontiers in Marine Science*, vol. 7.

Li, C & Guo, J 2015, 'Underwater image enhancement by dehazing and color correction', *Journal of Electronic Imaging* 24(3), 033023, viewed 25 November 2021 <<https://doi.org/10.1117/1.JEI.24.3.033023>>

Lu, D & Weng, Q 2007, 'A survey of image classification methods and techniques for improving classification performance', *International journal of remote sensing*, vol. 28, no. 5, pp. 823-70.

Mabin, CJT, Gribben, PE, Fischer, A & Wright, JT 2013, 'Variation in the morphology, reproduction and development of the habitat-forming kelp *Ecklonia radiata* with changing temperature and nutrients', *Marine ecology. Progress series (Halstenbek)*, vol. 483, pp. 117-31.

Mahesh, B 2020, 'Machine Learning Algorithms - A review', *International Journal of Science and Research (IJSR)*, vol. 9, no. 1, pp. 381-6.

Marzinelli, EM, Williams, SB, Babcock, RC, Barrett, NS, Johnson, CR, Jordan, A, Kendrick, GA, Pizarro, OR, Smale, DA & Steinberg, PD 2015, 'Large-scale geographic variation in distribution and abundance of Australian deep-water kelp forests', *PLoS ONE*, vol. 10, no. 2, pp. e0118390-e.

McDowell, L-M, Green, D & Griffante, D 2009, *Adelaide Coastal Waters Information Sheet No. 4*, Environmental Protection Agency (EPA), Australia, <https://www.epa.sa.gov.au/files/477425_acws_physical.pdf>.

Mohring, MB, Wernberg, T, Kendrick, GA & Rule, MJ 2012, 'Reproductive synchrony in a habitat-forming kelp and its relationship with environmental conditions', *Marine biology*, vol. 160, no. 1, pp. 119-26.

Mohring, MB, Wernberg, T, Wright, JT, Connell, SD & Russell, BD 2014, 'Biogeographic variation in temperature drives performance of kelp gametophytes during warming', *Marine ecology. Progress series (Halstenbek)*, vol. 513, pp. 85-96.

Mount, R 2005, 'Acquisition of through-water aerial survey images: Surface effects and the prediction of sun glitter and subsurface illumination', *Photogrammetric Engineering and Remote Sensing*, vol. 71, no. 12, pp. 1407-15.

Mumby, PJ, Clark, CD, Green, EP & Edwards, AJ 1998, 'Benefits of water column correction and contextual editing for mapping coral reefs', *International journal of remote sensing*, vol. 19, no. 1, pp. 203-10.

Murfitt, SL, Allan, BM, Bellgrove, A, Rattray, A, Young, MA & Ierodiaconou, D 2017, 'Applications of unmanned aerial vehicles in intertidal reef monitoring', *Sci Rep*, vol. 7, no. 1, pp. 10259-.

Mustard, JF, Staid, MI & Fripp, WJ 2001, 'A Semianalytical Approach to the Calibration of AVIRIS Data to Reflectance over Water: Application in a Temperate Estuary', *Remote sensing of environment*, vol. 75, no. 3, pp. 335-49.

NatureMaps 2021, *NatureMaps Coastal Monitoring Profile Line #200054*, Australia, <<http://spatialwebapps.environment.sa.gov.au/naturemaps/?locale=en-us&viewer=naturemaps>>.

Nelson, W, Duffy, C, Trnski, T & Stewart, R 2018, 'Mesophotic *Ecklonia radiata* (Laminariales) at Rangitāhua, Kermadec Islands, New Zealand', *Phycologia (Oxford)*, vol. 57, no. 5, pp. 534-8.

NPSA 2016, *SA Marine Parks Sanctuary Zone Maps*, National Parks South Australia (NPSA), viewed 24 November 2021, <<https://cdn.environment.sa.gov.au/marine-parks/docs/sa-marine-parks-sz-maps-update-2016.pdf>>

Orych, A., Walczykowski, P., Jenerowicz, A., & Zdunek, Z. 2014, 'Impact of the Camera Radiometric Resolution on the Accuracy of Determining Spectral Reflectance Coefficients', *The International Archives of the Photogrammetry, Remote Sensing and Spatial Information Sciences*, Volume XL-1, 2014 ISPRS Technical Commission I Symposium, 17 – 20 November 2014, Denver, Colorado, USA, pp 347-349

Pix4D 2018, [*iOS*] *Pix4Dcapture and Parrot Sequoia captures less overlap with custom camera settings*, Pix4D, May 2018, <<https://community.pix4d.com/t/ios-pix4dcapture-and-parrot-sequoia-captures-less-overlap-with-custom-camera-settings/6579/2>>.

— 2021, *Learn more about Sequoia+*, Pix4D SA, viewed 18/11/2021 2021, <<https://www.pix4d.com/product/sequoia/faq>>.

Pope, R.M & Fry, E.S 1997, 'Absorption spectrum (380–700 nm) of pure water. II. Integrating cavity measurements,' *Appl. Opt.* 36, pp.8710-8723, accessed 22 November 2021, <<https://www.osapublishing.org/ao/fulltext.cfm?uri=ao-36-33-8710&id=63107>>

Rand, AM 2006, 'Using Geographic Information Systems and remote sensing to improve the management of kelp resources in South Africa', University of Cape Town.

Riniatsih, I, Ambariyanto, A, Yudiati, E, Redjeki, S & Hartati, R 2021, 'Monitoring the seagrass ecosystem using the unmanned aerial vehicle (UAV) in coastal water of Jepara', *IOP conference series. Earth and environmental science*, vol. 674, no. 1, p. 12075.

Roelfsema, C, Kovacs, E, Ortiz, JC, Wolff, NH, Callaghan, D, Wettle, M, Ronan, M, Hamylton, SM, Mumby, PJ & Phinn, S 2018a, 'Coral reef habitat mapping: A combination of object-based image analysis and ecological modelling', *Remote sensing of environment*, vol. 208, pp. 27-41.

Roelfsema, C, Kovacs, E, Roos, P, Terzano, D, Lyons, MI & Phinn, S 2018b, 'Use of a semi-automated object based analysis to map benthic composition, Heron Reef, Southern Great Barrier Reef', *Remote Sensing Letters*, vol. 9, no. 4, pp. 324-33.

Roelfsema, CM, Lyons, M, Kovacs, EM, Maxwell, P, Saunders, MI, Samper-Villarreal, J & Phinn, SR 2014, 'Multi-temporal mapping of seagrass cover, species and biomass: A semi-automated object based image analysis approach', *Remote sensing of environment*, vol. 150, pp. 172-87.

- Rothman, MD, Mattio, L, Wernberg, T, Anderson, RJ, Uwai, S, Mohring, MB & Bolton, JJ 2015, 'A molecular investigation of the genus *Ecklonia* (Phaeophyceae, Laminariales) with special focus on the Southern Hemisphere', *J. Phycol*, vol. 51, no. 2, pp. 236-46.
- Sanderson, JC 1990, 'A Preliminary Survey of the Distribution of the Introduced Macroalga, *Undaria pinnatifida* (Harvey) Suringer on the East Coast of Tasmania, Australia', vol. 33, no. 2, pp. 153-8.
- Schiel, DR & Choat, JH 1980, 'Effects of density on monospecific stands of marine algae', *Nature (London)*, vol. 285, no. 5763, pp. 324-6.
- Schläpfer, D, Popp, C & Richter, R 2020, 'Drone Data Atmospheric Correction Concept for Multi- and Hyperspectral Imagery – The Droacor Model', *ISPRS - International Archives of the Photogrammetry, Remote Sensing and Spatial Information Sciences*, vol. XLIII-B3-2020, pp. 473-8.
- Selvaraj, S 2021, 'Development of Novel Image Analysis Approaches for Seaweed Discrimination – Species Level Study Using Field Spectroscopy and UAV Multispectral Remote Sensing', PhD thesis, Auckland University of Technology.
- Selvaraj, S, Case, BS & White, WL 2021, 'Effects of Location and Season on Seaweed Spectral Signatures', *Frontiers in ecology and evolution*, vol. 9.
- Shan, S, Hannah, CG & Wu, Y 2020, 'Response of sea level to tide, atmospheric pressure, wind forcing and river discharge in the Kitimat Fjord System', *Estuarine, coastal and shelf science*, vol. 246.
- Shepherd, JD, Dymond, JR, Gillingham, S & Bunting, P 2014, 'Accurate registration of optical satellite imagery with elevation models for topographic correction', *Remote Sensing Letters*, vol. 5, no. 7, pp. 637-41.
- Short, A.D., 2020. *Australian Coastal Systems Beaches, Barriers and Sediment Compartments* 1st ed. 2020., Springer International Publishing : Imprint: Springer
- Silberfeld, T, Leigh, JW, Verbruggen, H, Cruaud, C, de Reviers, B & Rousseau, F 2010, 'A multi-locus time-calibrated phylogeny of the brown algae (Heterokonta, Ochrophyta, Phaeophyceae): Investigating the evolutionary nature of the “brown algal crown radiation”', *Mol Phylogenet Evol*, vol. 56, no. 2, pp. 659-74.
- Staehr, PA & Wernberg, T 2009, 'Physiological Responses of *Ecklonia Radiata* (Laminariales) to a Latitudinal Gradient in Ocean Temperature', *J Phycol*, vol. 45, no. 1, pp. 91-9.
- Tait, L, Bind, J, Charan-Dixon, H, Hawes, I, Pirker, J & Schiel, D 2019, 'Unmanned Aerial Vehicles (UAVs) for Monitoring Macroalgal Biodiversity: Comparison of RGB and Multispectral Imaging Sensors for Biodiversity Assessments', *Remote Sensing*, vol. 11, no. 19.

Tait, LW, Orchard, S & Schiel, DR 2021, 'Missing the forest and the trees: Utility, limits and caveats for drone imaging of coastal marine ecosystems', *Remote sensing (Basel, Switzerland)*, vol. 13, no. 16, p. 3136.

Tait, LW & Schiel, DR 2018, 'Ecophysiology of Layered Macroalgal Assemblages: Importance of Subcanopy Species Biodiversity in Buffering Primary Production', *Frontiers in Marine Science*.

Tatsumi, M & Wright, JT 2016, 'Understory algae and low light reduce recruitment of the habitat-forming kelp *Ecklonia radiata*', *Marine ecology. Progress series (Halstenbek)*, vol. 552, pp. 131-43.

Tin, HC, O' Leary, M, Fotedar, R & Garcia, R 2015, 'Spectral response of marine submerged aquatic vegetation: A case study in Western Australia coast', in *OCEANS 2015 - MTS/IEEE Washington*, pp. 1-5.

Turner, D, Lucieer, A & Wallace, L 2014, 'Direct Georeferencing of Ultrahigh-Resolution UAV Imagery', *IEEE Transactions on Geoscience and Remote Sensing*, vol. 52, no. 5, pp. 2738-45.

Turner, DJ 2004, 'Effect of sedimentation on the structure of a phaeophycean dominated macroalgal community', PhD thesis, The University Of Adelaide.

Turner, DJ, Kildea, TN & Westphalen, G 2007, *Examining the health of subtidal reef environments in South Australia, Part 2: Status of selected South Australian reefs based on the results of the 2005 surveys*, South Australian Research and Development Institute (Aquatic Sciences), South Australia.

Uhl, F, Oppelt, N & Bartsch, I 2013, 'Spectral mixture of intertidal marine macroalgae around the island of Helgoland (Germany, North Sea)', *Aquatic botany*, vol. 111, pp. 112-24.

Underwood, AJ 2000, 'Experimental ecology of rocky intertidal habitats: what are we learning?', *J Exp Mar Bio Ecol*, vol. 250, no. 1, pp. 51-76.

Vergés, A, Doropoulos, C, Malcolm, HA, Skye, M, Garcia-Pizá, M, Marzinelli, EM, Campbell, AH, Ballesteros, E, Hoey, AS, Vila-Concejo, A, Bozec, Y-M & Steinberg, PD 2016, 'Long-term empirical evidence of ocean warming leading to tropicalization of fish communities, increased herbivory, and loss of kelp', *Proc Natl Acad Sci U S A*, vol. 113, no. 48, pp. 13791-6.

Wegener, J, E. 1995, 'The Relationship Between Sedimentation on Aldinga Reef, and Washpool Creek and Sellicks Creek Catchments, Willunga Basin', Bachelor of Arts with Honours in Geography thesis, University of Adelaide.

Wernberg, T 2005, 'Holdfast aggregation in relation to morphology, age, attachment and drag for the kelp *Ecklonia radiata*', *Aquatic botany*, vol. 82, no. 3, pp. 168-80.

Wernberg, T, Bennett, S, Babcock, R, de Bettignies, T, Cure, K, Depczynski, M, Dufois, F, Fromont, J, Fulton, C, Hovey, R, Harvey, E, Holmes, T, Kendrick, G, Radford, B, Santana Garcon, J,

Saunders, B, Smale, D, Thomsen, M, Tuckett, C, Tuya, F, Vanderklift, M & Wilson, S 2016, 'Climate-driven regime shift of a temperate marine ecosystem', *Science*, vol 353, no 6295, pp. 169-172

Wernberg, T, Coleman, MA, Babcock, RC, Bell, SY, Bolton, JJ, Connell, SD, Hurd, CL, Johnson, CR, Marzinelli, EM, Shears, NT, Steinberg, PD, Thomsen, MS, Vanderklift, MA, Vergés, A & Wright, JT 2019a, *Biology and Ecology of the Globally Significant Kelp Ecklonia radiata*, 1 edn, CRC Press.

——— 2019b, 'Biology and Ecology of the Globally Significant Kelp *Ecklonia radiata*', *Oceanography and Marine Biology: An Annual Review*, vol. 57, pp. 265-323.

Wernberg, T & Connell, SD 2008, 'Physical disturbance and subtidal habitat structure on open rocky coasts: Effects of wave exposure, extent and intensity', *Journal of sea research*, vol. 59, no. 4, pp. 237-48.

Wernberg, T, de Bettignies, T, Joy, BA & Finnegan, PM 2016b, 'Physiological responses of habitat-forming seaweeds to increasing temperatures', *Limnol. Oceanogr*, vol. 61, no. 6, pp. 2180-90.

Wernberg, T, Kendrick, GA & Phillips, JC 2003, 'Regional differences in kelp-associated algal assemblages on temperate limestone reefs in south-western Australia', *Diversity & distributions*, vol. 9, no. 6, pp. 427-41.

Wernberg, T, Thomsen, MS, Tuya, F, Kendrick, GA, Staehr, PA & Toohey, BD 2010, 'Decreasing resilience of kelp beds along a latitudinal temperature gradient: potential implications for a warmer future', *Ecol Lett*, vol. 13, no. 6, pp. 685-94.

Wessen, S 2009, *Murni, Dhungang, Jirrar: living in the Illawarra*, Department of Environment and Conservation (NSW), <<https://www.heritage.nsw.gov.au/search-for-heritage/publications-and-resources/aboriginal-cultural-heritage-publications/>>Western, M, Hesp, P, Bourman, R & Miot Da Silva, G 2020a, 'Coastal Adaptation Study for City of Onkaparinga, Integrated Coasts, South Australia', viewed 14 December 2021, <<https://yoursay.onkaparinga.sa.gov.au/coastal-adaptation-study>>.

———2020b, 'Coastal Adaptation Study for City of Onkaparinga, Integrated Coasts, South Australia, Cell 10, Aldinga Reef', viewed 20 November 2021, <<https://yoursay.onkaparinga.sa.gov.au/coastal-adaptation-study>>.

Wicaksono, P & Lazuardi, W 2018, 'Assessment of PlanetScope images for benthic habitat and seagrass species mapping in a complex optically shallow water environment', *International journal of remote sensing*, vol. 39, no. 17, pp. 5739-65.

Womersley, HBS 1984, *The marine benthic flora of Southern Australia*, Adelaide : Government Printer, Adelaide.

8 APPENDICES

8.1 Permits and certificates

8.1.1 Marine Parks Permit to Undertake Scientific Research



Government of South Australia
Department for Environment
and Water

Scientific research is encouraged in South Australia's marine parks. It is only through increased scientific understanding that we can develop robust conservation management. Your research should be conducted to have the smallest possible impact on the marine environment.

MARINE PARKS PERMIT TO UNDERTAKE SCIENTIFIC RESEARCH

Permit issued pursuant to

Marine Parks Act 2007, section 19
Marine Parks (Zoning) Regulations 2012

Permit number MR00177-1

Permit holder Ms Basma Abdul Muhsin
Flinders University, College of Science & Engineering
Sturt Road
Bedford Park, SA 5042

Project title The use of drone multispectral imagery to map and understand the distribution of *Ecklonia Radiata* at Aldinga Reef

Activities authorised by this permit

1. Conducting scientific research for commercial or professional purposes in nominated marine park sanctuary zones

Duration This permit is valid from one year from date of issue (unless cancelled or revoked).

Location Encounter Marine Park, sanctuary zone 3 Aldinga Reef

Enquiries contact details

For any enquiries relating to this permit, contact:

Department for Environment and Water
Marine Parks Unit
Postal address: GPO Box 1047, Adelaide SA 5001
Email: DEW.MarineParksPermits@sa.gov.au

Permit conditions

This permit is issued subject to the following conditions. Failure to adhere to the conditions constitutes a breach which can result in revocation of the permit and potential prosecution. The Permit Holder must not contravene or fail to comply with the *Marine Parks Act 2007* or any regulations made under that Act, except where specifically provided for by this permit.

Obligations

1. The Permit Holder and all persons associated with the activity authorised by this permit must:
 - 1.1 take all reasonable measures to prevent or minimise harm to a marine park through their actions or activities;
 - 1.2 have the permit in their possession when undertaking the authorised activity;
 - 1.3 notify DEW within fourteen days of any changes to contact, address or business details during the term of this permit;
 - 1.4 for the term of this permit, hold and maintain insurance for public liability for not less than \$10 million in respect of any one claim arising out of the activities of the insured, covering all third party claims arising out of loss, destruction or damage to real or personal property and ensuing loss of that property and death or injury to persons. The permit holder shall, whenever requested by the relevant authority, produce evidence of the currency of such insurance.
2. The Permit Holder is responsible for the actions of other persons who may undertake this research or collect specimens on their behalf.
3. The Permit Holder and all persons associated with the permitted activity must comply with all other legislation, regulations, by-laws, codes of practice or similar applicable to the activity or the area in which it is undertaken.

Activity

4. No specimens, dead or alive, are to be removed from marine park sanctuary zones
5. The drone must avoid disturbance of any possible marine mammals or birds. If, during survey runs, any mammals or birds enter the area the drone must be flown away until the mammal or bird has left the area.
6. Avoid anchoring on reefs, seagrass beds or other sensitive habitats where possible.
7. Ensure best practice diving techniques (fin usage, buoyancy control, secure gear and equipment) are used to minimise impact and disturbance to habitats and fauna

Reporting and liaison

8. The relevant marine parks Regional Coordinator(s) must be notified at least 10 days prior to any research being undertaken in their region(s).

Adelaide & Mount Lofty Ranges Jon Emmett; jon.emmett@sa.gov.au; ph. 0428 106 412
9. The Principal, Marine Science, DEW, must be notified at least 5 days prior to commencement of any fieldwork operations in marine parks (Simon Bryars; ph. (08) 8124 4788, simon.bryars@sa.gov.au).

10. Within 60 days of the expiration of this permit, the Delegate or the Principal, Marine Science, DEW, must be provided with a completed Marine Parks Research Permit Activity Log.
11. Raw data and/or results (including data obtained as a result of laboratory analysis or satellite or acoustic tracking) derived from the activities authorised by this Permit must be made available to DEW on request at any time during or following the completion of those activities.
12. If an account of the research is published, or information circulated, a copy of the account or information shall be provided to DEW, within 28 days of its publication or circulation.
13. When planning and conducting your research, please be aware that your work may intrude on locations or involve species with cultural significance to local Aboriginal communities. As part of your project planning it would be a courtesy, and in some cases a requirement, to consult with local Aboriginal representatives to determine any potential impacts and the means of avoiding or limiting them.

Equipment

14. DJI Mavic 2 Pro drone
15. Upon completion of the research, all equipment shall be removed from the marine park sanctuary zone, unless specific approval to the contrary has been obtained.

Vessels

16. The following vessels / vehicles are authorised to be used in association with the activities authorised by this permit.
 - RV Tehthys,
 - RV Polycraft
17. Details of any vessels and aircraft that may be used as part of the activity within marine parks must be provided to the Delegate prior to the commencement of the activity in which they are to be used. Nominated vessels may be used subject to approval of the Delegate

Liability

18. The Permit Holder undertakes the activity authorised in this permit at his/her own risk and releases DEW and other relevant parties from all claims and demands resulting from:
 - any accident, damage, death or injury occurring as a result of activities authorised by this permit; or
 - the pollution, contamination or damage to the marine environment in which the authorised activity is undertaken, and
 - any loss, cost, damage, liability or other detriment incurred in connection with these circumstances.

Persons who will undertake activities authorised by this permit

- Basma Abdul Muhsin - master's student (basma.abdulmuhsin@flinders.edu.au, 0466256766)
- Assoc. Professor David Bruce - main supervisor (david.bruce@flinders.edu.au, 8201 2321)
- Dr. Ryan Barring - associate supervisor (ryan.baring@flinders.edu.au, 8201 5747)
- Other student volunteers and other experienced researchers (if needed)



Jason Irving
Manager, National Parks and Protected Area Program
National Parks and Wildlife Service
Department for Environment and Water

As Delegate under section 23 of the *Marine Parks Act 2007*

Date: 2 May 2021

8.1.2 RPA Operator Accreditation Certificate



Australian Government
Civil Aviation Safety Authority

RPA operator accreditation

Holder: **BASMA ABDUL MUHSIN**

ARN: 1122562

DOB: 20/05/1983

Issued: 16/03/2021

Valid to: 16/03/2024

This accreditation authorises the holder to operate excluded RPA, micro RPA and model aircraft.

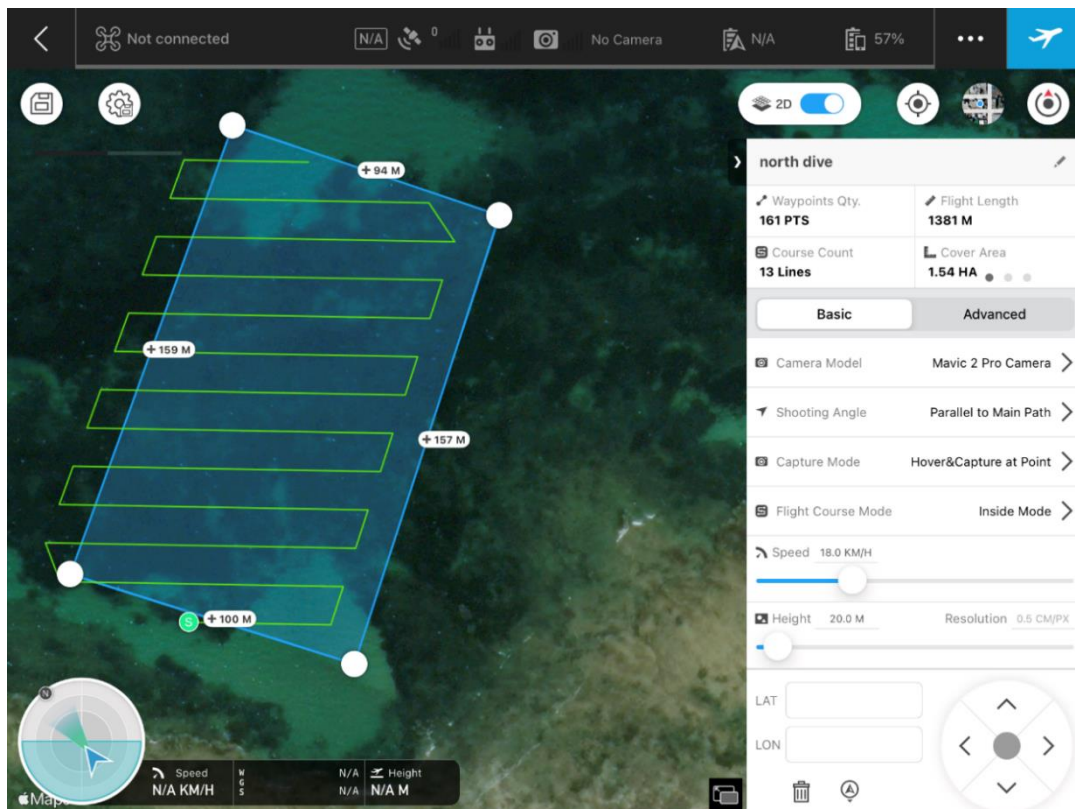
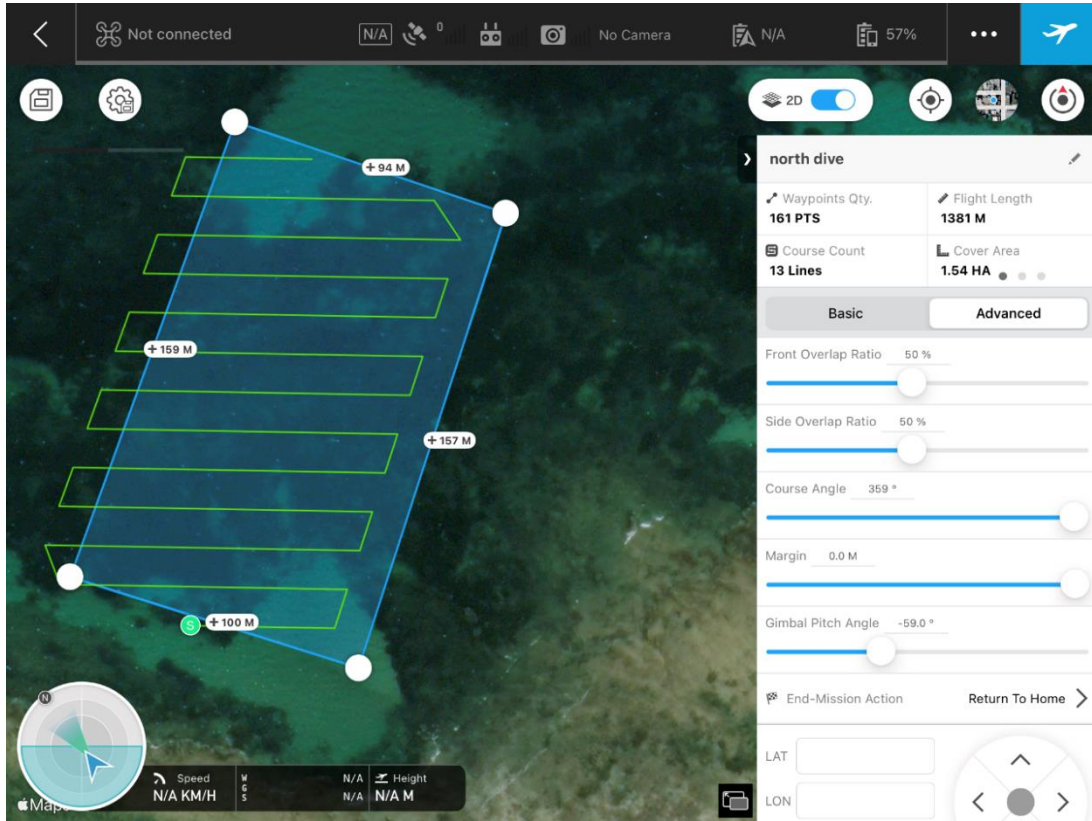
Issued in accordance with regulation 101.374E of the *Civil Aviation Safety Regulations 1998*.

Branch Manager
Client Services Centre
Delegate of the Civil Aviation Safety Authority

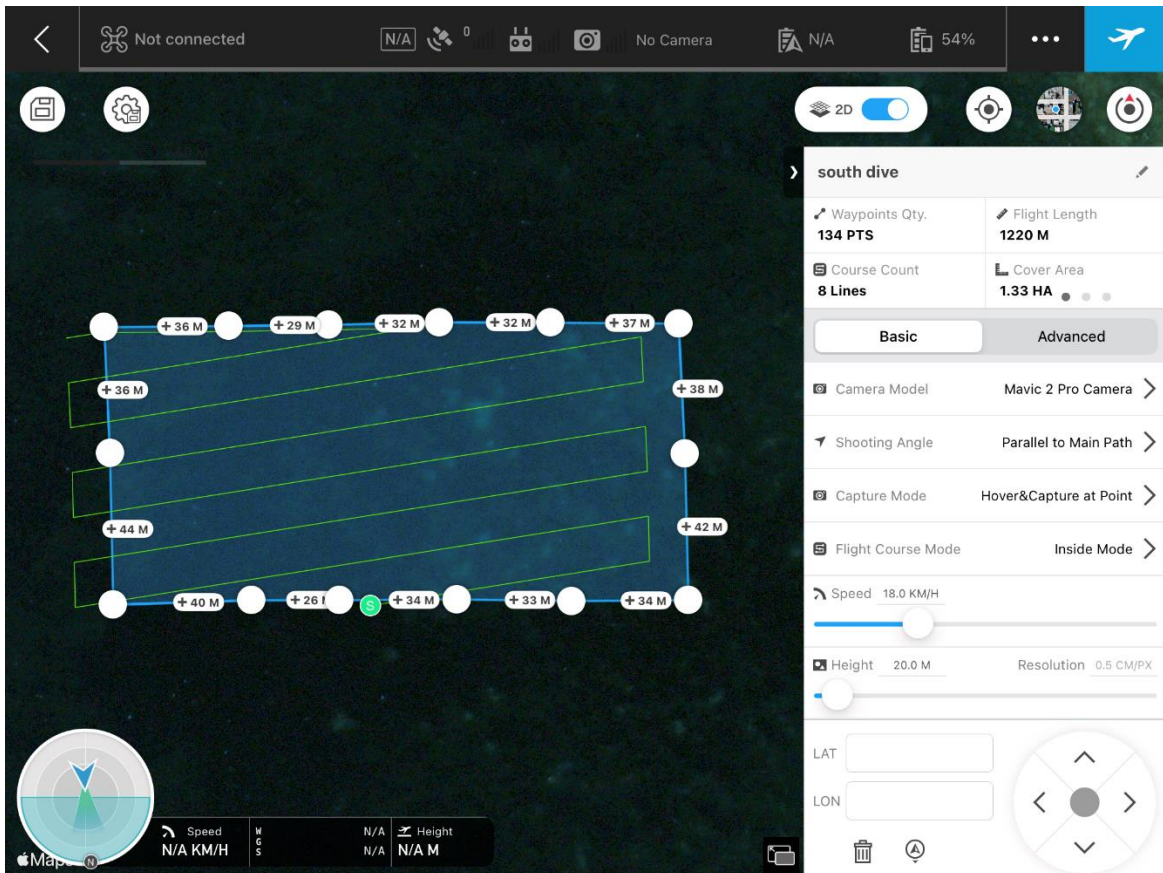
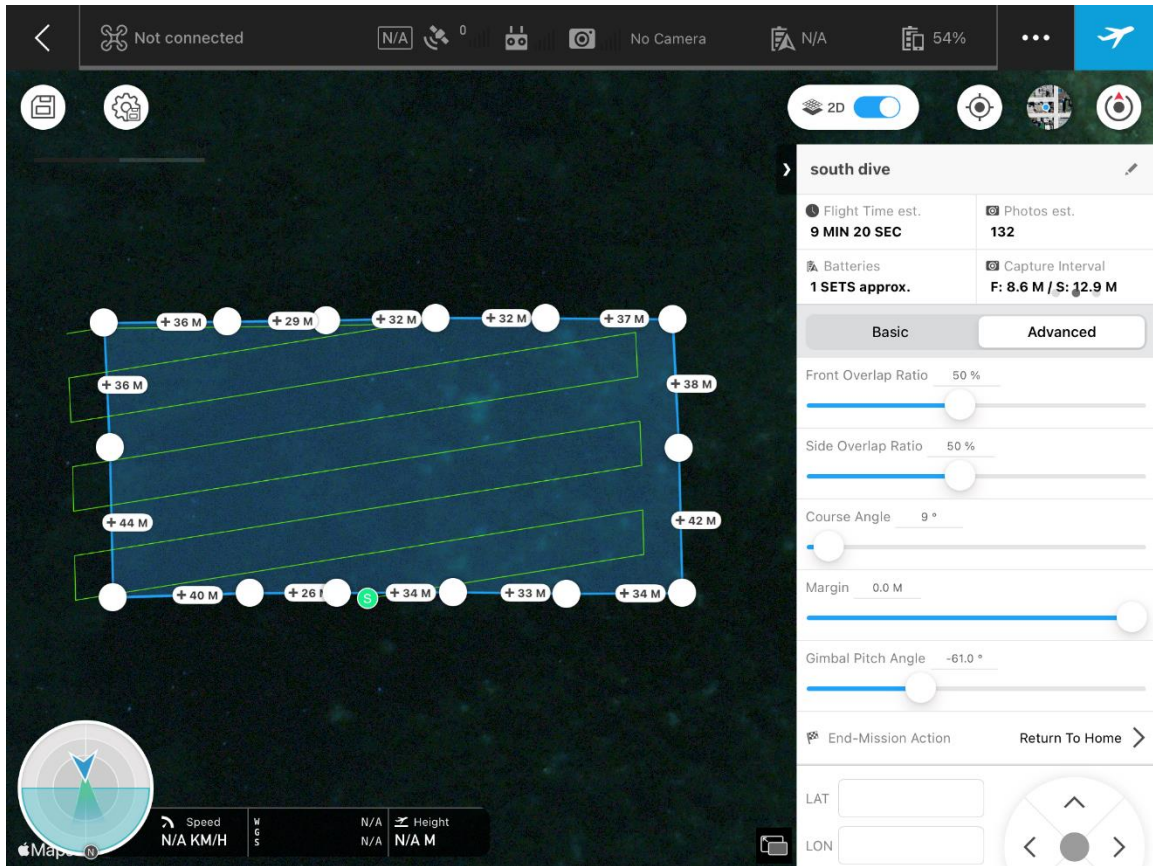
8.2 Screenshots of GSP Missions

8.2.1 Screenshots of GSP 3D Mission Flight Plans to capture overlapping images over the Dive Validation Areas in Zone

North Validation Area



South Validation Area



West Validation Area

Not connected | N/A | 0 | No Camera | N/A | 54%

2D

west dive1

Flight Time est. 11 MIN 20 SEC	Photos est. 163
Batteries 1 SETS approx.	Capture Interval F: 8.6 M / S: 12.9 M

Basic | **Advanced**

Front Overlap Ratio 50 %

Side Overlap Ratio 50 %

Course Angle 9 °

Margin 0.0 M

Gimbal Pitch Angle -60.0 °

End-Mission Action **Return To Home**

LAT

LON

Speed N/A KM/H | Height N/A M

Not connected | N/A | 0 | No Camera | N/A | 54%

2D

west dive1

Waypoints Qty. 165 PTS	Flight Length 1460 M
Course Count 14 Lines	Cover Area 1.55 HA

Basic | **Advanced**

Camera Model **Mavic 2 Pro Camera**

Shooting Angle **Parallel to Main Path**

Capture Mode **Hover&Capture at Point**

Flight Course Mode **Inside Mode**

Speed **18.0 KM/H**

Height **20.0 M** | Resolution **0.5 CM/PX**

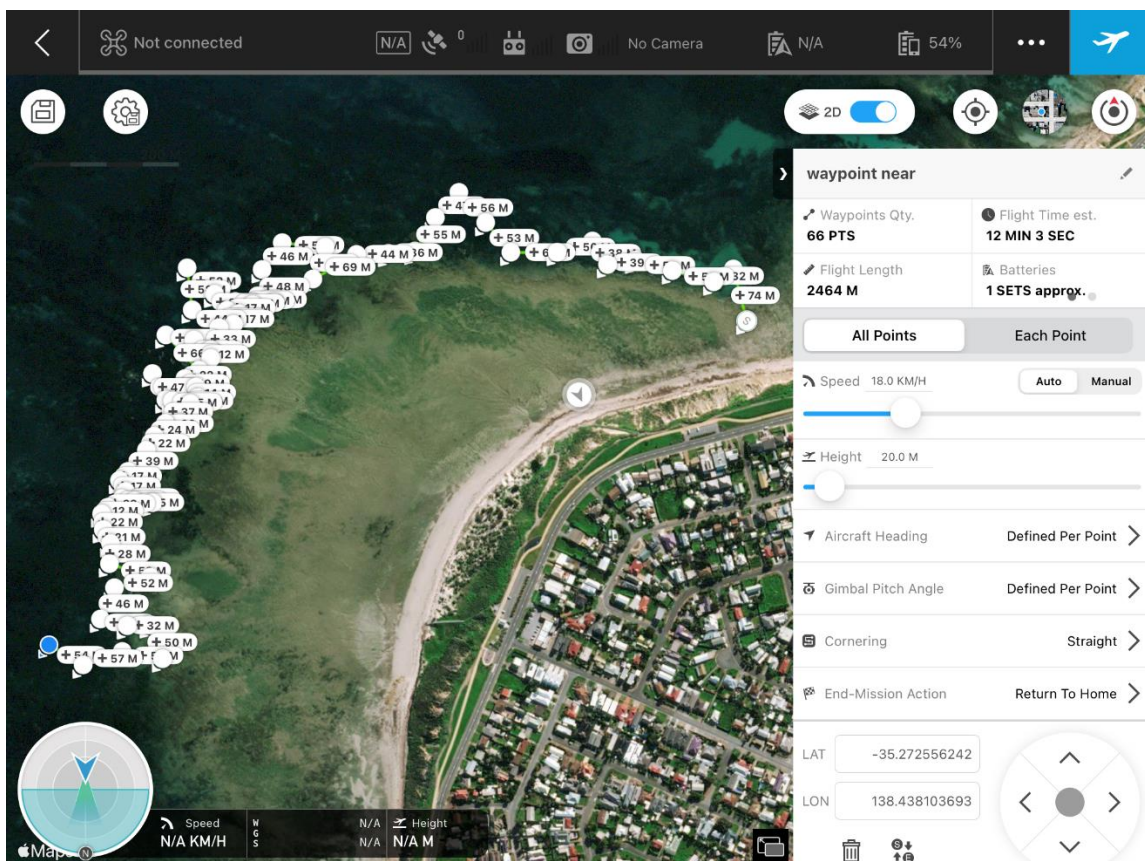
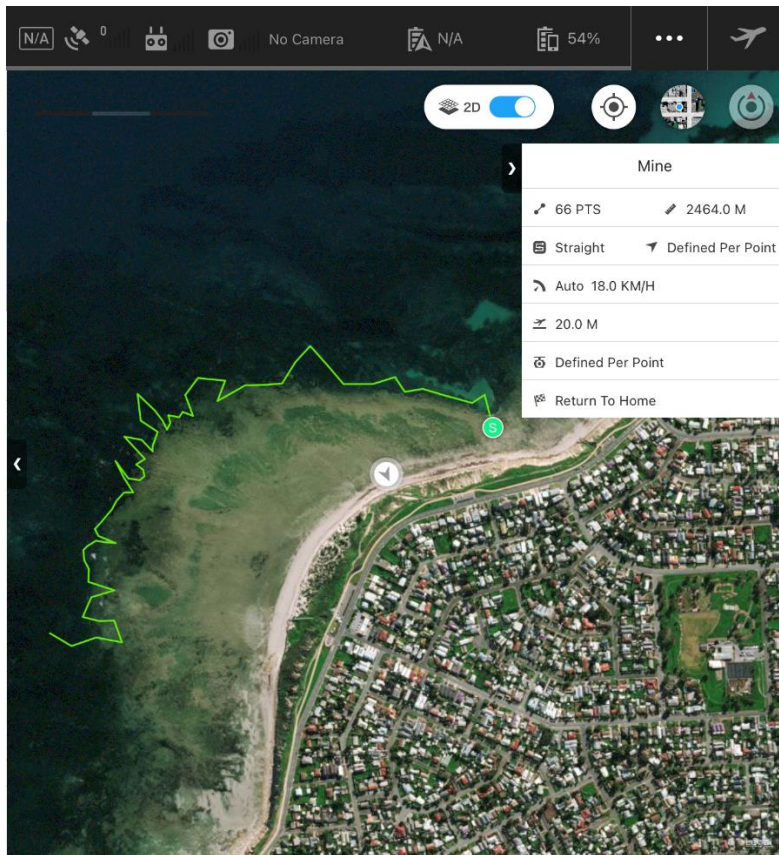
LAT

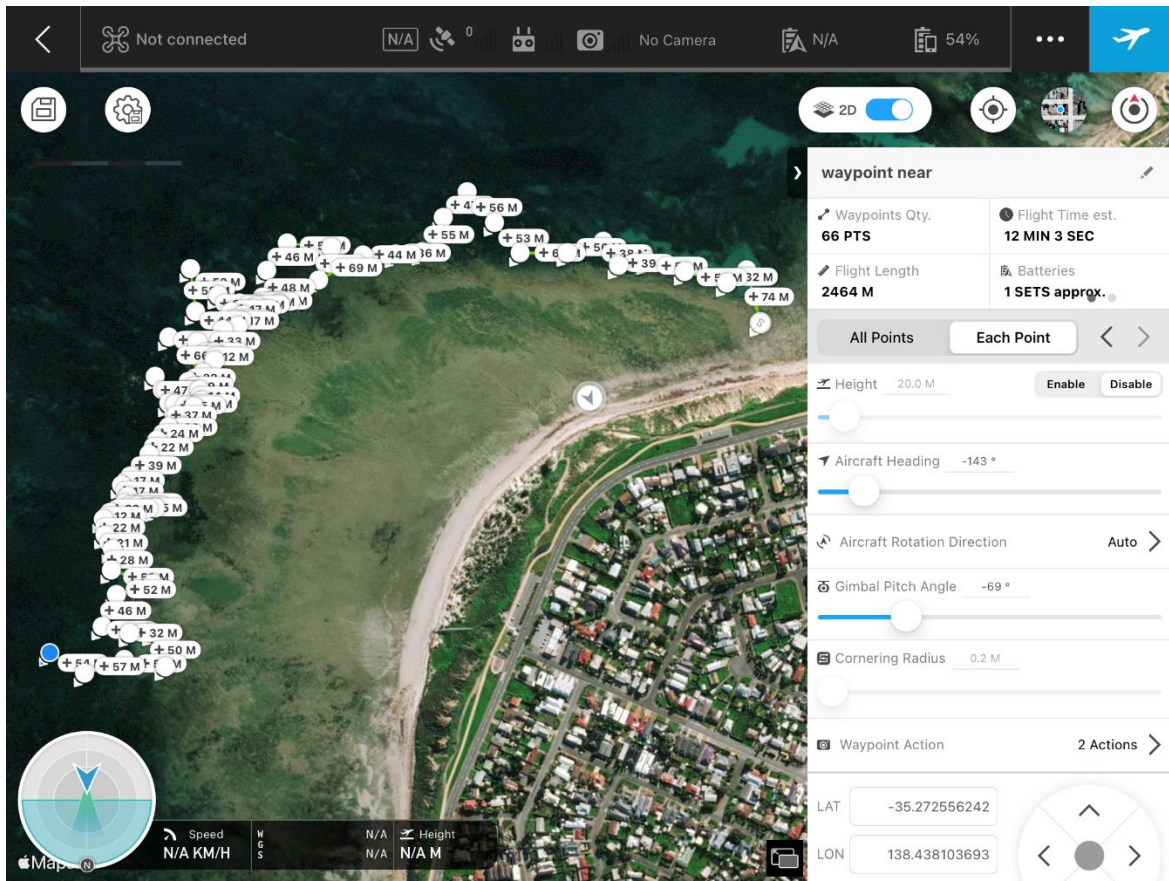
LON

Speed N/A KM/H | Height N/A M

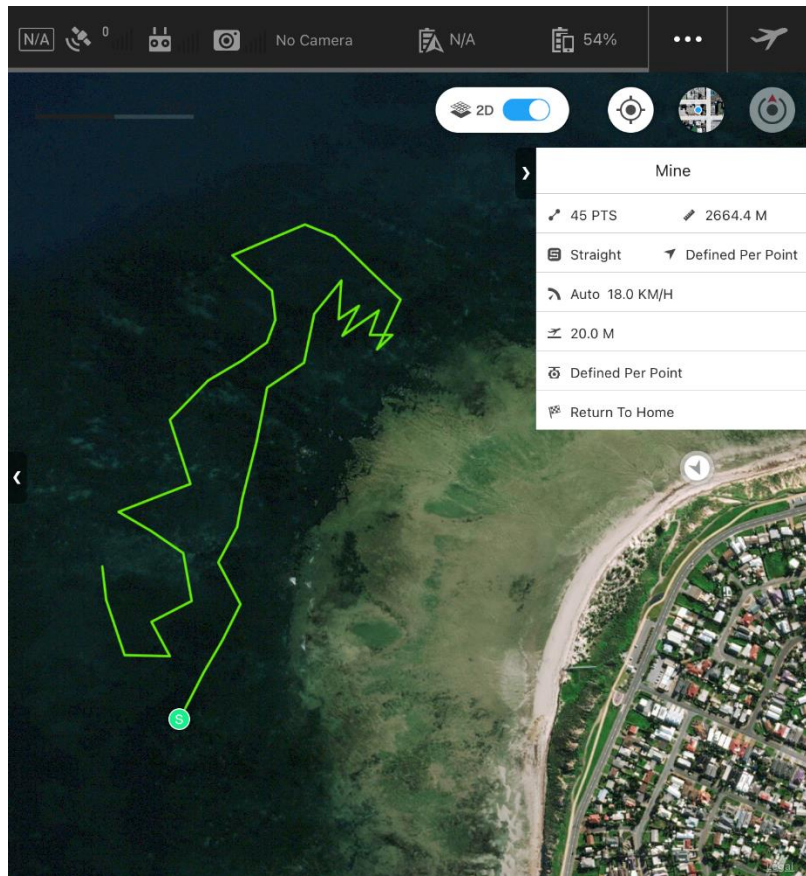
8.2.2 Screenshots of Way Point Mission Flight Plans to capture individual images over Zone I and Zone S

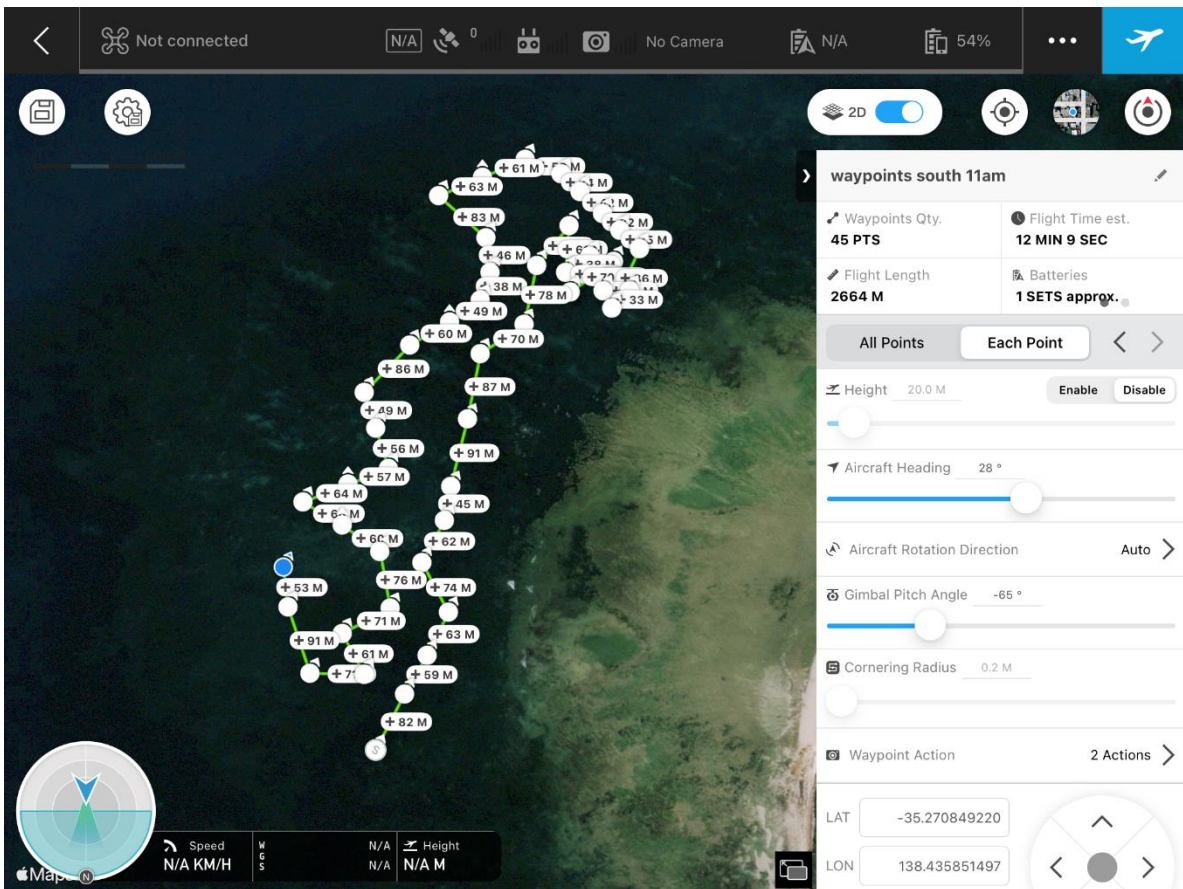
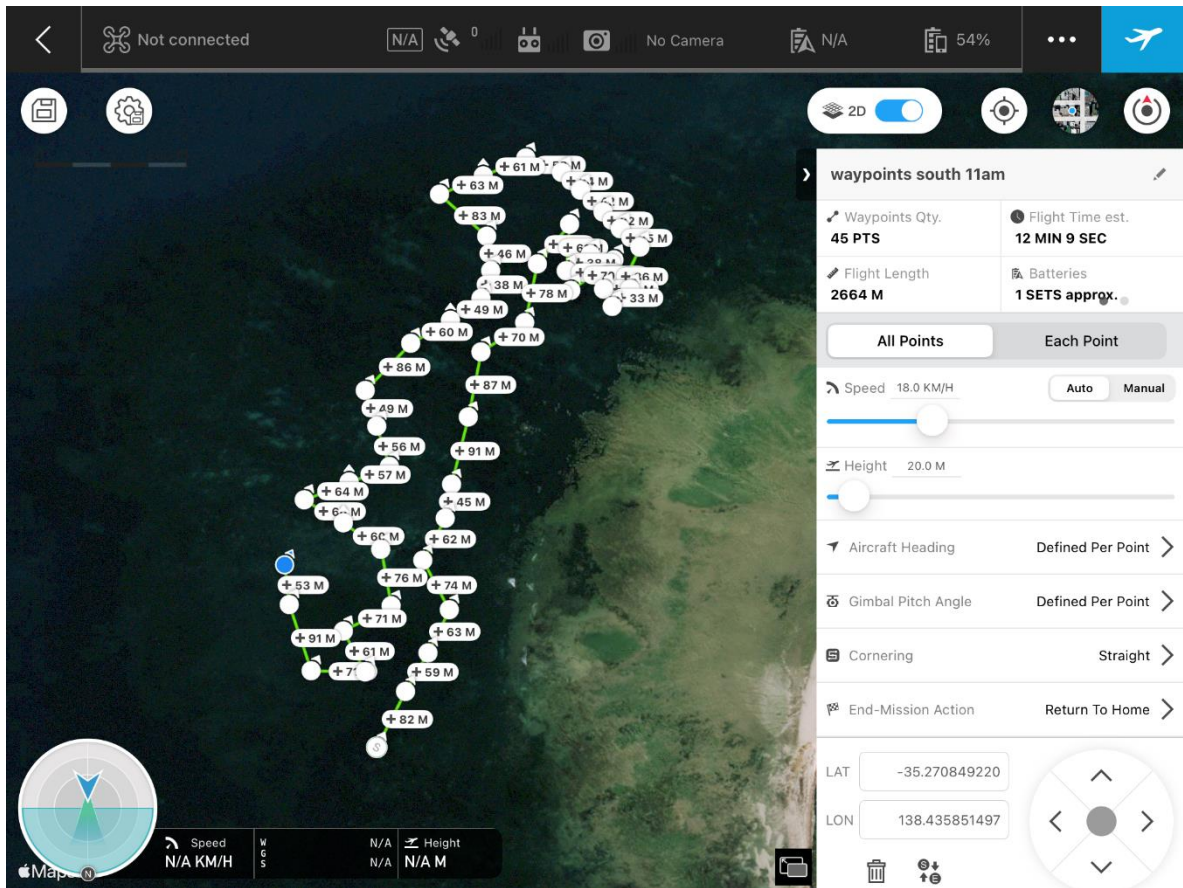
Zone I (carried out in one mission)



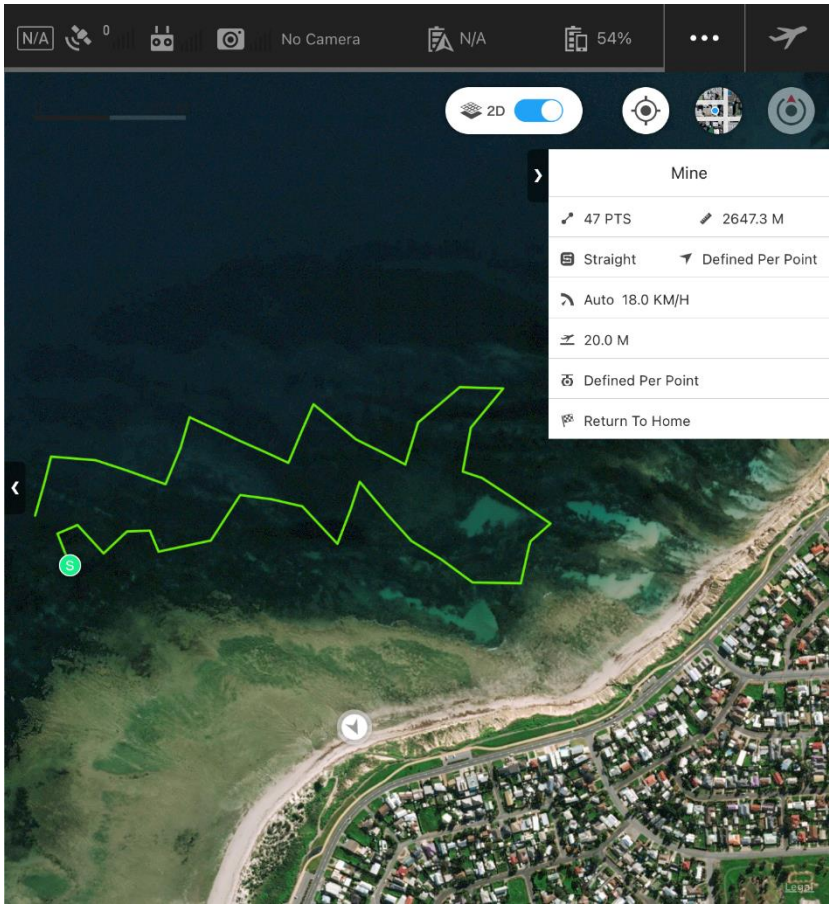


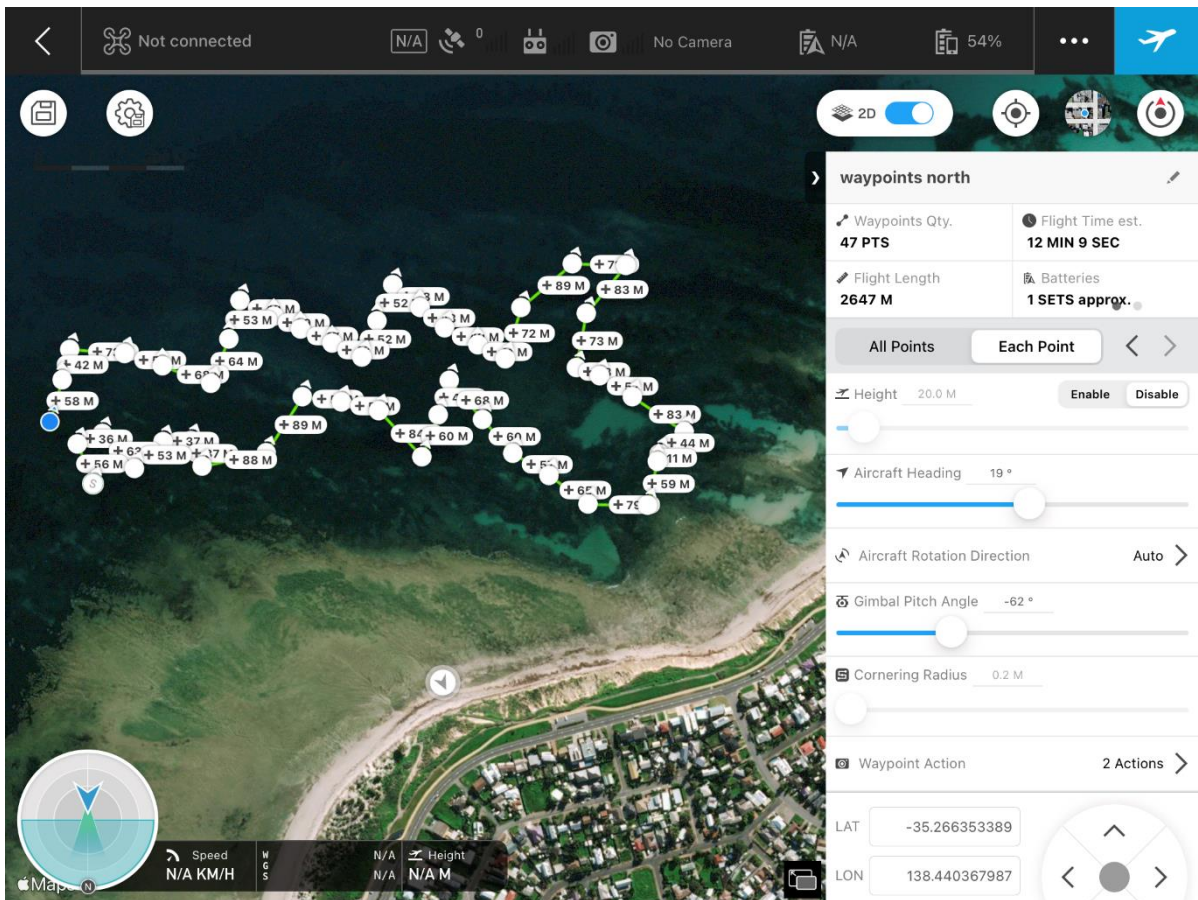
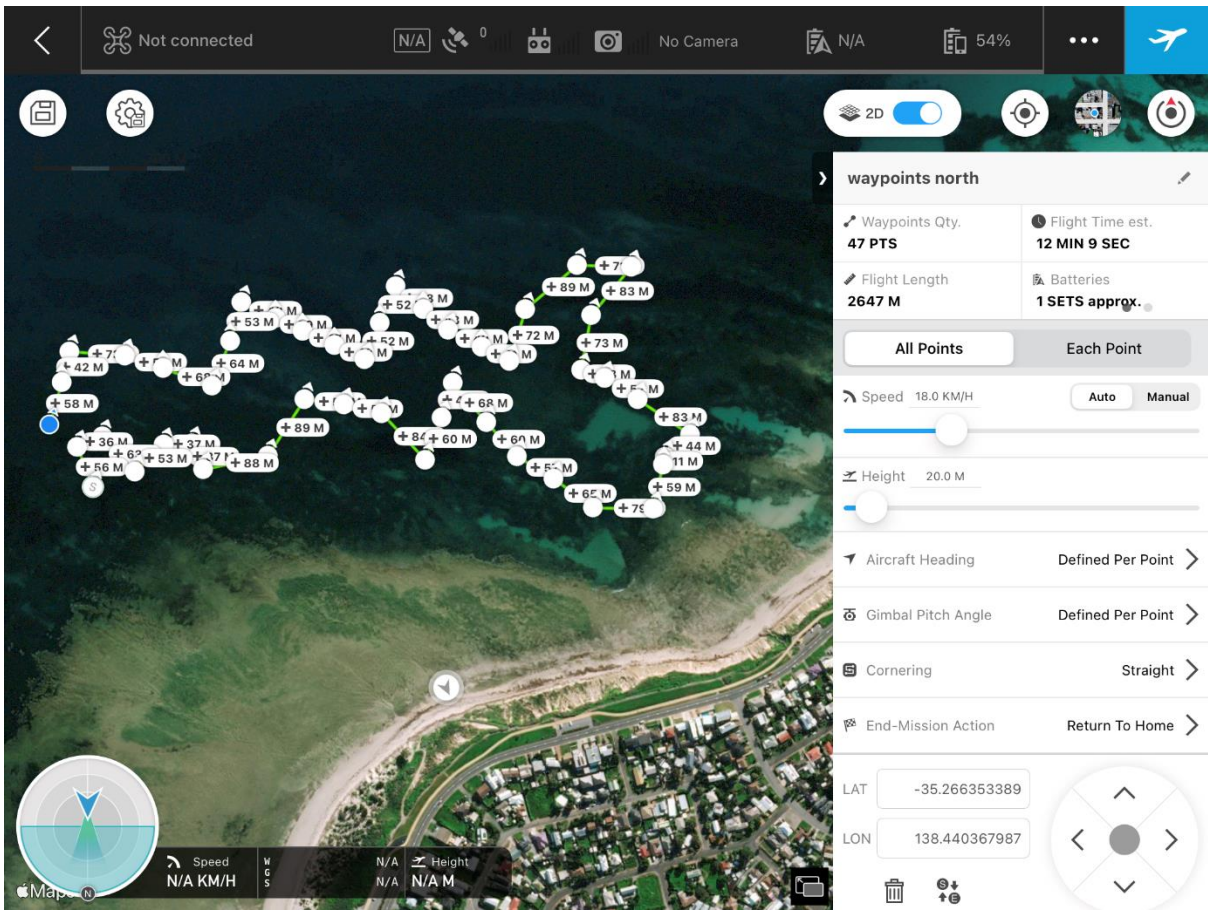
Zone S (Mission 1: Southern Section)





Zone S (Mission 2: Northern Section)

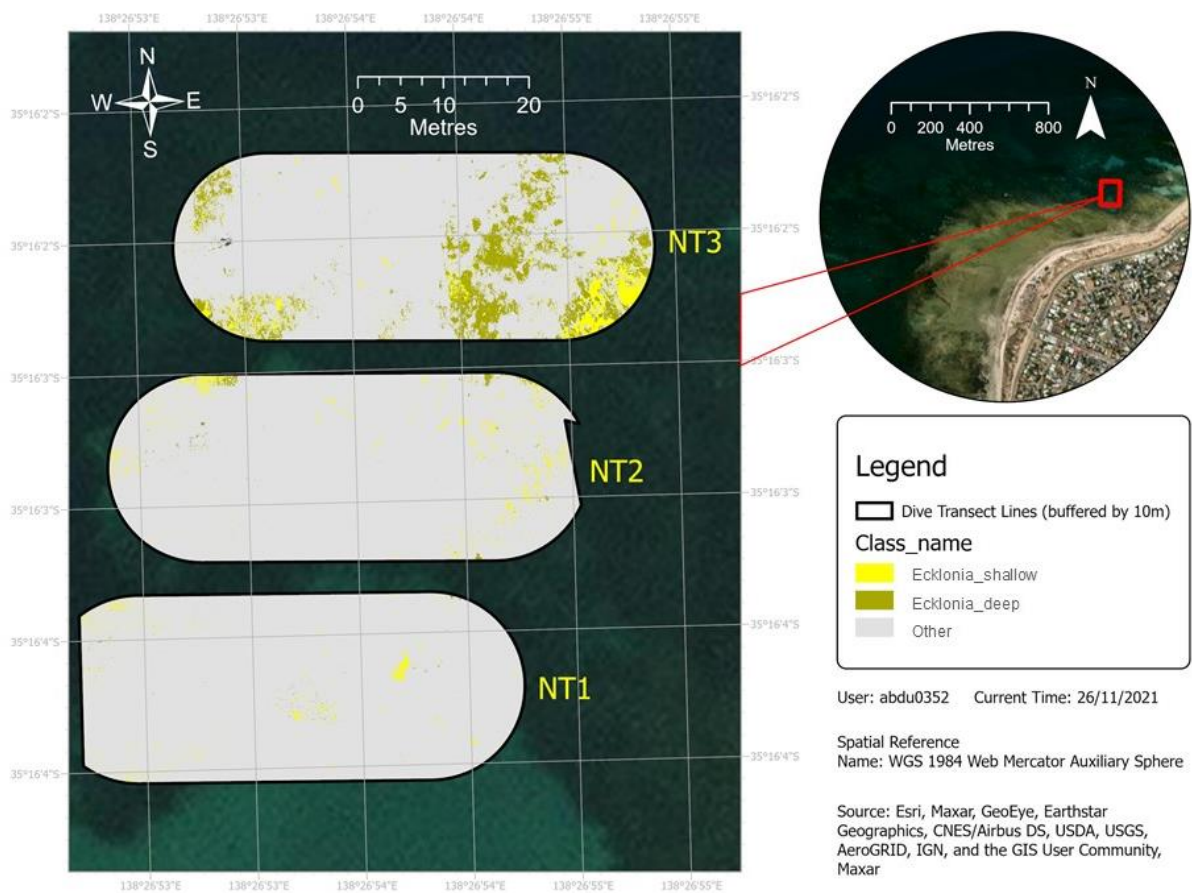




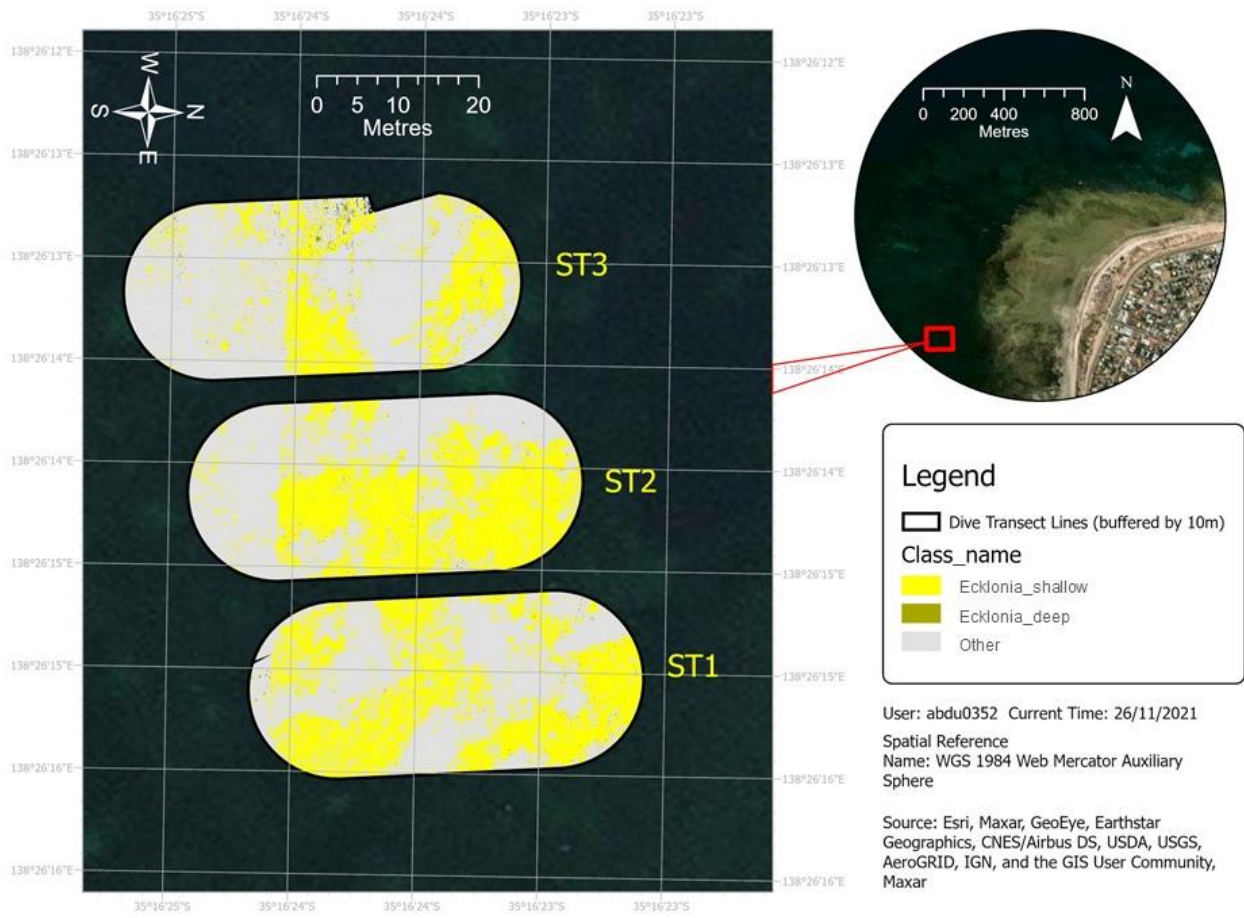
8.3 Map Outputs

8.3.1 *Ecklonia radiata* cover in Validation Sites (Zone S) in Aldinga Reef

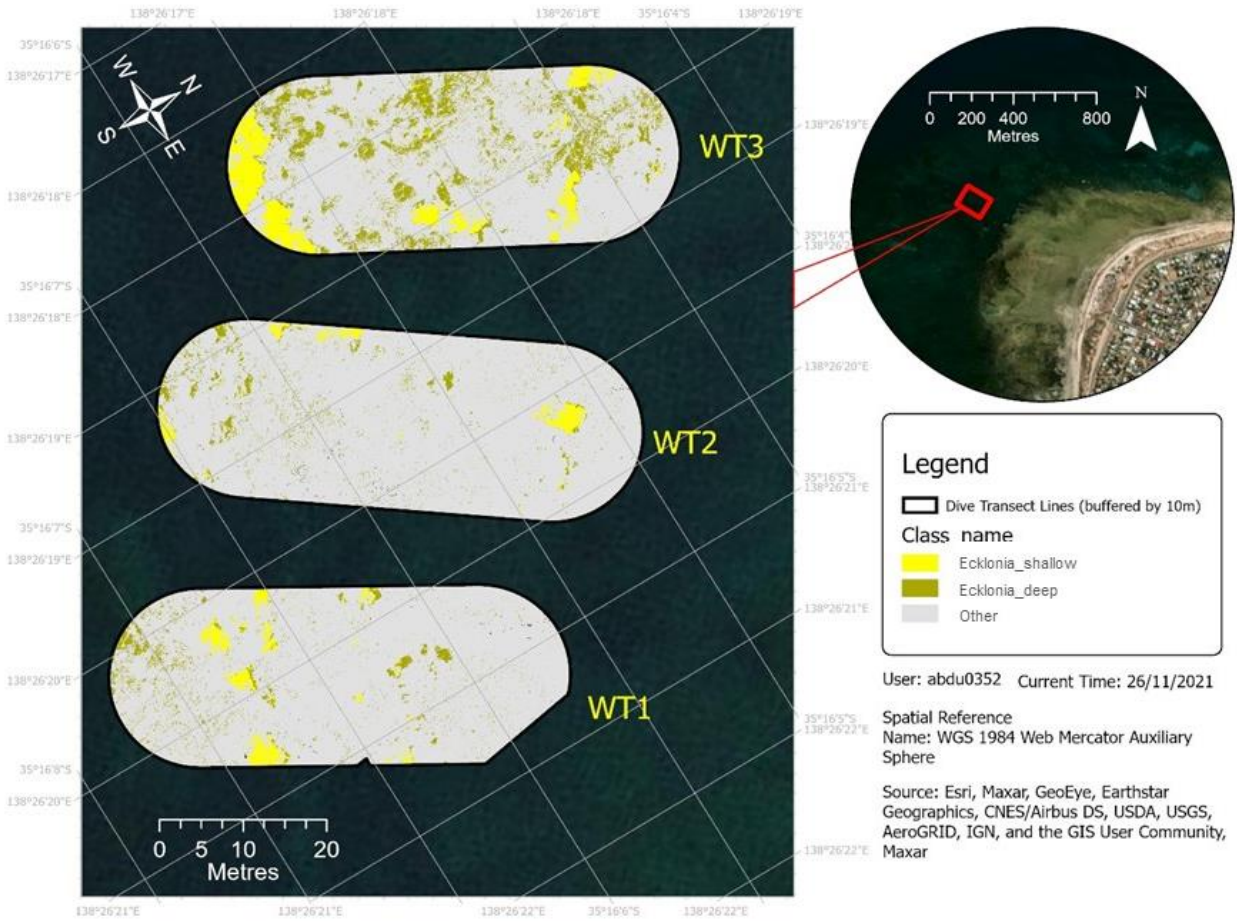
Map 1: *Ecklonia radiata* classification in the North Validation Transects (Zone S) of Aldinga Reef



Map 2: *Ecklonia radiata* classification in the South Validation Transects (Zone S) of Aldinga Reef

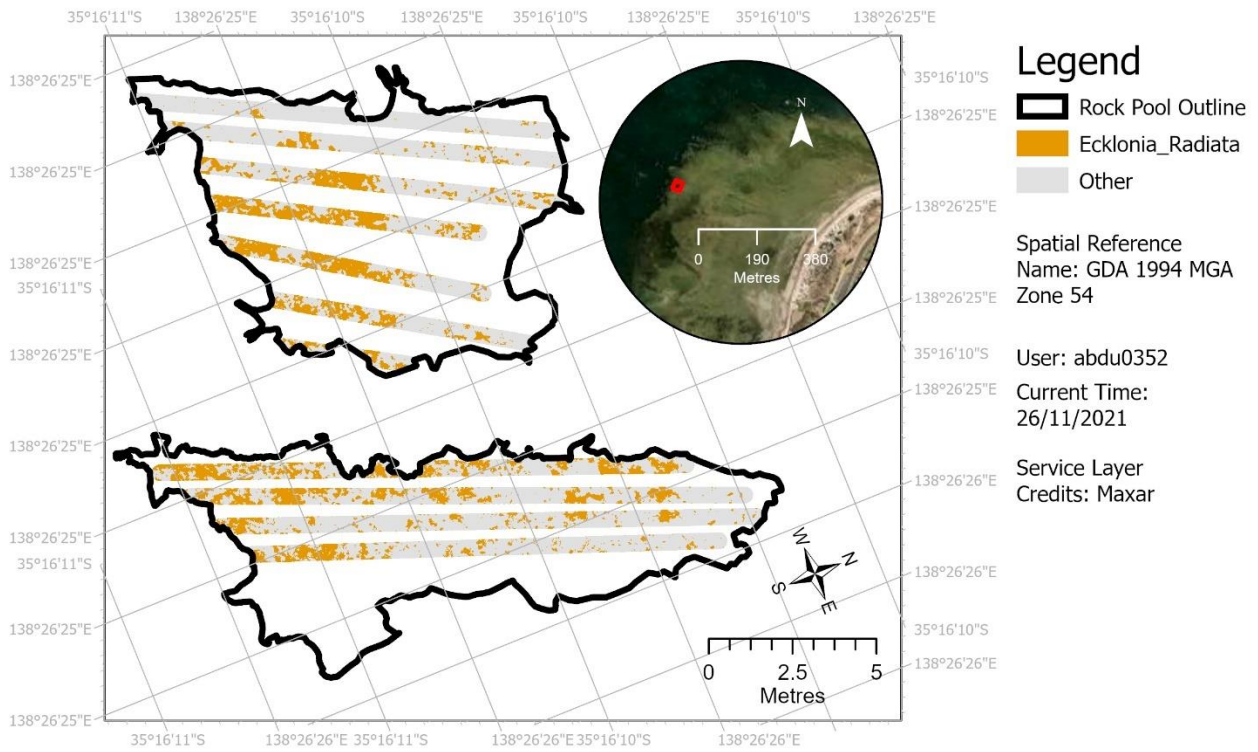


Map 3: *Ecklonia radiata* classification in the West Validation Transects (Zone S) of Aldinga Reef

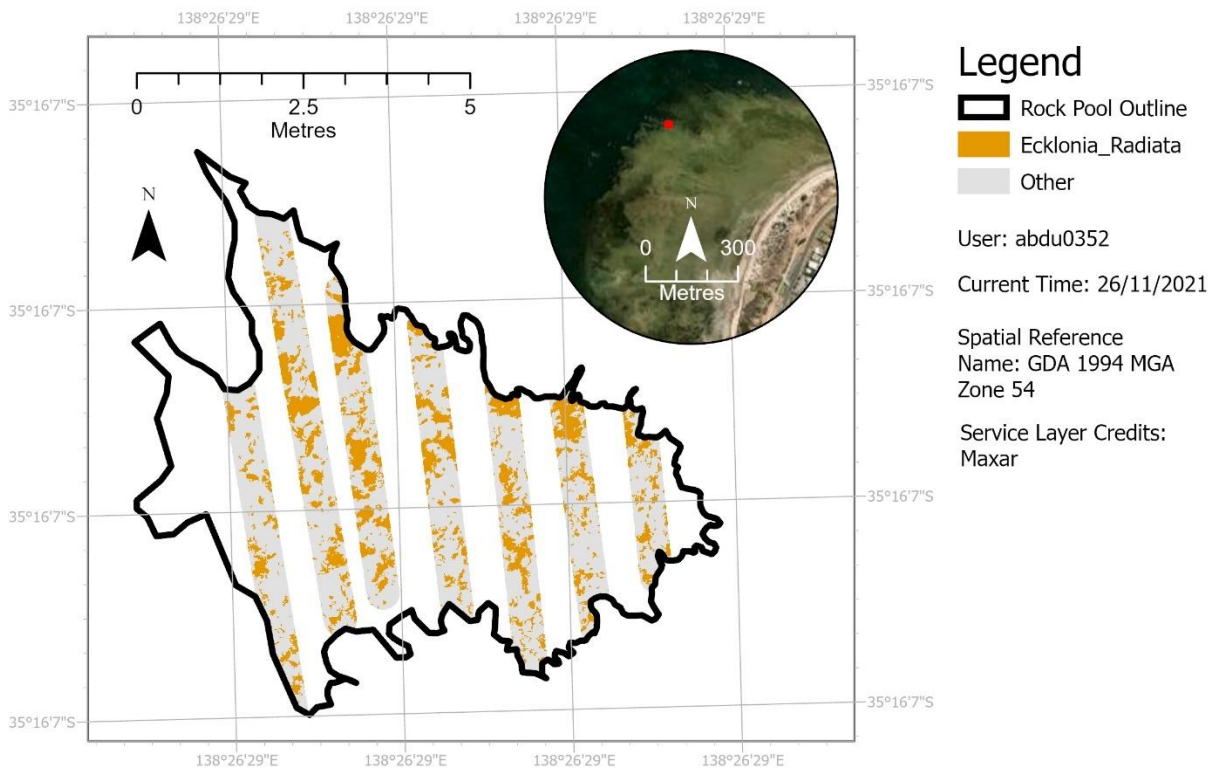


8.3.2 Ecklonia radiata cover in Validation Sites (Zone I) in Aldinga Reef

Map 4: *Ecklonia radiata* classification in the transects over West Deep (WD) and West Shallow (WS) Rockpools (Zone I) of Aldinga Reef

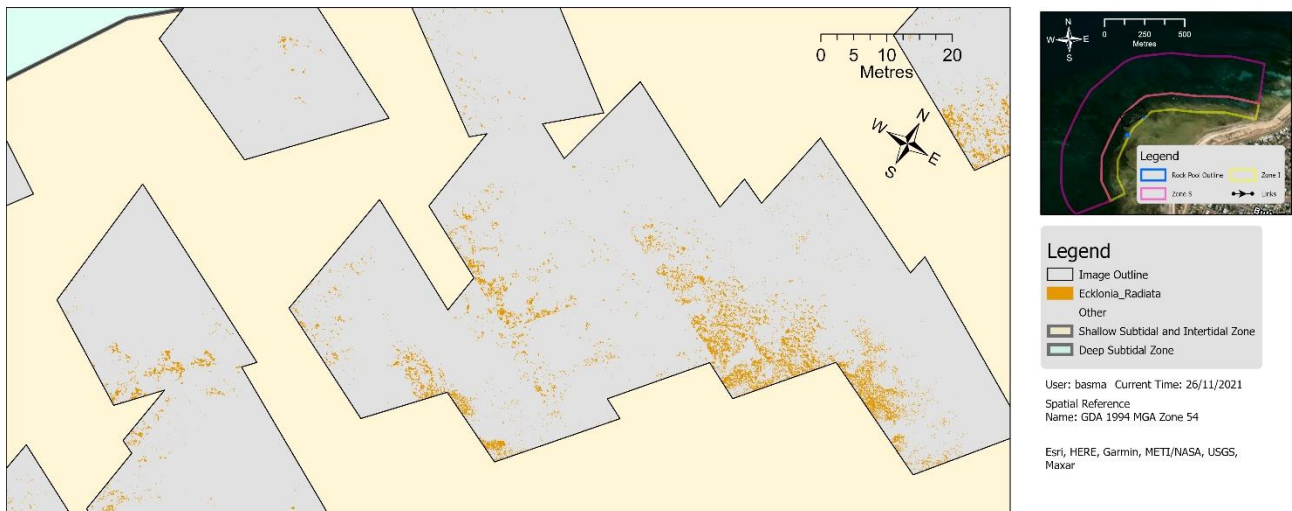


Map 5: *Ecklonia radiata* classification in the transects over North Shallow (NS) Rockpool (Zone I) of Aldinga Reef



8.3.3 Ecklonia radiata cover in Individual Images in (Zone I) in Aldinga Reef

Map 6: A sample area showing *Ecklonia radiata* cover in Individual Images in (Zone I) in Aldinga Reef



8.3.4 Ecklonia radiata cover in Individual Images in (Zone S) in Aldinga Reef

Map 5: A sample area showing *Ecklonia radiata* cover in Individual Images in (Zone S) in Aldinga Reef

